Development of Neural-Network-Based Digital Pulse Processing for Photoneutron Detection

by

Abbas Johar Jinia

A dissertation submitted in partial fulfillment
of the requirements for the degree of
Doctor of Philosophy
(Nuclear Engineering and Radiological Sciences)
in the University of Michigan
2023

Doctoral Committee:

Professor Sara A. Pozzi, Co-Chair
Dr. Shaun D. Clarke, Co-Chair
Professor Igor Jovanovic
Associate Professor Hun-Seok Kim
Professor David D. Wentzloff

Abbas Johar Jinia

ajinia@umich.edu

ORCID iD: 0000-0002-6619-2207

Dedication

Dedicated to my beautiful family.

Acknowledgements

It would not have been possible to write this Ph.D. dissertation without the help and support of the kinds of people around me, to only some of whom it is possible to give mention here. Above all, I would like to thank Dr. Mohammed Burhanuddin and my family, who have given me love and support throughout, as always, for which my mere expression of thanks will not be sufficient.

This Ph.D. dissertation would not have been possible without the constant encouragement and guidance of my two advisors, Prof. Sara Pozzi and Dr. Shaun Clarke. Their knowledge of radiation detection, nuclear non-proliferation and safeguard, and Monte Carlo simulations has been invaluable, for which I am extremely grateful. A special thanks to Prof. David Wentzloff and Prof. Hun-Seok Kim. Their knowledge of machine learning algorithms and its implementation for real-time data analysis has been very crucial for this Ph.D. work. I express my gratitude to Prof. Igor Jovanovic whose knowledge of active interrogation has been instrumental.

The current work has been supported by the U.S. Department of Homeland Security (DHS), Countering Weapons of Mass Destruction Office (CWMD), Academic Research Initiative under Grant No. 2016-DN-077-ARI106. This work was also funded in-part by the Consortium for Monitoring, Technology, and Verification under Department of Energy (DOE), National Nuclear Security Administration (NNSA) award number DE-NA0003920. I express my gratitude to the DHS-CWMD and the DOE-NNSA for their gracious support.

The members of my team, Christopher Meert and Tessa Maurer, have been great resources and means of help for this work. The measurement results presented in the current work would not have been possible without the support and feedback from my team members. My gratitude to all members of the team. Additionally, I am grateful to the past and current graduate students in the Detection for Nuclear Non-Proliferation Group (DNNG) who have provided honest feedback on my research work and have been great friends.

I would like to acknowledge the Department of Nuclear Engineering and Radiological Sciences at the University of Michigan for providing the necessary support. The library facilities and computer facilities of the university have been very important. Last but no means least, I thank all my friends around the world for their support and encouragement throughout.

Table of Contents

List of Tables

List of Figures

Abstract

High-energy photon interrogation is a non-destructive technique that is used to detect hidden special nuclear materials (SNMs) and characterize nuclear waste. The development of such systems is complex and requires Monte Carlo simulations to optimize system performance. Monte Carlo simulations rely on various scattering, absorption, and photonuclear cross-section data. The scattering and absorption cross-section data for neutrons and photons has been extensively studied and validated with experiments because of their importance in nuclear reactor and radiation shielding simulations. However, photonuclear cross-sections are not extensively studied and lack the desired validation with measured results. The under-prediction by Monte Carlo codes can range from 20-30%, and therefore there is a need to validate photonuclear cross-section data with precise new measurements.

The present Ph.D. research provides new measured results for photoneutron count rates from various high-Z targets. The measured results were compared with the simulated results obtained by Monte Carlo codes. The simulations were performed using the MCNPX-PoliMi transport code with the most updated photonuclear cross-section data. For measurements of photoneutrons, several high-Z targets were interrogated with bremsstrahlung photons from a 9-MV electron linac, and fast neutrons were detected with four *trans*-stilbene organic scintillators. The comparative study between measurement and simulation provided a quantitative assessment of the under-prediction in the photoneutron count rates by MCNPX-PoliMi.

During interrogation of targets, the intense bremsstrahlung photons from the linac creates significant pulse pile-up in *trans*-stilbene. The pulse pile-up effect was mitigated by developing an artificial neural network (ANN) system for digital processing of scintillation pulses. The developed ANN system outperformed traditional pulse shape discrimination methods during an active ^{252}Cf measurement. In this measurement, prompt fission neutrons were measured from a ^{252}Cf spontaneous fission source in the presence of the intense photon flux from the linac, imitating a challenging radiation environment for the measurement of fast neutrons.

Photoneutrons were measured from a SNM surrogate, such as depleted uranium (DU), and a non-SNM target, such as lead. The results obtained from the developed ANN system showed a 5x increase in the photoneutron count rate when lead target was replaced with the DU target. Additionally, the light output distribution for lead photoneutrons was softer than the light output distribution for DU photoneutrons. This difference in the light output distributions is a new result because there exists no prior work in the literature that detected photoneutrons without time-of-flight and coincidence counting. The DU target was further interrogated in various iron and polyethylene shielded configurations. The measured photoneutron count rates decreased with an increase in shield wall thickness. This decreasing trend is due to the moderation of photoneutrons by polyethylene, and the attenuation of bremsstrahlung radiation by iron.

The interrogation measurements of DU in bare and shielded configurations were simulated using the developed MCNPX-PoliMi framework. For a light output window of 0.28 – 2.67 MeVee (1.66 – 6.85 MeV proton recoil energy), the simulated photoneutron count rate under-predicted the measured rate by 32.8 $\pm$ 3.2%. The findings from this work provide new measured results that can help improve photonuclear cross-section data for uranium, which in turn will enhance simulation capabilities with existing Monte Carlo codes.

Chapter 1 Introduction and Motivation

Active interrogation using high-energy photons is a non-destructive assay technique that is used to detect special nuclear materials [1–3] and characterize nuclear waste [4,5]. The development of high-energy photon interrogation systems is complex and requires Monte Carlo simulations to optimize system performance for a given application. Monte Carlo simulations rely on various scattering, absorption, and photonuclear cross-section data. The scattering and absorption cross-section data for neutrons and photons has been extensively studied and validated with experiments because of their importance in nuclear reactor and radiation shielding simulations. However, photonuclear cross-sections are not extensively studied and lack the desired validation with measured results [6]. The results obtained from photonuclear simulations are found to under-predict measured results, indicating uncertainties in the cross-sections themselves. The discrepancy between measurement and simulation can be as high as 20-30% [7], and therefore, there is a need for new supporting measured results that can be used to quantify under-prediction in these cross-sections.

Most recently, Sari performed characterizations of photoneutron fluxes emitted by a linear accelerator (linac) in the 4-20 MeV energy range using the MCNPX transport code [8]. The author identified that the lack of knowledge of photoneutron yield both near the reaction energy threshold and at the maximum of the cross-section curve could potentially be the cause of unreliable photoneutron fluxes. In a research project coordinated by the International Atomic Energy Agency,

Varlamov performed a reliability study of photonuclear cross-section data obtained by Lawrence Livermore National Laboratory in the U.S. and Saclay Laboratory in France [9]. The author identified disagreements between data from two laboratories for partial reaction cross-sections. This disagreement results from the different photoneutron multiplicity sorting methods used by the two laboratories. Noticeable uncertainties were reported in the evaluated photonuclear cross-section data, and therefore, precise measurements of photoneutron yield are needed to validate photonuclear cross-section data.

The measurement of the photoneutron yield from a target is challenging due to the presence of the intense photon flux, which causes challenges such as pulse pile-up (i.e., two or more pulses occurring within the detection time window), detector saturation, and a poor signal-to-background ratio. The interaction of high-energy photons, through photonuclear reactions e.g. (γ, Xn) with the surrounding high-Z materials creates an elevated neutron background. This "active" background reduces the signal-to-background ratio. The pulse pile-up further complicates the measurement because if piled-up signals are not eliminated they can cause misclassification of the data, and upon elimination of piled-up events there is loss of information. Thus, it is crucial to mitigate these challenges during active interrogation.

In this Ph.D. work, I significantly enhanced digital pulse processing by developing and demonstrating an artificial neural network system that can recover neutron and photon pulses from piled-up events. Experiments were performed to measure the photoneutron count rate from various targets using *trans*-stilbene organic scintillators and a 9-MV electron linac. Additionally, a comparative study was made between the measured and simulated results obtained with the MCNPX-PoliMi transport code. The detailed comparison performed in this work provided a

quantitative assessment on the under-predictions in the photoneutron count rates obtained by Monte Carlo codes.

1.1 Existing Literature

1.1.1 Artificial Intelligence in Nuclear Safeguards and Non-proliferation

Artificial intelligence is a technique that enables computers to mimic human behavior. Deep learning is a subset of artificial intelligence that extracts patterns from data using artificial neural networks (ANNs). With recent technological advances in computing resources, ANN hardware accelerators and deep architectures, ANN technology has gained maturity to learn complicated functions that can represent high-level abstractions [10]. The use of ANN technology is reaching astonishing heights in several areas of science and technology, and the nuclear community is working collaboratively to identify requirements, needs, and opportunities for artificial intelligence in nuclear safeguards and non-proliferation.

Radiation imaging plays a vital role in monitoring, localizing, and characterizing radioactive sources for nuclear security and safety. Olesen and colleagues developed a convolutional neural network (CNN) encoder-decoder architecture to reconstruct images from the rotating scatter mask imaging system [11]. The authors demonstrated that the CNN-based reconstruction algorithm outperforms the standard maximum-likelihood expectation–maximization (ML-EM) algorithm. The relative error of reconstruction was reduced from 145% to 33% and precision was increased from 27% to 85%. Additionally, the CNN-based algorithm demonstrated a successful reconstruction of the image with minor degradation when the network was trained on noisy input data. Similarly, in another study by Zhang et al., the CNN-based reconstruction was found to improve the quality of reconstructed images for coded-aperture imaging systems under low count conditions [12].

NEutron Detector Array (NEDA) is a state-of-the-art detection system built for safeguards applications [13]. NEDA is a versatile device with 331 EJ-301 liquid scintillators that has high detection efficiency, excellent particle discrimination, and high-count rate capabilities. Fabian et al. developed three different ANN architectures, multi-layer perceptron (MLP), CNN, and long short-term memory (LSTM) for neutron and gamma-ray discrimination in the neutron detector of NEDA [14]. The authors concluded that all three ANN architectures performed quite similarly, and LSTM was found to be robust against time misalignment of the scintillator voltage pulse. Another comparative study of ANN architectures was performed by Tambouratzis et al [15]. Linear vector quantization (LVQ) and self-organizing maps (SOM) were the two ANN architectures that were investigated. The investigation found SOM to have superior overall accuracy at all energies.

To mitigate the effect of pulse pile-up, Belli et al. provide a method for recovery of piled-up pulses from the NE-213 detector [16]. In this method, the first pulse in a piled-up event is fitted with a response function. The response function is specific to the detector, as it is a function of the scintillators decay constant, and the time constant of the measuring circuit. The second pulse is then recovered after subtracting the first partially fitted pulse from the piled-up event. The subtraction process continues until all single pulses from the piled-up event are recovered. The process proposed by Belli et al. is non-trivial and quite complex to implement in real time.

An ANN approach was demonstrated by Kafaee and Saramad to recognize piled-up events from a NaI scintillator and recover gamma information [17]. The authors used an MLP with the Levenberg–Marquardt backpropagation learning algorithm. The developed ANN consisted of an input layer with a dimension of 8, two hidden layers each had a dimension of 20, and an output layer with a dimension of 3. The measured gamma energy spectrum was found to have a reduced

effect of piled-up events and an increased count in the full-energy photopeak. Additionally, MLP was found to outperform hardware-based pile-up rejection methods.

In 2018, Fu et al. used ANN to recover piled-up pulses [18]. Fully connected neural networks (Fc-NN) and recurrent neural networks (RNN) were developed to perform pulse shape discrimination and identification of piled-ups produced by organic scintillators. The performance of Fc-NN and RNN was tested in a high-radiation environment (100,000 counts per second) that had a gamma-ray to neutron ratio of approximately 400-to-1. The authors demonstrated that ANN has greater accuracy in identifying piled-up events than traditional charge integration methods. Additionally, the capability of ANN in recovering neutron and photon information from piled-up events was demonstrated. The authors found that RNN achieved a better classification of individual pulses in a piled-up event compared to Fc-NN. In a similar study, Han et al. investigated the performance of CNN to classify scintillation pulses from Cs_2LiYCl_6 (CLYC) detector [19]. The authors demonstrated classification of neutron, photon, and piled-up signals with a discrimination error of approximately 4%.

Artificial intelligence has demonstrated its potential in radiation detection; however, there is limited literature available on the applicability of neural networks in intense radiation environments, such as the bremsstrahlung radiation from the linac, which causes significant pulse pile-up. In the present work, I developed and demonstrated an ANN system that can be used in such intense radiation environments for scintillation pulse processing. Supporting experiments and accompanying simulations were performed to validate the performance of the developed ANN system.

1.1.2 Prompt Photoneutron Detection

Numerous systems have been developed that rely on prompt photofission neutrons for the detection of hidden SNMs. In 2007, Blackburn et al. demonstrated the detection of prompt photofission neutrons from depleted uranium. In Blackburn's experiment, high-energy photons were produced with a 10-MV electron linac from Varitron operating at 125 Hz. Interrogation measurements with a) no material present (active background), b) bismuth, and c) depleted uranium were performed and signals that fell under 3 μs of the accelerator pulse were analyzed. An EJ-200 fast plastic scintillator detector was used to monitor photoneutrons. The measured integral counts demonstrated successful identification of actinides among other photoneutron producing targets, such as bismuth.

In 2014, Mueller et al. proposed a novel method to discriminate between fissile and non-fissile contents of SNM [20,21]. The proposed method exploits the difference in the prompt neutron yield parallel and perpendicular to the plane of γ-ray beam polarization. This difference in prompt neutron yield is referred to as polarization asymmetry. High-energy photons with energies between 5.3 and 7.6 MeV were used to interrogate several actinide targets (i.e., ^{232}Th, ^{233,235,238}U, ^{237}Np, and ^{239,240}Pu) and 18 BC-501A liquid scintillators were used for fast neutron detection. The authors found that non-fissile targets had significant polarization asymmetries ranging from 0.2 to 0.5, whereas fissile targets had asymmetries of nearly zero. The method proposed by Mueller and colleagues could be used to simultaneously detect and identify fissile and non-fissile fissionable material during active interrogation. Since the asymmetry is much smaller for fissile actinides, this method could theoretically be used to determine the enrichment of small samples of SNM (approximately 1 g/cm^2) to the level of 10% enrichment. Additionally, the authors found that this asymmetry was relatively insensitive to moderate amounts of lead, steel, and high-density polyethylene shielding. Another study for the applicability of photofission reaction ratios to

identify enrichment was performed by Chin et al. [22,23]. The authors demonstrated that by calculating the ratio of photofission neutrons produced by a higher photon energy over a lower photon energy, quantitative information on uranium enrichment could be obtained.

An X-ray inspection system has been developed by Passport Systems Inc. to scan cargo containers for possible contrabands, anomalies, and nuclear threats [1,24]. This system utilizes a continuous wave 9 MeV rhodotron to induce photofission reactions in SNM. Prompt fission neutrons were detected with phenylxylylethane (PXE) liquid scintillation detectors. During the initial testing, interrogation measurements with a) depleted uranium, b) heavy water, and c) beryllium were performed. Both heavy water and beryllium have defined photoneutron endpoint energies at 3.4 MeV and 6.5 MeV respectively for a 9 MeV interrogating photon; however, depleted uranium does not have an endpoint energy because of the presence of prompt fission neutrons. The X-ray interrogation system developed by Passport Inc. exploits this difference in the energy spectra of photoneutrons to reduce false positives and efficiently identify fissionable materials.

Capture-based and scatter-based neutron detectors are often challenged by the intense high-energy photon source, which causes pulse pile-up. Neutron activation analysis (NAA) is a technique in which gamma-rays from (n,γ) reactions are counted to estimate photoneutron yields in various targets. The (n,γ) reaction is a threshold-based reaction, and therefore, by selecting appropriate isotope foils, the photoneutron spectrum information can be obtained. The physics of NAA makes this technique robust against pile-up and is often used to characterize photoneutron fluxes emitted from the high-Z X-ray converter target in linacs. Recently, the NAA technique has been used to measure photofission yields of ^{239}Pu, ^{235}U, and ^{238}U isotopes [25]. Delarue and colleagues used a 17.5 MeV bremsstrahlung photon beam to produce photoneutrons in Pu and U

isotopes and a n-type high-purity germanium (HPGe) detector to count gamma-rays from (n, γ) reactions in various foils. The various activation foils used were gold, nickel, uranium, zinc, and zirconium. In another study by Meert et al., an NAA technique was used to discriminate a SNM surrogate, such as depleted uranium, from a non-SNM material, such as lead [26].

The high-energy photon interrogation systems that rely on prompt photofission neutrons are quite promising for the detection of hidden SNMs. However, in a laboratory, it is difficult to test the performance of the system for field operations, such as cargo scanning at ports of entry. Restricted access to SNM, limited space, and regulatory concerns about high-energy photon sources are the limitations in a laboratory. Monte Carlo simulations that rely on photonuclear cross-section data are the best tools, which can help predict the response of the developed system in a real-like scenario. There is a growing concern about the reliability of results from Monte Carlo simulations, and therefore a need to validate photonuclear cross-sections [6,27].

1.2 Thesis Overview

In the current Ph.D. work, measurement of photoneutrons from various high-Z targets were performed. Photoneutrons were produced through bombardment of high-energy bremsstrahlung radiation from a pulsed source of 9-MV linac and detected with *trans*-stilbene organic scintillators. Lead, which produces photoneutrons through (γ, n) reactions, and depleted uranium (DU), which produces photoneutrons through (γ, n) and (γ, f) reactions, were interrogated with the linac. To mitigate the effect of pule pile-up during interrogation, I developed and demonstrated an ANN system for digital processing of scintillation pulses. The developed ANN system can identify single neutron pulses and recover neutron and photon information from piled-up events. The measured results were compared with the simulated results, which were obtained using the MCNPX-PoliMi [28–30] transport code. This detailed comparison provided a quantitative

assessment on the under-predictions in the photoneutron count rates obtained by Monte Carlo codes. A brief description of each chapter is provided below:

Chapter 2: The physics of photoneutron production is described in this chapter, followed by the physics of fast neutron detection with capture-based and scatter-based detectors. I further describe the digital acquisition system that is used to readout the scintillation light from organic scintillators.

Chapter 3: An overview of the fundamental concepts and principles of the ANN is provided, including their architecture, and learning algorithms. Additionally, common types of ANN are briefly described in this chapter.

Chapter 4: The training of the developed ANN system requires high-quality training data. This chapter provides detailed description of steps used to acquire high-confidence neutron and photon pulses from a time-of-flight measurement. Additionally, the chapter describes the synthesis of various types of piled-up events using the acquired neutron and photon pulses.

Chapter 5: In this chapter, I describe the architecture of the developed ANN system. Details on acquiring high-confidence neutron, photon, and piled-up pulses are provided, and the training process of the ANN system is explained. The ANN system performance was demonstrated through an experiment whose details are described. The chapter is concluded with a discussion on obtained results and accuracy of the developed ANN system.

Chapter 6: This chapter includes the measured results for photoneutron count rate from an unshielded depleted uranium target that was interrogated with bremsstrahlung photons from a 9-MV linac. The developed framework for MCNPX-PoliMi simulation is described. I discuss my findings from the detailed comparison of the simulated and measured photoneutron count

rates. This chapter concludes with a discussion on discrepancies observed between measurement and simulation.

Chapter 7: In this chapter, I present measured results for photoneutron count rates from depleted uranium, which was shielded in various iron and polyethylene configurations. The experiment was modeled with the developed MCNPX-PoliMi framework. A detailed comparison made between the measured and simulated results provided a quantitative information on the under-predictions in the photonuclear cross-section data for uranium.

Chapter 8: This chapter presents the overall summary and conclusions and provide recommendations for future work.

Chapter 2 Photoneutrons: Production and Detection

The physics of photoneutron production is discussed in this chapter, followed by the physics of fast neutron detection with capture-based and scatter-based neutron detectors. Additionally, the digital data acquisition system used to readout voltage signals from detectors is described. The goal of this chapter is to provide fundamental knowledge about photoneutrons and their detection.

2.1 Photoneutron Production

Photons with sufficient energy to overcome the neutron binding energy can cause photonuclear reactions, such as (γ, Xn). The photonuclear reactions are governed by broad resonances known as giant dipole resonances, and the probability of the reaction is maximum at the resonance peak energy. For a low-Z material like ^{9}Be, the resonance peak is at 20 MeV, and for a high-Z material like ^{208}Pb, the resonance peak is at 14 MeV. For most actinides, the resonances peak between 10 and 15 MeV.

There are two possible types of photonuclear reactions i.e., (γ, n) and (γ, f) for photon energies below 10 MeV. Figure 2.1 shows the cross-section data for the (γ, n) and (γ, f) reactions. The threshold energy for (γ, n) reactions varies with the target element. This threshold is 1.66 MeV and 7.37 MeV for ^{9}Be and ^{208}Pb respectively [31]. Special nuclear material (SNM), such as ^{235}U, have a threshold of 5.30 MeV for (γ, n) reactions [31]. Additionally, SNM can undergo photofission reactions i.e., (γ, f) resulting in the emission of prompt and delayed fission neutrons.

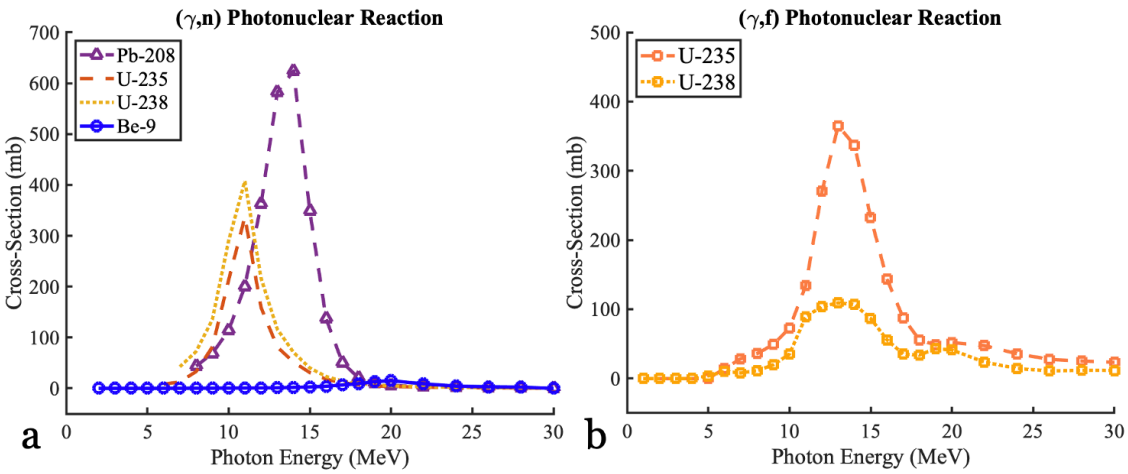

Figure 2.1. TENDL-2019 cross-section data for a) (γ, n) photonuclear reactions and b) (γ, f) photonuclear reactions [31].

Fission reactions have a higher multiplicity than (γ, n) reactions, which have a multiplicity of one. For an interrogating gamma-ray energy of 7 MeV, the prompt fission neutron yield is 2.54 and 2.72 for ^{235}U and ^{238}U isotopes respectively [32,33]. The yield of photofission reaction and prompt neutrons increases with photon energy (Figure 2.3 and Figure 2.2). Additionally, fission neutrons and (γ, n) neutrons are emitted with different energy spectra. Figure 2.4 shows the difference in the energy spectrum of photoneutrons produced by (γ, f) and (γ, n) reactions. Photoneutrons through (γ, n) reactions have a maximum kinetic energy, which is determined by the incoming photon energy and the reaction Q-value. For photon energies that exceed the minimum threshold energy for (γ, n) reaction, the corresponding photoneutron energy is given by,

$$E_n(\theta) \cong \frac{M(E_\gamma + Q)}{m + M} + \frac{E_\gamma \sqrt{(2mM)(m + M)(E_\gamma + Q)}}{(m + M)^2} \cos(\theta) \qquad 2\text{-}1$$

where θ = angle between interrogating photon and neutron direction,

E_γ = photon energy,

M = mass of recoil nucleus $* c^2$, and

m = mass of neutron $* c^2$.

However, prompt fission neutrons, emitted with a Watt energy spectrum [34], have energies up to 10 MeV and beyond.

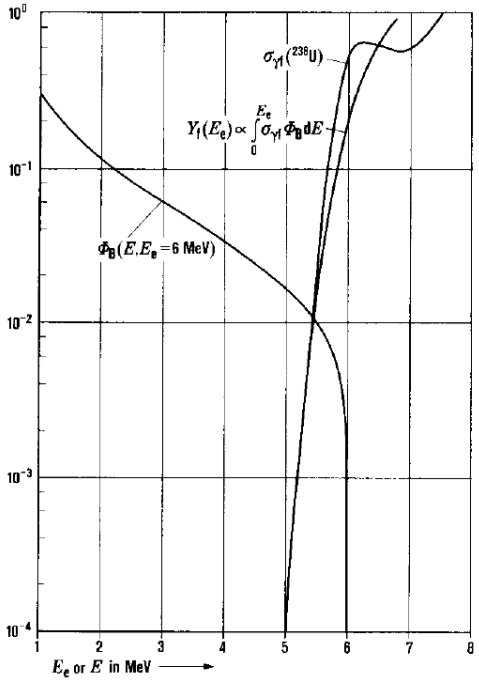

Figure 2.2. Yield of photofission as a function of bremsstrahlung photon energy [33]. $\phi_B(E)$ is the energy spectrum of bremsstrahlung photons, $\sigma_{\gamma f}$ is the photofission cross-section, and $Y_f(E)$ is the photofission yield.

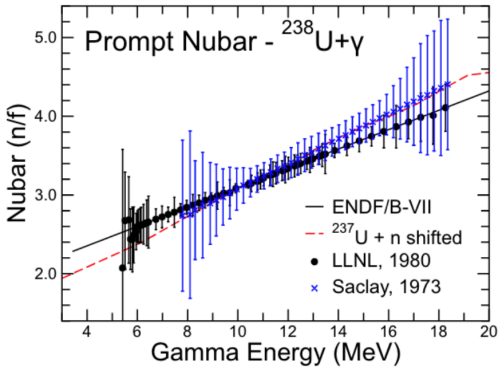

Figure 2.3. Prompt neutron yield per photofission reaction for photons incident on ^{234}U [7].

Electron linear accelerators (linacs) are commonly used to produce high-energy photons for photonuclear reactions. The linac uses electric and magnetic fields to accelerate electrons into a conversion target. These fast electrons lose energy by radiative processes as they decelerate in the conversion target, resulting in the emission of bremsstrahlung photons. In general, linacs operate in pulsed mode, i.e., emitting bremsstrahlung photons in pulses of a duration between a few microseconds and a few milliseconds at a given repetition frequency [35]. The pulsed nature of the linac can facilitate separation of prompt fission neutrons from delayed neutrons, which are produced through β-decay of photofission fragments.

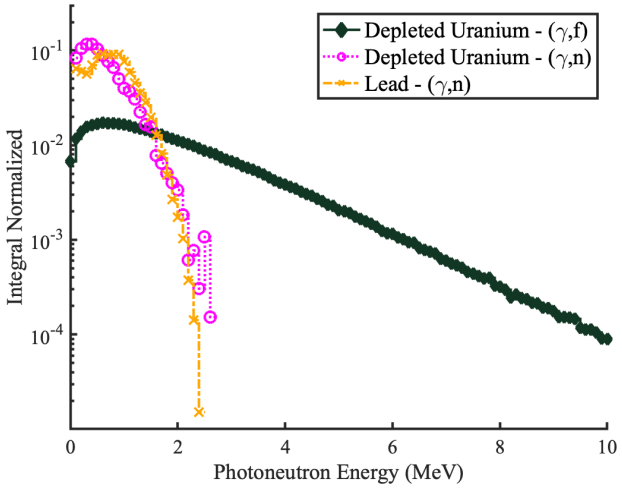

Figure 2.4. Energy spectrum of photoneutrons produced because of (γ, f) and (γ, n) photonuclear reactions. These distributions are simulated using the MCNPX-PoliMi transport code.

2.2 Photoneutron Detection

The photoneutrons from (γ, n) and (γ, f) reactions are fast neutrons, which are emitted promptly after the incident pulse of high-energy photons. Capture-based detectors e.g., ^{3}He, and scatter-based detectors e.g., organic scintillators are widely used for neutron detection. Neutrons are neutral particles that are detected through secondary interactions. The choice of neutron detectors is based on several factors, which includes cross-section for the secondary interaction, the Q-value of the reaction, the ability to discriminate gamma-rays in the detection process, and

the efficiency of the detectors. The physics of capture-based and scatter-based neutron detectors is described in sections below.

2.2.1 Capture-based detectors

In capture-based detectors, the neutron is absorbed by the target nucleus resulting in the emission of charged particles. These charged particles are directly detectable with conventional radiation detectors, such as gas-filled proportional counters. The commonly used nuclei for neutron-capture reactions are ^{3}He, ^{10}B, and ^{6}Li.

$$^{3}_{2}He + ^{1}_{0}n \rightarrow ^{3}_{1}H + ^{1}_{1}p \qquad Q = 0.764\ MeV$$

$$^{10}_{5}B + ^{1}_{0}n \rightarrow \begin{cases} ^{7}_{3}Li + ^{4}_{2}\alpha & Q = 2.792\ MeV\ (ground\ state) \\ ^{7}_{3}Li^{*} + ^{4}_{2}\alpha & Q = 2.310\ MeV\ (excited\ state) \end{cases}$$

$$^{6}_{3}Li + ^{1}_{0}n \rightarrow ^{3}_{1}H + ^{4}_{2}\alpha \qquad Q = 4.78\ MeV$$

Figure 2.5 shows the cross-section data for some reactions of interest in neutron detection. The cross-section drops rapidly with increasing neutron energy, and therefore, these detectors are mainly used for thermal neutron detection. The photoneutrons from (γ, Xn) reactions are fast neutrons and require moderation for their efficient detection. The moderating process eliminates the information on the neutron energy and further slows down its detection. In intense photon environments, reactions with higher Q-values are desired because it is relatively easy to discriminate gamma-ray interactions within the detector using simple amplitude discriminator.

The size of the detector and the amount of moderation present have important consequences on the detector design. To capture the full kinetic energy of charged particles, the active volume must be large enough to stop these particles within the detector. If one of the charged particles escapes the active volume, then wall losses are observed, i.e., partial energy deposition by the charged particle. Another consideration is the amount of neutron moderator present around

the detector. The slowing-down of the neutron to thermal energies and its lifetime in the moderator determines the response time of the detector. The capture-based detectors used for fast neutron detection have a typical timing response on the order of microseconds.

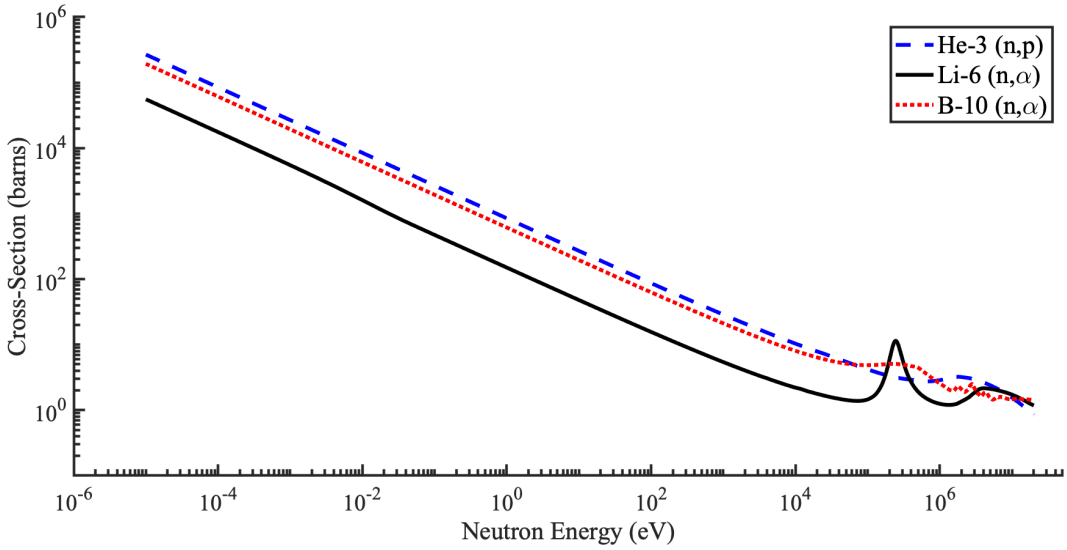

Figure 2.5. ENDF/B-VII cross-section data for neutron-capture reactions in various nuclei of interest.

2.2.2 Scatter-based detectors

Figure 2.6 shows the cross-section data for neutron elastic scatter on hydrogen, deuterium, and helium. At thermal energies, the cross-section for neutron elastic scatter is orders of magnitude lower than the neutron capture reaction. This lower cross-section has a direct consequence on the detection efficiency. The benefit of scatter-based detectors is their ability to perform spectroscopy. The electrical signal that is constituted by the recoil nucleus is directly proportional to the energy deposited by incoming neutrons. Additionally, direct detection of fast neutrons without any moderation makes detection times relatively faster than capture-based detectors.

The neutron transfers partial of its initial kinetic energy on elastic scatter with a target nucleus, resulting in a recoil nucleus. Hydrogen, deuterium, and helium are preferred target nuclei because neutrons can transfer most of their energy in a single elastic scatter. The amount of energy

transferred to recoil nucleus depends on the scattering angle and mass number of the target nucleus. Equation 2-2 gives the relation for the recoil nucleus energy in terms of its own angle of recoil.

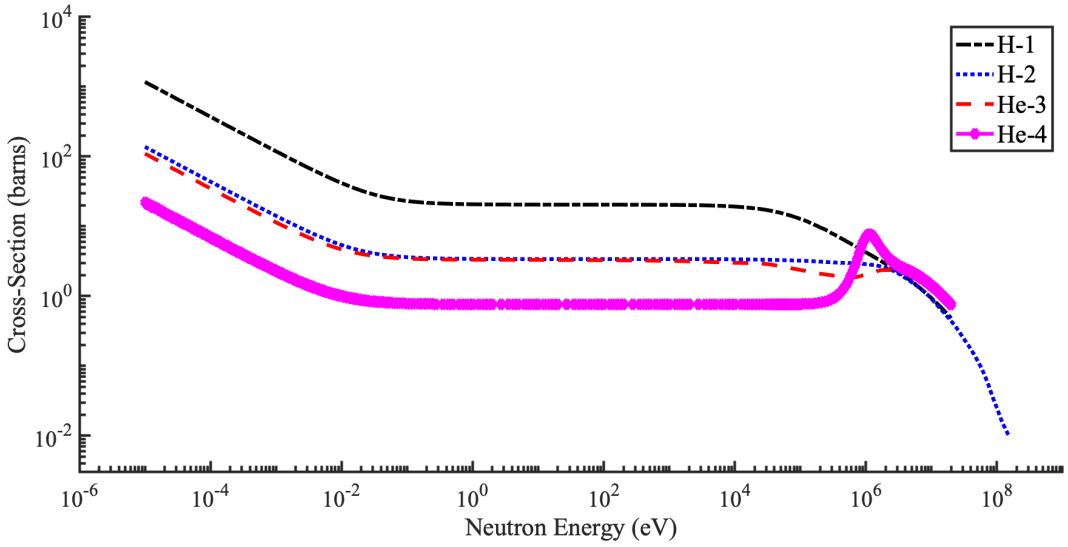

Figure 2.6. ENDF/B-VII cross-section data for neutron elastic scatter.

$$E_R = \frac{4A}{(1+A)^2}.\cos^2\theta\,.E_n \qquad 2\text{-}2$$

where E_R = kinetic energy of the recoil nucleus,

A = mass number of target nucleus,

θ = scattering angle of the recoil nucleus, and

E_n = kinetic energy of the incoming neutron.

The maximum recoil energy is when the incoming neutron undergoes head-on collision i.e., $\theta = 0$ with the target nucleus. Table 2.1 shows the maximum energy transferred by a neutron during elastic scatter with target nucleus. For a single scatter on ${}_1^1H$, neutrons can transfer any energy between 0% and 100% and therefore, organic scintillators are best suited for neutron spectroscopy. Additionally, organic scintillators have time resolution on the order of nanoseconds [36], which is an added benefit for photoneutron detection.

Table 2.1: Maximum energy transferred during elastic scattering of neutron with target nucleus.

Target nucleus	Mass number (A)	$\frac{E_{R_{Max}}}{E_n} = \frac{4A}{(1+A)^2}$
${}^{1}_{1}H$	1	1
${}^{2}_{1}H$	2	0.889
${}^{3}_{2}He$	3	0.750
${}^{4}_{2}He$	4	0.640
${}^{12}_{6}C$	12	0.284
${}^{16}_{8}O$	16	0.221

2.2.3 Organic scintillators

Organic scintillators are state-of-the-art fast neutron detectors with spectroscopy capabilities and fast timing characteristics. In organic scintillators, the prompt fluorescence (decay time of a few nanoseconds) represents most of the scintillation light. However, in many cases delayed fluorescence emitted with a decay time of several hundred nanoseconds is observed. This fraction of light that appears in the slow component of the scintillation pulse helps differentiate between different particles that deposit the same amount of energy in the scintillator i.e., pulse shape discrimination (PSD). Figure 2.7 shows the time dependence of the prompt and delayed fluorescence in the *trans*-stilbene scintillator when photons, fast neutrons, and alpha particles interact within the scintillator. The slow component of the scintillation pulse originates with the excitation of long-lived triplet states along the track of the ionizing particle, and depend on the rate of energy loss i.e., dE/dx of the exciting particle.

In the organic scintillator, fast neutrons are detected through elastic scatter (proton and carbon recoils) and photons are detected through Compton scatter (electron recoil). PSD is commonly achieved using a charge integration technique, which exploits the difference in the slow

component of the scintillation pulse for neutron and photon discrimination. The charge integration method compares the tail and total integrals of the scintillation pulse to a discrimination line to classify each detected event. Figure 2.8a illustrates the charge integration method, and Figure 2.8b shows a typical PSD distribution, which is obtained using a 5.08 cm in length and 5.08 cm in diameter *trans*-stilbene crystal coupled to a photomultiplier tube.

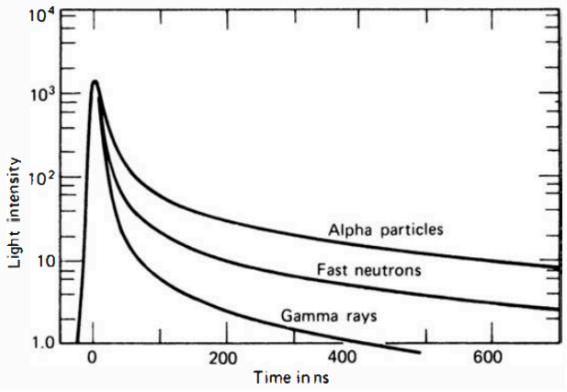

Figure 2.7. Time dependence of prompt and delayed fluorescence for different particles in the *trans*-stilbene crystal [37].

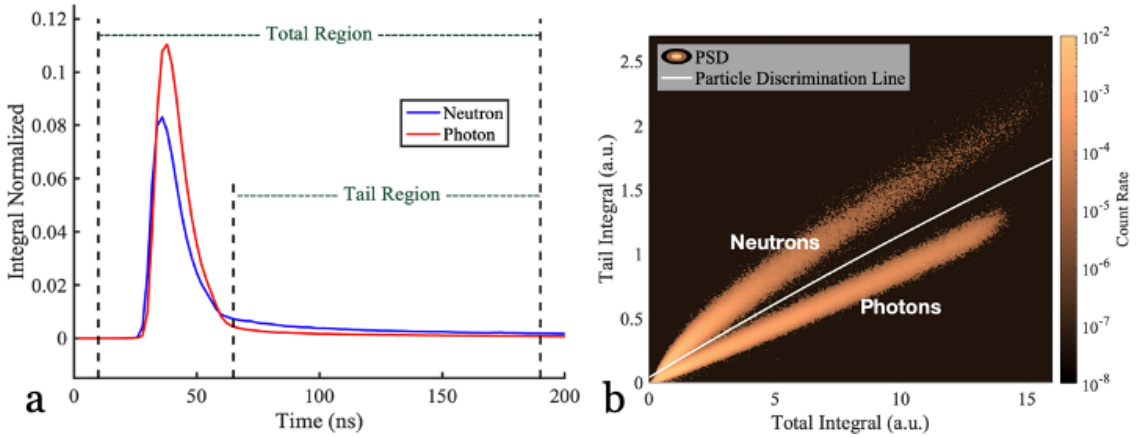

Figure 2.8. a) Traditional charge integration method for PSD analysis and b) PSD plot for a ^{252}Cf spontaneous fission source (measured with a 5.08 cm in length and 5.08 cm in diameter t*rans*-stilbene detector).

The fraction of particle energy that is converted to scintillation light depends on the particle type i.e., electron versus proton versus carbon, and its energy. Figure 2.9 shows a typical scintillation response to electrons, protons, and alpha particles. For electrons, the scintillation response is nearly linear. However, for heavy charged particles, such as protons, the scintillation

response increases non-linearly with energy. This non-linear response is due to the quenching of primary excitation by the high density of ionized and excited molecules. The quenching is greatest for particles with large dE/dx. The Birks function, represented in eq. 2-3, can be used to account for the quenching effect in the *trans*-stilbene scintillator.

$$L(E) = \int \frac{a}{1 + b\left(\frac{dE}{dx}\right)} dE \qquad 2\text{-}3$$

where $L(E)$ = light output in MeVee (MeV electron equivalent, i.e., the amount of light created by a photon energy deposition in MeV),

dE/dx = particle stopping power in the scintillator, and

a and b = fitted coefficients.

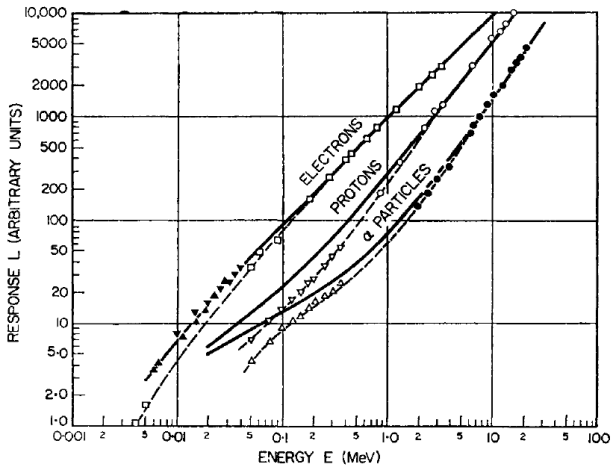

Figure 2.9. Scintillation response to electrons, protons, and α-particles (anthracene organic scintillator) [38].

2.2.4 Scintillation Light Readout

Figure 2.10 shows a block diagram to read the scintillation light from organic scintillators. The scintillation light is read through a photomultiplier tube (PMT). A PMT consists of a photodiode that converts the emitted light to a photoelectron, and an electron multiplier, which uses an electric field to accelerate electrons into a dynode. The collision of electrons with the dynode releases several new electrons, which are accelerated into another dynode. After

amplification through dynodes, there are sufficient electrons to serve as the charge for the original scintillation light. This charge is then collected at the anode of the PMT. For all measurements performed in the present Ph.D. research, the *trans*-stilbene crystal coupled to a 5.08 cm in diameter PMT from ET Enterprises [39] were used. The *trans*-stilbene crystals were from Inrad Optics [40] and the dimensions were 5.08 cm in length and 5.08 cm in diameter. Figure 2.11 shows the photograph of the scintillator and the PMT used in this work.

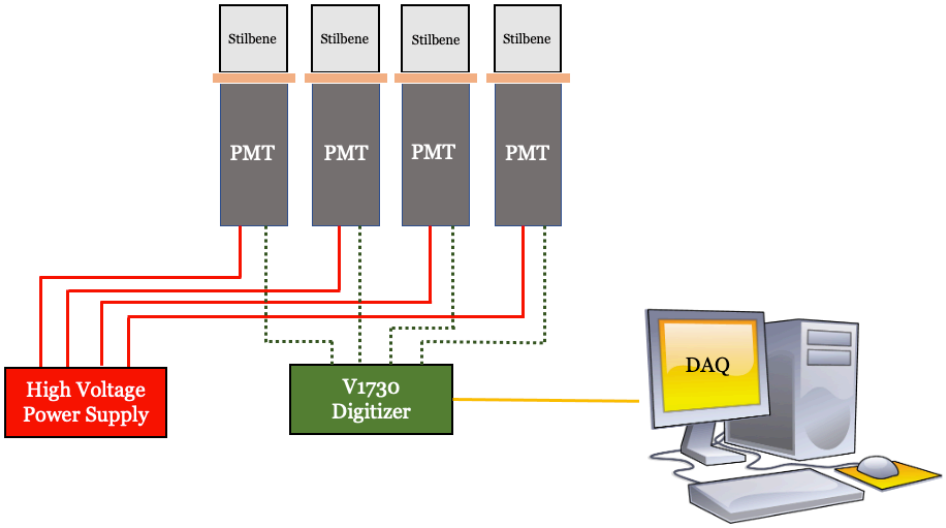

Figure 2.10. Block diagram for reading scintillation light from *trans*-stilbene crystals.

Figure 2.11. Photograph of the 5.08 cm in length and 5.08 cm in diameter *trans*-stilbene crystal and a 5.08 cm in diameter photomultiplier tube.

The charge from the anode of the PMT is digitized using a high-speed multichannel analog-to-digital converter (ADC). The digitizer used in this work was a V1730 14-bits, 500 MS/s digitizer

from CAEN [41] (Figure 2.12). The 500 MS/s rate samples scintillation pulse data every 2 ns, and 14-bits provides a vertical resolution of $2^{14} = 16384$ voltage bins. These digitizers have a dynamic range of 0 to 2 V, and therefore the voltage bins can be converted from ADC units to volts using,

$$S_{Volts} = S_{ADC} * \left(\frac{2}{2^{14}}\right). \quad 2\text{-}4$$

where S_{Volts} = voltage in units of volts, and

S_{ADC} = voltage in units of ADC.

All digitized data were transferred to the data acquisition computer (DAQ) using an optical cord and was saved locally on the DAQ for future processing.

Figure 2.12. Photograph of the V1730 digitizer from CAEN [41].

Chapter 3 Artificial Neural Networks

Artificial neural networks (ANNs) are a type of machine learning model inspired by the structure and function of the human brain [42]. ANNs have become increasingly popular in recent years due to their ability to model complex relationships between inputs and outputs. ANNs consist of layers of interconnected nodes, each of which performs a simple computation on its inputs. Through training, ANNs can learn to recognize patterns and make predictions on new data. In this chapter, an overview of the fundamental concepts and principles of ANNs is provided, including their architecture, and learning algorithms.

3.1 Architecture of Artificial Neural Networks

An ANN is comprised of an input layer, one or more hidden layers, and an output layer (Figure 3.1). Each layer consists of several neurons, which combine an input signal and compare its value to a threshold to estimate an output. The input layer receives a set of numerical values representing features of the problem being solved. These input data are then passed through a series of hidden layers. A simple mathematically model for any layer can be represented using a linear regression.

$$B + \sum w_i x_i \qquad 3\text{-}1$$

$$Ouput = f(L) = \begin{cases} 1\ if\ \sum w_i x_i + B \geq 0 \\ 0\ if\ \sum w_i x_i + B < 0 \end{cases} \quad 3\text{-}2$$

where w_i = weight of the neuron,

x_i = numerical value entering neuron, and

B = bias value.

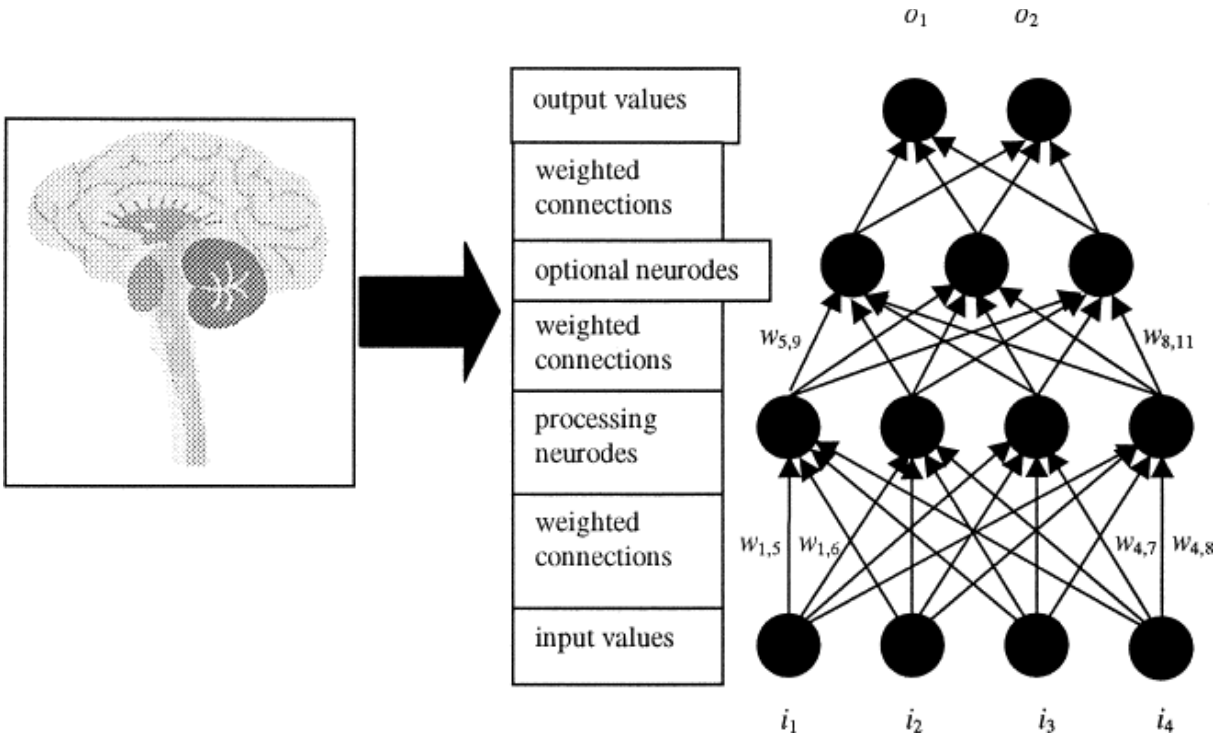

Figure 3.1 Structure of an artificial neural network inspired from human brain [42].

Once a layer is determined, weights are assigned. These weights represent the importance of any given variable, with larger ones contributing more significantly to the output compared to other inputs. All inputs are then multiplied by their respective weights and then summed (eq. 3-1). The solution of eq. 3-1 is passed through an activation function (eq. 3-2), which determines the final output. The activation function introduces non-linearity into the network, allowing it to model

complex relationships between the input and output data. If the output of the activation function exceeds a given threshold, its "fires" (or activates) the neuron, passing data to the next layer in the network. This results in the output of one neuron becoming the input of the next neuron.

Optimizing the appropriate number of hidden layers for an ANN requires careful consideration of the complexity of the problem, the size of the dataset, and prior knowledge of the problem domain. The number of hidden layers and the number of neurons in each hidden layer can have a significant impact on the performance of the network. Starting with a simple architecture, such as a single hidden layer with a few neurons, will help establish the baseline performance of the ANN. A validation dataset is used to evaluate the performance of the developed architecture. The decision to increase the number of hidden layers and number of neurons is informed by the performance of the network on this validation dataset.

Table 3.1. Mathematical equation for various activation functions used in ANN [43].

Function	Equation
Sigmoid	$f(L) = \frac{1}{1 + e^{-(B+\sum w_i x_i)}}$
Hyperbolic Tangent	$f(L) = \frac{e^{(B+\sum w_i x_i)} - e^{-(B+\sum w_i x_i)}}{e^{(B+\sum w_i x_i)} + e^{-(B+\sum w_i x_i)}}$
Softmax	$f(L) = \frac{e^{(B+\sum w_i x_i)}}{\sum_{m=0}^{M-1} e^{(B+\sum w_i x_i)_m}}$, where M is the categories of responses
Softplus	$f(L) = \ln\left[1 + e^{(B+\sum w_i x_i)}\right]$
Rectifier linear unit	$f(L) = \begin{cases} 1 \; if \; \left[B + \sum w_i x_i\right] \geq 0 \\ 0 \; if \; \left[B + \sum w_i x_i\right] < 0 \end{cases}$

Choosing the appropriate activation function is also important when designing an ANN. The choice of activation function depends on the specific requirements of the problem. The decision on a specific function can be made after trying out different activation functions to see which one works best for the application. Some commonly used activation functions are represented in Table 3.1.

3.2 Learning Algorithms

After defining the ANN architecture, it is trained with real data. The training can be performed in an unsupervised or a supervised fashion. In unsupervised training, no prior knowledge of the output is needed. The network discovers patterns in data without the need for a pre-labeled output. In supervised training, a set of pre-labeled input and output data is needed. The network learns from the training data by iteratively making predictions on the data and adjusting for the correct answer. The self-organizing map (SOP) is a widely used unsupervised training method in which an input space of training samples is processed to lower its dimensions by clustering of similar samples [44]. The backpropagation algorithm is a widely used supervised training method, which is an iterative training process until a threshold criterion is satisfied [44].

3.2.1 Self-Organizing Map

In 1982, Kohonen explained the process of self-organizing maps (SOMs) [45]. One of the key features of SOMs is their ability to create a two-dimensional map that preserves the topological relationships between the input vectors. This means that similar input vectors are mapped to nearby neurons in the SOM, while dissimilar input vectors are mapped to neurons that are further apart. This property allows SOM to be used for data visualization and exploration, as the two-

dimensional map can provide a high-level overview of the input data and reveal hidden structures and relationships.

SOMs are a type of ANN that is commonly used for unsupervised learning tasks, which means that they do not require pre-labeled data for training. Unsupervised training makes them particularly useful for tasks where labeled data is difficult to obtain. Another advantage of SOM is its computational efficiency. SOMs can be trained on large datasets in a reasonable amount of time.

The objective of Kohonen's learning algorithm is that each neuron learns to specialize in different regions of input space. When an input from such a region is fed into the network, the corresponding neuron should compute the maximum excitation. This maximum excitation is achieved by computing the Euclidean distance between an input X and its weight vector W. Kohonen learning uses a function $\phi(i,k)$, which represents the strength of the coupling between neuron i and neuron k during the training process. A simple choice is defining $\phi(i,k) = 1$ for all neuron i in a neighborhood of radius r of unit k and $\phi(i,k) = 0$ for all other neurons. The learning algorithm for Kohonen networks is described below [46].

Start: The n-dimensional weight vector $(w_1, w_2, \dots, w_k)$ of the m computing units are randomly generated. An initial radius r, a learning constant η, and a neighborhood function ϕ are selected.

Step 1: Select an input vector X using the desired probability distribution over the input space.

Step 2: The unit k with the maximum excitation is selected i.e., the distance between w_i and X is minimal, $i = 1,2,\dots,m$.

Step 3: The weight vectors are updated using the neighborhood function and the update rule,

$$w_i \leftarrow w_i + \eta\phi(i,k)(X - w_i), \qquad for\ i = 1,2,\dots,m$$

Step 4: Stop if the maximum number of iterations has been reached; otherwise modify η and ϕ, and continue with step 1.

By repeating the above steps several times, a uniform distribution of weight vectors in the input space is achieved. During the learning process, both the size of the neighborhood and the value of ϕ fall gradually, so that the influence of each neuron upon its neighbors is reduced. The learning constant controls the magnitude of the weight updates and is also reduced gradually.

3.2.2 Backpropagation Algorithm

The backpropagation algorithm is based on the principle of gradient descent, which is a method for finding the minimum of a cost function by iteratively adjusting the weights in the direction of the steepest descent. The algorithm works by propagating the error (the difference between the predicted output and the actual output) backwards through the network, starting from the output layer and moving towards the input layer. At each layer, the error is multiplied by the derivative of the activation function (which determines the output of each neuron), and then the resulting values are used to update the weights of the connections between neurons. This process is repeated for each training example, and the weights are adjusted until the error is minimized. For a simple ANN with a single input and a single output neutron, the backpropagation algorithm can be formulated as follows [46]:

Consider a network with a single input x and activation function F. The derivation $F'(x)$ is computed in two phases:

Feed-forward The input x is fed into the network. The primitive functions at the neurons and their derivatives are evaluated at each neuron. The derivatives are stored.

Backpropagation: The constant 1 is fed into the output neuron and the network is run backwards. Incoming information to a neuron is added and the result is multiplied by the value stored in the left part of the neuron. The result is transmitted to the left of the neuron. The result collected at the input neuron is the derivative of the network function with respect to x.

Figure 3.2 shows an example of a multilayer ANN for computation of the error function. For simplicity, a single input-output pair (o, t) is considered. Moving from right to left in Figure 3.2, the quadratic deviation i.e., $\frac{1}{2}(o_i^{(2)} - t_i)$ for the i^{th} component of the output vector is computed. Each output neuron i in the network produces the output $o_i^{(2)}$ using the activation function s. Additions of the quadratic deviations give the error function E. The training of the network stops after the value of the error function is reduced below a user-specified value. The training can also be stopped if the error between two consecutive epochs, $n-1$ and n, is not significantly reduced.

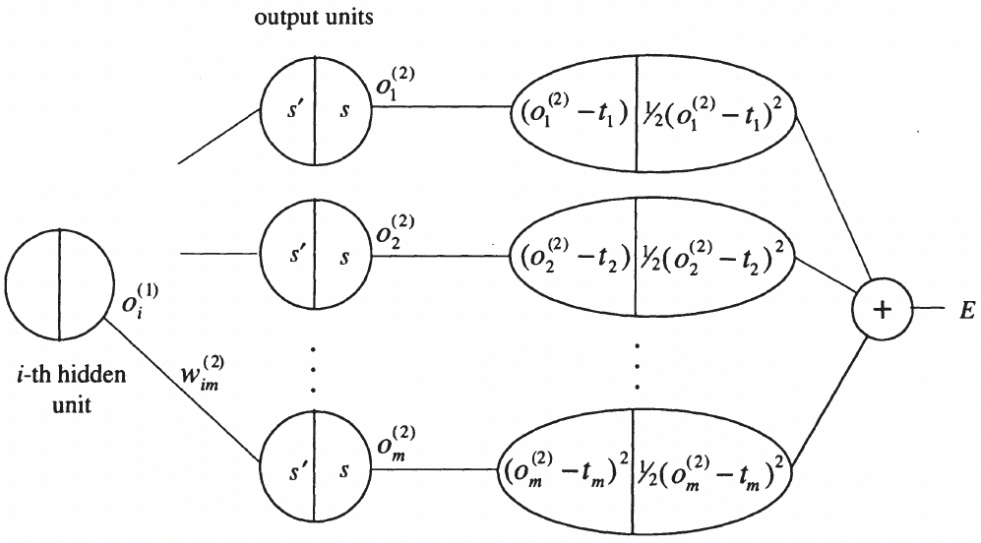

Figure 3.2. An example of a multilayer ANN for computation of the error in the propagation algorithm [46].

Initially, the weights of the network are selected randomly. The backpropagation algorithm computes the necessary corrections using the following four steps.

1. Feed-forward computation
2. Backpropagation to the output layer
3. Backpropagation to the hidden layer
4. Weight updates

In the first step, the input vector o is presented to the ANN. The output vectors $o^{(1)}$ i.e., output of the hidden layer, and $o^{(2)}$ i.e., output of the network, are computed. The derivatives of the activation function at each neuron are also computed and stored. In the second step, the partial derivative of the error function E is computed using,

$$\frac{\partial E}{\partial w_{ij}^{(2)}} = \left[o_j^{(2)}\left(1 - o_j^{(2)}\right)\left(o_j^{(2)} - t_j\right)\right] o_i^{(1)} = \delta_j^{(2)} o_i^{(1)}. \quad \text{3-3}$$

where $w_{ij}^{(2)}$ = the weight between hidden layer i and output layer j, and

$\delta_j^{(2)}$ = backpropagated error to the output layer.

Similarly, in the third step, backpropagated error to the hidden layer is computed using,

$$\frac{\partial E}{\partial w_{ij}^{(1)}} = \left[o_j^{(1)}\left(1 - o_j^{(1)}\right)\sum_{q=1}^{m} w_{jq}^{(2)} \delta_q^{(2)}\right] o_i = \delta_j^{(1)} o_i. \quad \text{3-4}$$

where $w_{ij}^{(1)}$ = the weight between input layer i and hidden layer j, and

$\delta_j^{(1)}$ = backpropagated error to the hidden layer.

After computing all partial derivatives, the ANN weights are updated in the negative gradient direction. A learning constant γ defines the step length of the correction. The corrections for the weights are given by,

$$\Delta w_{ij}^{(2)} = -\gamma o_i^{(1)} \delta_j^{(2)}, \qquad for\ i = 1,..,k+1; j = 1,\dots,m \tag{3-5}$$

$$\text{and } \Delta w_{ij}^{(1)} = -\gamma o_i \delta_j^{(1)},\ for\ i = 1,..,n+1; j = 1,\dots,k \tag{3-6}$$

where k = number of hidden layers,

m = number of output neurons, and

n = number of input neurons.

It is very important to make the corrections to the weights only after the backpropagated error has been computed for all neurons in the network. Otherwise, the corrections become intertwined with the backpropagation of the error and the computed corrections do not correspond any more to the negative gradient direction.

3.3 Types of Artificial Neural Network

There are several types of ANNs, each with its unique architecture and functions, such as feedforward neural networks, recurrent neural networks, convolutional neural networks, and more. The choice of which type of neural network to use depends on the specific task and input data. While the list below is not comprehensive, it is representative of the most common types of neural networks.

3.3.1 Feedforward Neural Networks

Feedforward neural networks (FNN) are the most commonly applied ANN, where information flows in one direction, from input to output. It consists of an input layer, one or more hidden layers, and an output layer. The sigmoid activation function is commonly used for non-linearity. Data is fed into these models to train them. FNNs are often used for pattern recognition, classification, and regression tasks. FNNs are a powerful and versatile type of neural network that

offer several advantages for machine learning and artificial intelligence applications. Their ability to handle large and complex data, generalize well, perform parallel processing, perform non-linear mapping, and learn quickly make them an essential tool in modern data analysis and predictive modeling.

3.3.2 Convolutional Neural Networks

Convolutional neural networks (CNN) are primarily used for image and video analysis. They have a hierarchical structure consisting of convolutional and pooling layers that help to identify patterns in the input data. The hierarchical structure allows them to identify features such as edges, textures, and shapes, which can then be used to recognize objects and scenes in the input data. CNNs are designed to be invariant to translations in the input data i.e., the network can recognize an object in an image regardless of where it appears in the image. This invariance is particularly useful for tasks such as object detection and recognition, where the position and orientation of an object can vary. Another advantage of CNN is their ability to learn from small datasets, which makes them particularly useful in applications where acquiring large amounts of training data is difficult.

3.3.3 Recurrent Neural Networks

Recurrent neural networks (RNN) are identified by their feedback loops. These learning algorithms are primarily leveraged when using time-series data to make predictions about future outcomes, such as stock market predictions or sales forecasting. RNNs are a powerful and versatile type of neural network that offer several advantages for tasks that involve sequential data. Their memory component, flexibility, ability to capture temporal dynamics, parallel processing, and

transfer learning capabilities make them an essential tool in modern natural language processing, speech recognition, and other sequential data analysis applications.

3.3.4 Modular Neural Networks

Modular neural networks (MNN) consist of multiple smaller neural networks that are interconnected and work together to solve a larger problem. They are often used in robotics and control systems. MNNs can be designed with a modular architecture, reusable modules that can be used across different tasks and applications, and interpretable modules. The reusability makes MNN effective for applications where similar tasks are performed across different domains. The interpretability makes MNN effective for applications such as medical diagnosis, where interpretability is critical.

Chapter 4 Training Data for Artificial Neural Network System

Artificial neural networks (ANNs) require high-confidence training data that can be used by the network to learn and make predictions. The ANN system developed in this dissertation was trained with experimental data acquired through dedicated measurements. This chapter provides details of the measurement setup and detailed description of steps involved in data processing. The goal of this chapter is to provide a framework that can used to create high-quality training dataset for ANNs.

4.1 Time-of-Flight Measurement Setup

A time-of-flight (TOF) measurement was performed to acquire high-confidence neutron and photon scintillation pulses for the training of the ANN system. Two 5.08 cm in length and 5.08 cm in diameter *trans*-stilbene organic crystals coupled to a 5.08 cm in diameter photomultiplier tube (PMT) were used for the TOF measurement. The scintillators were placed across one another at 1 m. A ^{252}Cf spontaneous fission source was placed very close to the start detector in the TOF measurement. Figure 4.1 shows the photograph of the TOF measurement setup.

The ^{252}Cf source decays through α-decay (branching ratio of 96.91%) and spontaneous fission (branching ratio of 3.09%). To reduce the contribution of gamma-rays produced during the decay of ^{252}Cf, the detectors were placed in a lead cave. The lead cave was constructed with standard 5.08 cm x 10.16 cm x 20.32 cm (2” x 4” x 8”) bricks. Lead is a high-Z material, which

shields gamma-rays and has a minimal effect on neutron energy moderation. This lead shielding reduces the detection of gamma-rays in the start and stop detectors, which aids in determining the particle discrimination line at low tail and total integral values where neutrons and gamma-rays overlap (Figure 2.8). The TOF measurement setup was placed in the center of the room and 1.6 m from the floor to reduce room-return i.e., scattered neutrons and gamma-rays reflected from room surfaces, such as sidewalls, ceiling, and floor.

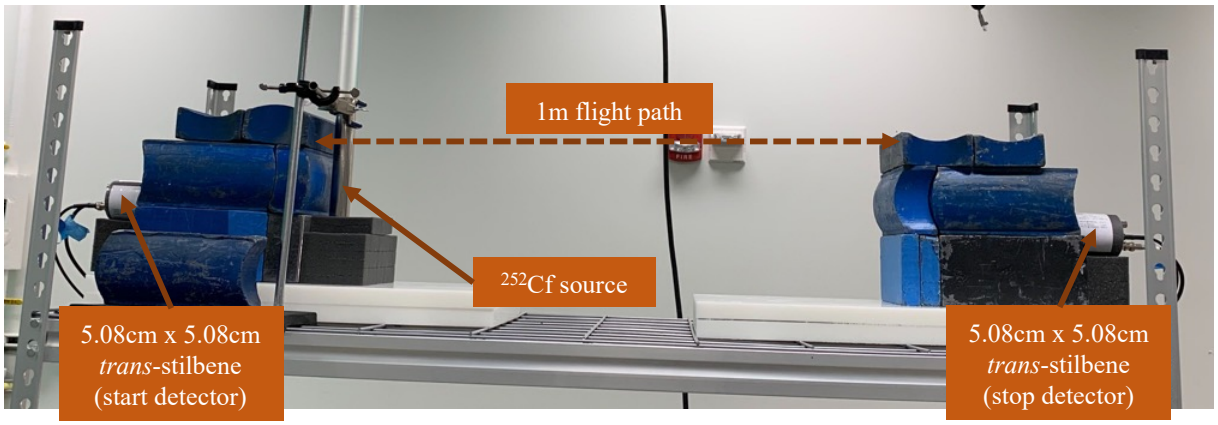

Figure 4.1. Photograph of the time-of-flight measurement setup that is used to acquire high-confidence neutron and photon scintillation pulses.

Figure 4.2. Data format of the output .dat file. Information contained in green boxes are used for data processing. $recordLength$ is the number of waveform samples in each scintillation pulse.

Scintillation pulses from the *trans*-stilbene detector were digitized using a V1730 14-bits, 500 MS/s digitizer from CAEN [41]. An onboard coincidence logic was setup. The logical AND operation would write detection events to file if and only if the start detector and the stop detector triggered within 250 ns. The output file was saved in a .dat format, which is a binary format. The structure of the output file is shown in Figure 4.2.

4.2 Data processing

4.2.1 Time-of-Flight Histogram

The .dat binary file from the TOF measurement was read using a C++ program. For every detected event in the start and stop detectors, the corresponding time tag, channel number, and waveform samples were extracted and saved in an array. A fine time stamp was determined using the digital constant fraction discrimination (DCFD) method. In this method, a constant fraction i.e., 0.5 of the pulse amplitude was used to determine the fine time stamp. The detection time of radiation events in the start and stop detectors was obtained by summing the coarse time tag from the digitizer and the fine time tag determined using DCFD.

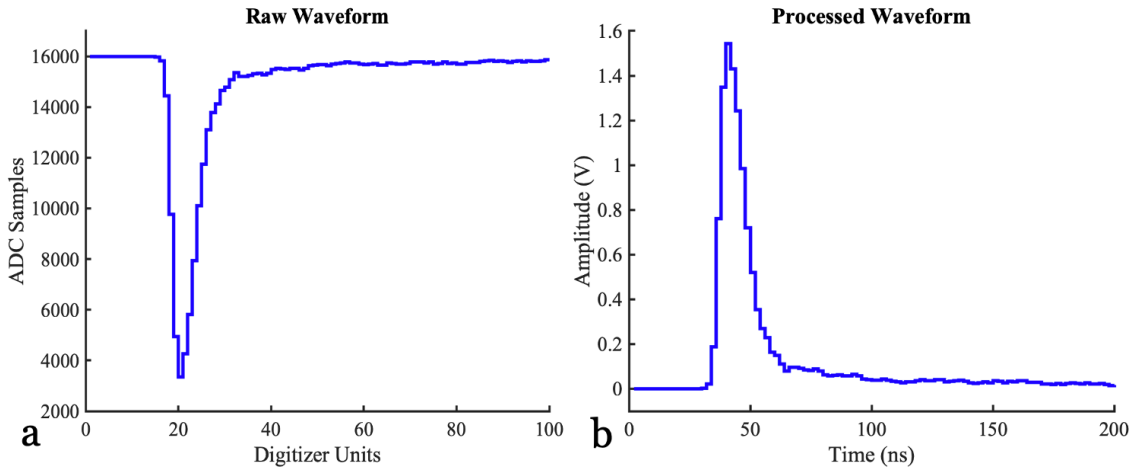

Figure 4.3. a) Raw waveform from CAEN digitizer and b) inverted and baseline corrected waveform.

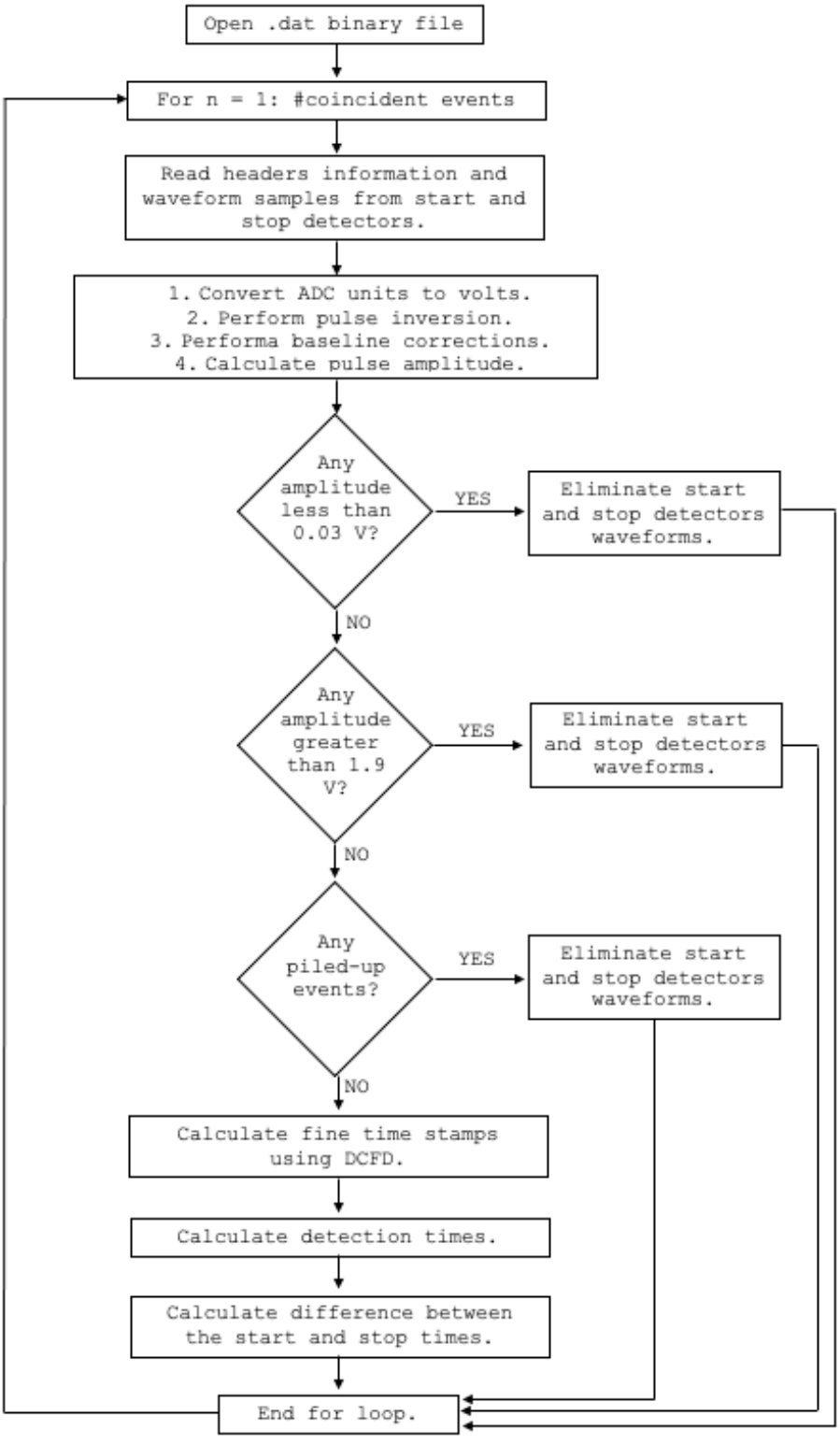

Figure 4.4. Pulse processing algorithm used for the time-of-flight data analysis.

The scintillation pulse samples were first converted from ADC units to volts using eq. 2-4. The pulses were then inverted from negative polarity to positive polarity using,

$$S_{positive} = (-1) * S_{negative} + 2. \quad 4\text{-}1$$

where $S_{positive}$ = positive polarity waveform sample in units of volts, and

$S_{negative}$ = negative polarity waveform sample in units of volts.

Baseline corrections were performed to align the baseline of pulses to zero level. This correction was needed to accurately determine the pulse amplitude. The mean of the first five samples was subtracted from each pulse sample for baseline corrections. Figure 4.3 shows an example of raw pulse and processed pulse from the digitizer.

Pulse cleaning was implemented in the C++ program. The pulses were cleaned for electronic noise, clipping, and pile-up. A threshold of 30 mV was used to eliminate noisy waveforms and an upper threshold of 1.9 V was used to eliminate clipped waveforms. Piled-up events were identified as those having a second voltage pulse with a leading edge that increased by at least 12% of the amplitude of the first voltage pulse in one digitizer step. For every pulse eliminated by the pulse cleaning algorithm, its corresponding detection event in the other detector was also eliminated. The entire pulse processing algorithm is described in Figure 4.4.

The difference between the stop and start detection times were calculated and binned to a histogram. The TOF distribution is shown in Figure 4.5. A peak is observed at 3 ns, which corresponds to gamma-rays traveling a flight path of 1 m. The wide distribution observed between 10 ns and 110 ns corresponds to neutrons emitted from the ^{252}Cf source. The prompt fission neutrons are emitted with a Watt energy spectrum [34] and the time neutrons take to travel a flight

path of 1 m is dependent on the energy of the emitted neutron. The relation between the neutron kinetic energy and travel time is,

$$KE = \frac{1}{2} m_v \left(\frac{d}{\Delta t}\right)^2 . \qquad 4\text{-}2$$

where KE = kinetic energy of the emitted neutron,

m_v = mass of neutron,

d = flight path i.e., 1m, and

Δt = difference between the stop and start detection times.

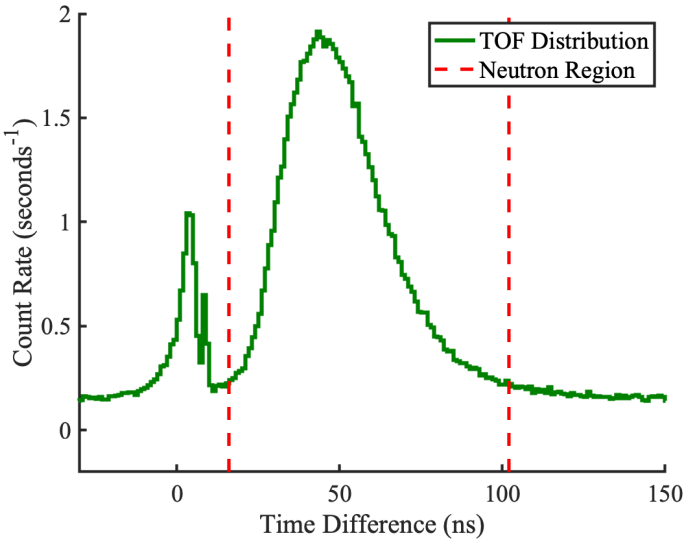

Figure 4.5. Histogram of the time differences between the start and stop detection times.

A neutron region was defined in the TOF distribution. All detection events in the stop detector that arrived within 16 ns and 102 ns of the start detector were selected for further processing. Using eq. 4-2, the selected region corresponds to neutron energies between 0.5 MeV to 20.4 MeV. The 0.5 MeV neutron energy is equivalent to 0.05 MeVee light output (eq. 2-3), which was the threshold used for pulse shape discrimination to remove gamma-ray contamination in the neutron

region. The 20.4 MeV neutron energy was sufficiently high to capture energetic prompt fission neutrons from the ^{252}Cf source.

4.2.2 High-Confidence Neutron and Photon Pulses

Figure 4.6 shows the tail and total integrals of all pulses that lie in the selected neutron region. A gamma contamination was present in this region. The contamination was due to accidental coincident radiation events i.e., chance coincident events that were detected in the stop detector. The gamma contamination was eliminated by performing pulse discrimination (PSD) analysis using the traditional charge integration (CI) method described in section 2.2.3. The particle discrimination line for CI method was determined using an auto-slice PSD algorithm described by Polack and colleagues [47].

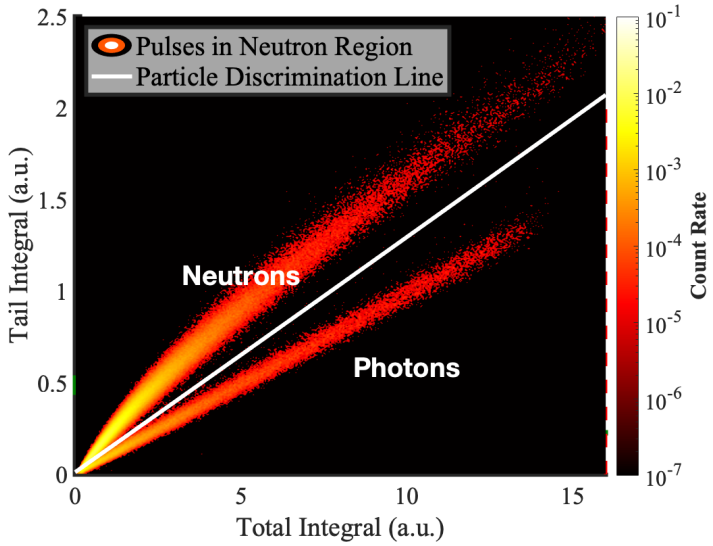

Figure 4.6. Tail and total integrals of all pulses that lie in the neutron region of the time-of-flight distribution.

The time-tags from the TOF analysis and scintillation events classified as neutrons by the traditional CI method provided high-confidence neutron pulses for training of the ANN system. The remaining scintillation events from the TOF analysis were labeled high-confidence photon pulses. To further improve the voltage pulse signal-to-noise ratio, a 200 mV threshold was applied

to high-confidence neutron and photon pulses. Additionally, a 1.9 V upper threshold was applied to remove any clipped pulses. The 200 mV threshold corresponded to 0.28 MeVee light output and 1.9 V corresponded to 2.67 MeVee light output. The extracted training data therefore had neutron and photon pulses of varying light output values ranging from 0.28 MeVee to 2.67 MeVee. Figure 4.7 shows the light output distributions for the training data.

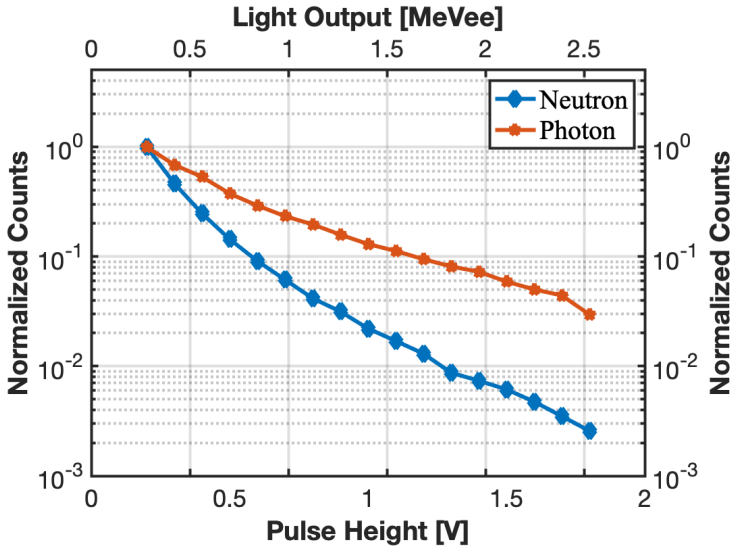

Figure 4.7. Light output distribution for high-confidence neutron and gamma pulses extracted from the time-of-flight measurement.

4.3 Synthesis of Piled-Up Events

The high-confidence neutron and photon pulses were used to synthesize piled-up events. The synthesis of piled-up events provided ground truth training data for the ANN system. Four categories of events were defined based on the time separation between pulses and the number of pulses present in the piled-up event. These categories were labeled close type, split type, cut type, and triple/quadruple type piled-up events. The close, split, and cut type piled-up events contain two pulses whose amplitudes are separated in time, whereas the triple and quadruple type piled-up events contain three and four pulses respectively. The developed ANN system only recovers

particle information from the close, split, and cut type piled-up events. The occurrence of triple and quadruple type piled-up events is rare, and therefore these types of pulses are eliminated.

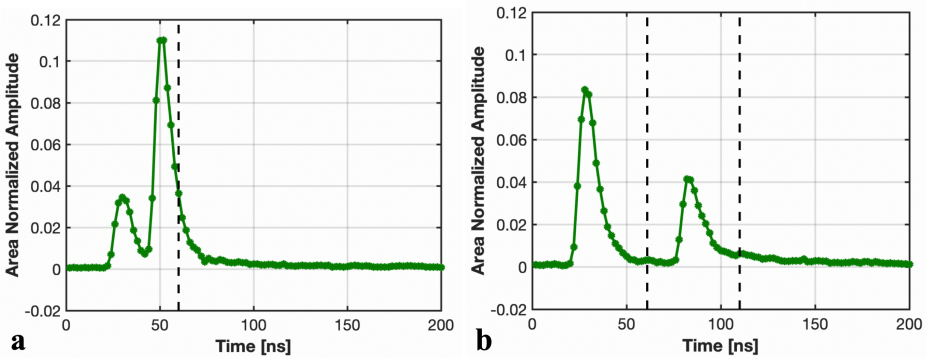

Figure 4.8. A close type piled-up event in which: a) the second voltage pulse is within 60 ns (too-close type), and b) the second voltage pulse is between 60-110 ns.

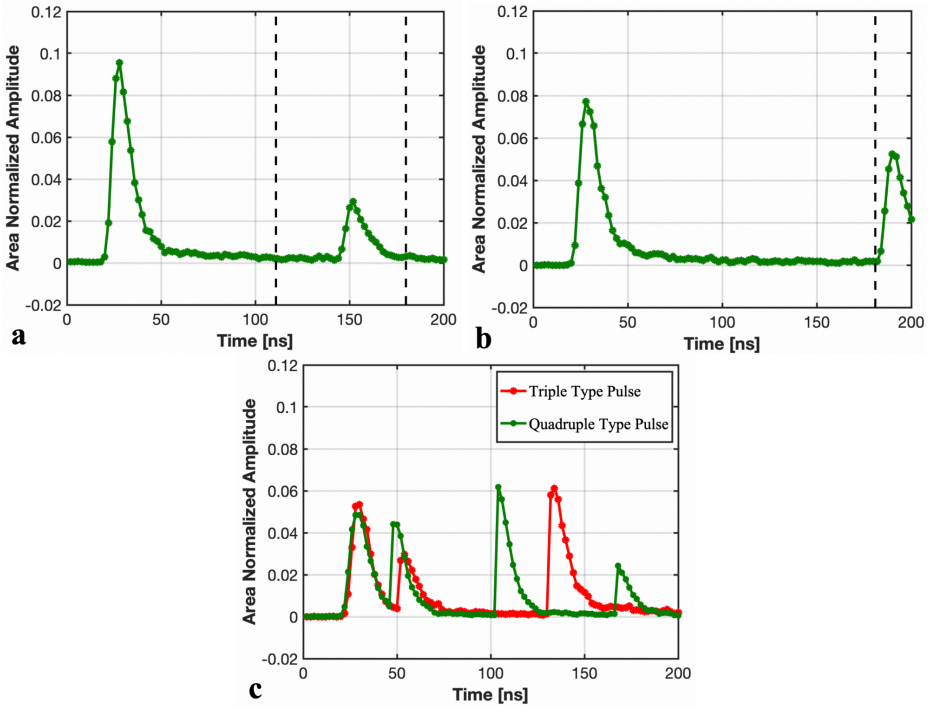

Figure 4.9. a) Split type piled-up event (second voltage peak is between 111-180 ns), b) cut type piled-up event (second voltage peak is past 181 ns), and c) triple/quadruple type pulses.

A close type piled-up is defined as one in which the amplitude of the second voltage pulse lies between 60 ns and 110 ns of the acquisition window. Piled-up events in which the second amplitude of the voltage pulse lies within 60 ns of the acquisition window were defined as too-

close type piled-up events. No information is recovered from too-close type events as the scintillation pulses cannot be time-resolved. In the split type piled-up events, the amplitude of the second voltage pulse lies between 111 ns and 180 ns. The piled-up events in which the amplitude of the second voltage pulse lies past 181 ns of the acquisition window were defined as cut-type events. In the cut-type piled-up events, only the first scintillation pulse is recovered. No information is recovered from the second pulse due to missing information in the tail of the voltage signal. Figure 4.8 and Figure 4.9 show an example of each category of piled-up event.

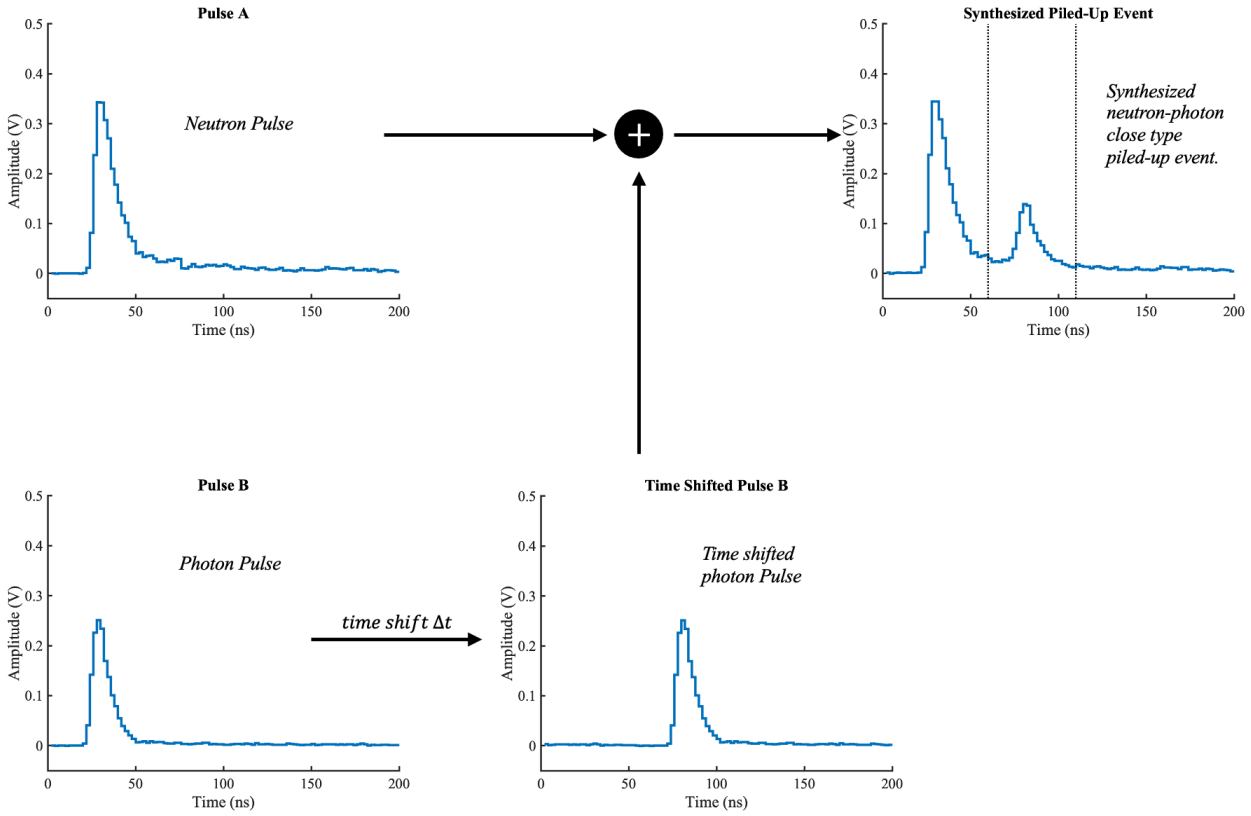

Figure 4.10. Graphical representation of steps involved in the synthesis of piled-up events.

The piled-up events were created by randomly selecting a pulse from high-confidence neutron dataset and photon dataset. These randomly selected pulses are referred to as pulse A and pulse B. The pulse B was then randomly shifted in time. The random time shifting was based on the type of piled-up event being synthesized i.e., close, split, or cut. In the final step, pulse A and

the time shifted pulse B were added together to create a piled-up event. This method allowed us to easily obtain a set of piled-up events with known type of first and second pulse, to precisely control the time interval between the two pulses, and to selectively train the ANN system. Figure 4.10 graphically illustrates steps involved in the synthesis of piled-up events.

4.4 Summary and Remarks

The success of machine learning algorithms depends on the quality of training dataset. In this chapter, I presented a framework to extract high-confidence neutron and photon pulses using TOF and CI method. Additionally, I illustrated the process of creating ground truth piled-up events that can be used to by the ANN system to learn about pulse pile-up recovery. The acquired high-quality training data was used to train the developed ANN system. The next chapter describes the architecture of the developed ANN system and its performance in intense radiation environments.

Chapter 5 Neural-Network-Based Digital Pulse Processing

To mitigate the effect of pulse pile-up during measurement of photoneutrons, an artificial neural network (ANN) system was developed and demonstrated. This chapter provides details on the architecture, high-confidence training data, and the training process of the ANN system. Additionally, the performance of the ANN system was demonstrated in intense radiation environment, such as the bremsstrahlung radiation from the linac. The results presented in this chapter were published in the IEEE Access journal in 2021 (doi.org/10.1109/ACCESS.2021.3108406).

5.1 Developed Artificial Neural Network System

5.1.1 Architecture of the System

The developed ANN system consists of six neural networks (NNs) that work in conjunction to produce the desired classification of voltage pulses. The ANN system represented in Figure 5.1 is a unique system in which small well-defined NNs are used to perform detailed classifications. Using multiple NNs allows the flexibility to add classification results in the future without significantly affecting the existing results. Additionally, the ANN system allows for easy interpretation of classification results as well as for updates and future improvements. The ANN system, in combination with two cleansers, presents a novel approach for classifying single and piled-up pulses from a *trans*-stilbene organic scintillator.

Data is pre-processed before it is sent to the ANN system. Pre-processing includes converting ADC units to volts (eq. 2-4), flipping the voltage pulse from negative to positive polarity, and performing baseline corrections. The rising edge of each voltage pulse is aligned at 24 ns (12th digitizer sample) using digital constant fraction discrimination (CFD).

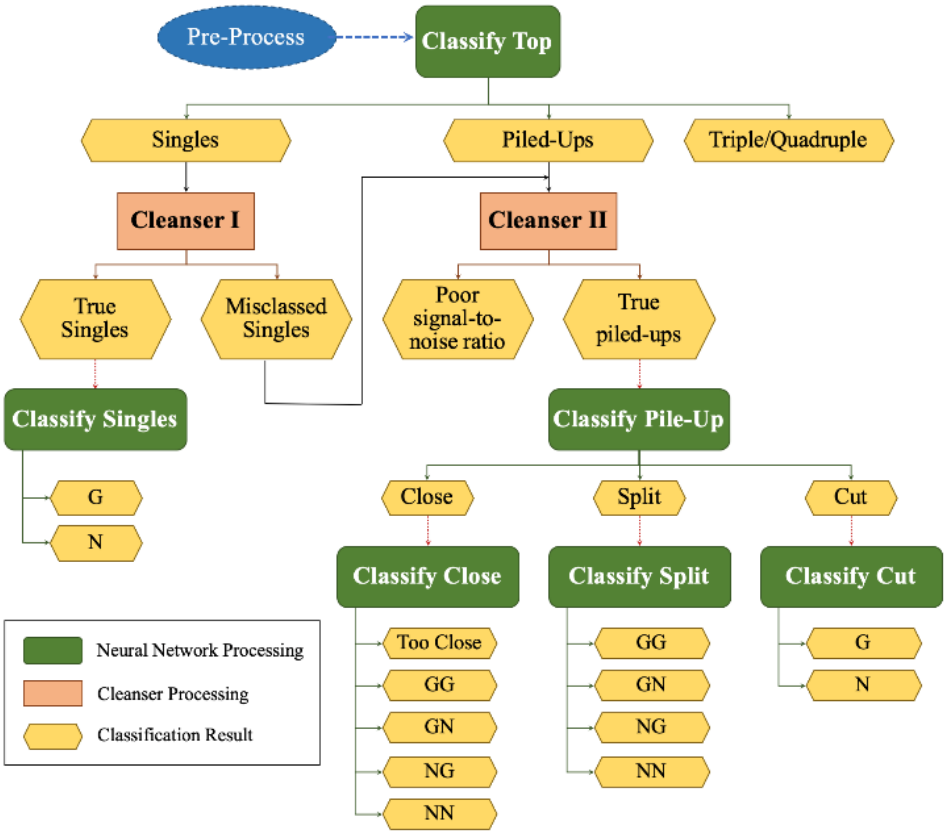

Figure 5.1. Architecture of the ANN system for digital processing of scintillation pulses [48].

After pre-processing the data, Classify Top NN categorizes single, piled-up (double pulses), and triple/quadruple type pulses. The triple/quadruple type pulses are neither recovered nor processed for further classification. Following the singles branch in Figure 5.1, Cleanser I provides an independent verification of the single pulse classification from Classify Top. The independent verification is important because the intense photon flux during interrogation may introduce additional noise in the voltage pulse that may result in misclassification from Classify Top. If Cleanser I flags pulses as misclass, they are reclassified as piled-up events. If not flagged, these

noisy pulses may likely be classified as neutrons by Classify Singles NN because of increased area in the tail. The "true" remaining single pulses are determined to either be a gamma or neutron pulse, represented in Figure 5.1 with a "G" for gamma/photon and an "N" for neutron, in Classify Singles.

Now considering the piled-ups branch of Figure 5.1, Cleanser II processes the piled-up events categorized by Classify Top (and Cleanser I). Cleanser II separates out poor signal-to-noise ratio (SNR) pulses from "true" piled-up events. The "true" piled-up events are then fed into Classify Pile-Up NN to be classified into three groups (close, split, and cut type piled-up events as defined in section 4.3). For each piled-up category, there is a corresponding NN processing that recovers neutron and photon information.

The hidden layers in all NNs were aimed to have the smallest dimension to reduce computational complexity while maintaining the performance of the network. The reduced complexity is particularly important for real-time data processing using field programable gate arrays (FPGA). For each NN, we started with an arbitrarily large dimension of the hidden layer. The dimension was gradually reduced, and for each dimension of the hidden layer the NN classification accuracy and error were determined. The percent accuracy and error were obtained from confusion matrices that were generated for each NN from a pre-labelled test dataset. The chosen dimension of the hidden layer is the one at which the percent accuracy is highest, and the percent error is the least, except in some cases where the computational complexity cost outweighs the marginal increase in accuracy. Table 5.1 summarizes the structure of NNs used in the ANN system. Following is a more detailed discussion on each NN.

Table 5.1: Structure of neural networks in the ANN system.

NN Processing	Dimension of input layer	Dimension of output layer	Activation function at output layer	Number of hidden layers	Activation function at hidden layers	Dimension of hidden layers
Classify Top*	110	3	Softmax	1	Log sigmoid**	30
Classify Singles*	110	2	Softmax	1	Log sigmoid**	30
Classify Pile-Up*	110	3	Softmax	1	Tansig	3
Classify Close*	120	5	Softmax	2	#1: Log sigmoid** #2: Tansig	#1: 30 #2: 10
Classify Split	120	4	Softmax	1	Tansig	7
Classify Cut	120	2	Softmax	1	Tansig	1

* Stacked neural network
** Encoder layer

5.1.2 Structure of Neural Networks

Classify Top is a stacked NN [49] in which an encoder layer is connected to a softmax output layer. A log sigmoid activation function was used for the encoder layer. The dimension of the encoder layer is 30 and the softmax output layer has a dimension of 3. The input vector to the NN consist of 100 Euclidean-normalized samples,

$$norm_{(Euclidean)_i} = \frac{S_{(Volts)_i}}{\sqrt{\sum_{j=1}^{n} S^2_{(Volts)_j}}}, \qquad 5\text{-}1$$

where $norm_{(Euclidean)_i}$ = Euclidean normalized value at i[th] sample,

$S_{(Volts)_i}$ = i[th] sample in units of volts, and

n = total number of digitizer sample per voltage pulse.

and 10 segmented maximum values. The segmented maximum is found by dividing the Euclidean-normalized voltage pulse, which consists of 100 normalized samples, into 10 segments of 10

samples each. For each segment of 10 samples, the maximum value in the segment is called the segmented maximum.

Classify Singles is also a stacked NN in which the encoder layer has a dimension of 30 and the softmax output layer's dimension is 2. Classify Singles NN takes in 100 cumulative distribution function samples,

$$CDF_i = \sum_{j=1}^{n} norm_{(Area)_j}, \quad 5\text{-}2$$

where CDF_i = Cumulative distribution function at i^{th} sample, and

$norm_{(Area)_j}$ = area normalized value at i^{th} sample, which is given by eq. 5-3.

$$norm_{(Area)_i} = \frac{S_{(Volts)_i}}{\sum_{j=1}^{n} S_{(Volts)_j}}, \quad 5\text{-}3$$

and 10 segmented maximum values as inputs. Unlike Classify Top NN that uses Euclidean-normalized samples for segmented maximums, Classify Singles NN uses 100 area normalized samples (eq. 5-3).

Classify Close NN is a differently stacked NN in which an encoder layer is connected to a hidden layer that is then connected to a softmax output layer. The activation function used for the hidden layer was a hyperbolic tangent sigmoid function (tansig). A log sigmoid activation function was used for the encoder layer that has a dimension of 30. The dimension of tansig hidden layer is 10 and the dimension of softmax output layer is 5. The input vector to the NN consists of 100 Euclidean-normalized samples, 10 segmented maximum values, and 10 segmented area values. Segmented area is the area of each segment of the Euclidean-normalized voltage pulse.

Classify Pile-Up, Classify Split and Classify Cut NNs have a tansig hidden layer connected to a softmax output layer. All three NNs take in 100 Euclidean-normalized samples and 10 segmented maximum values as inputs. In Classify Split and Classify Cut NNs, 10 segmented area values are also included in the input vector. The dimension of the tansig hidden layer is 3 for Classify Pile-Up NN, 7 for Classify Split NN and 1 for Classify Cut NN. The dimension of softmax output layer is 3 for Classify Pile-Up NN, 4 for Classify Split NN and 2 for Classify Cut NN.

Cleanser I is an autoencoder based cleanser that helps flag pulses with extra noise. The autoencoder consists of two fully connected layers; one is an encoder layer and the other is a decoder layer. Figure 5.2 provides visualization of the steps performed in Cleanser I. An autoencoder, which was trained on clean single pulses, is used as a denoiser to the original Euclidean-normalized pulse. The decoder from the autoencoder reconstructs the original Euclidean-normalized pulse. There is no noise/ripple present in the reconstructed pulse. The ratio of the absolute difference between reconstructed and original pulses to the reconstructed pulse is computed using,

$$ratio = \frac{|\, reconstructed - original \,|}{reconstructed}, \qquad 5\text{-}4$$

where $reconstructed$ = decoded pulse, and

$original$ = Euclidean-normalized pulse.

If the ratio exceeds a set threshold value, the pulse is flagged as a misclassified single pulse. Both the encoder and decoder use a log sigmoid activation function. The encoder layer has a dimension of 30 and the decoder layer's dimension is 100. Cleanser I provides an independent verification to the singles classification produced by the Classify Top NN, thereby increasing confidence in the neutron and photon classification of a single pulse.

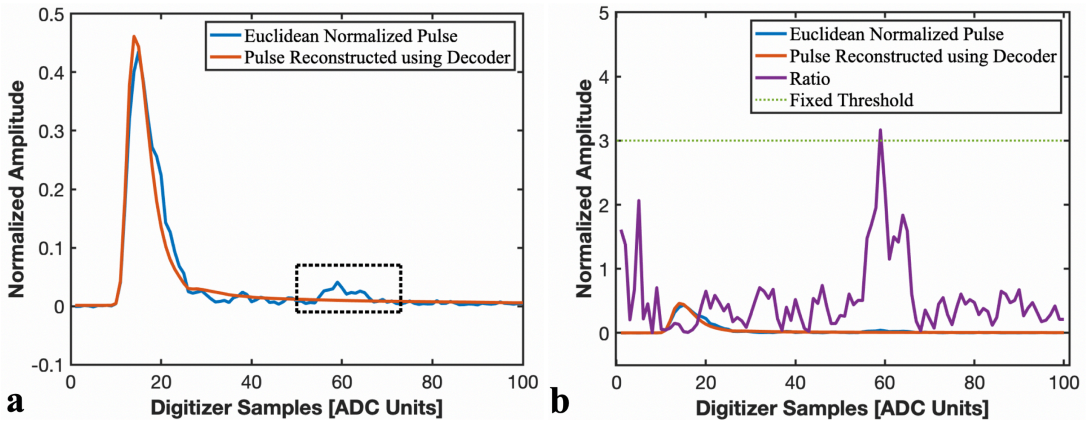

Figure 5.2. a) An example of a noisy pulse decoded using the trained autoencoder, and b) Ratio computed on the noisy pulse [48].

Cleanser II differentiates poor SNR pulses from "true" piled-up events. The second voltage pulse in the piled-up event must exceed a set threshold for it to be considered as a "true" piled-up event. The threshold is user-specified and all piled-up events that pass the voltage threshold check on the second pulse are sent to the Classify Pile-Up NN for further classification.

5.2 Training of the ANN system

5.2.1 Training Parameters

The ANN system was trained using the Deep Learning Toolbox from MATLAB [50]. All NNs are fully connected feedforward neural networks that were trained using the scaled conjugate gradient learning algorithm [51]. A cross-entropy loss function was implemented to calculate the loss during training of NNs. The maximum number of epochs to train was set to 25,000. The training was terminated when a loss of 1E-3 was achieved on the training dataset. Additionally, if the non-training validation subset loss increased for a consecutive 100 epochs, the network stopped training; we call this epoch *n*. At this point, the network disregards the latest 100 epochs and chooses the weights from epoch *n-100*.

All six NNs were trained individually in a supervised fashion. The three stacked NNs, Classify Top, Classify Singles and Classify Close were trained in three steps. First step included training of hidden layers in an unsupervised fashion using the autoencoder; followed by the training of the softmax output layer. In the final step, all layers were joined together to form a stacked NN, which was trained for one final time in a supervised fashion.

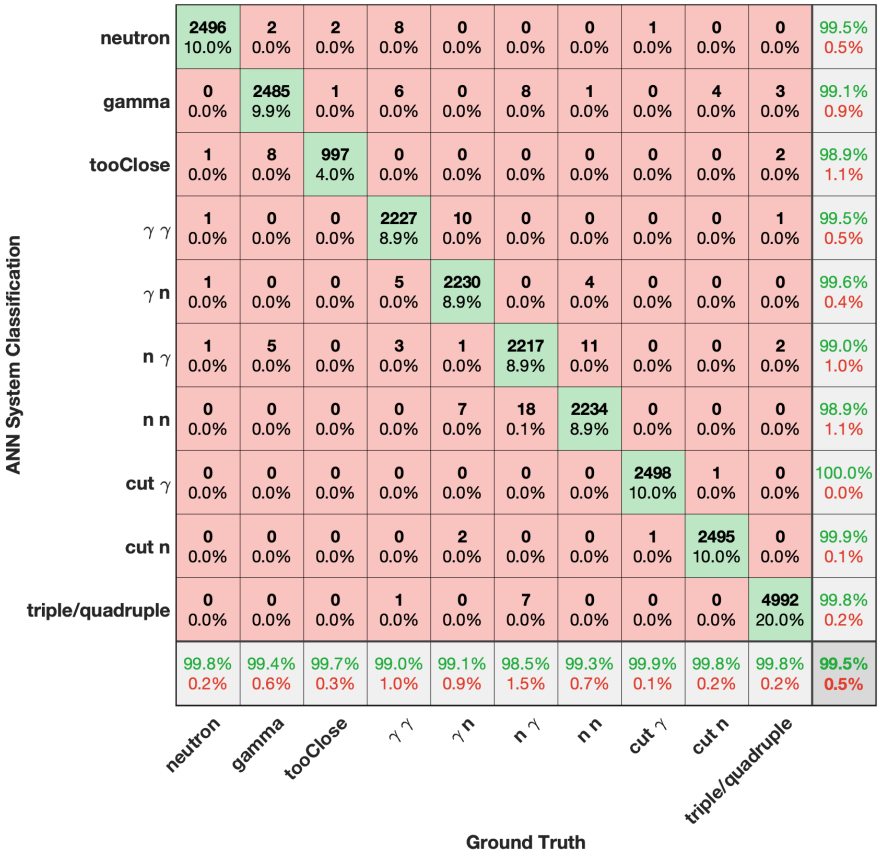

Figure 5.3. Confusion matrix after training of the ANN system [48].

A small set of the data (5,000 pulses for each single, close, split, cut and triple/quadruple category) was used to test the performance of the trained ANN system. The confusion matrix generated from the test dataset is given below in Figure 5.3. The classification of single pulses produced by the ANN system is 99.60% accurate. The neutron-photon combinations from close and split type piled-up events are identified with an average accuracy of 98.98%. In cut type piled-

up events, the classification of the primary voltage pulse is 99.85% accurate. An overall classification accuracy of 99.50% is obtained for the developed ANN system.

5.3 Testing the ANN System Across Different Gain Settings

The ANN system was tested on TOF data collected at a variety of PMT gain settings. The PMT gain was calibrated using a ^{137}Cs gamma source (Figure 5.4). A ^{252}Cf spontaneous fission source was used in the TOF measurement. Neutron and photon pulses were extracted using the steps described in section 4.2. The TOF+CI extracted neutrons and photons i.e., Figure 5.5a and Figure 5.5b were fed into the ANN system to test its performance at a variety of PMT gain settings.

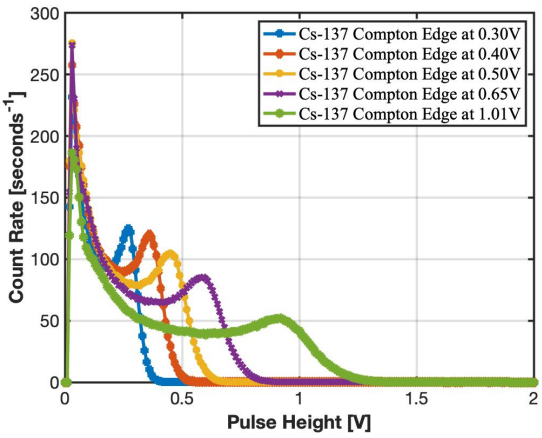

Figure 5.4. PMT gain calibration for the TOF measurement using a ^{137}Cs source.

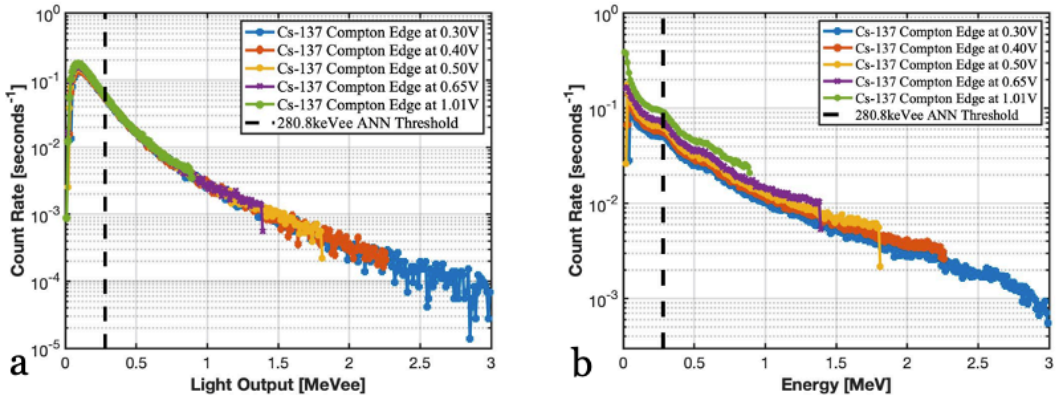

Figure 5.5. Light output distributions for a) TOF+CI extracted neutrons and b) TOF+CI extracted photons.

Figure 5.6a and Figure 5.6b shows the ANN classifications when TOF+CI labeled neutrons and photons were provided as inputs. Across a variety of PMT gain settings, the ANN classifications were within 1.2% of the TOF+CI labeled pulses. The pulse cleaning technique used to eliminate piled-up events in the traditional CI method misclassified certain poor signal-to-noise ratio pulses as good electrical signals. The developed ANN system successfully identified these kinds of poor SNR ratio pulses. Examples of ANN identifying poor SNR pulses are shown in Figure 5.7.

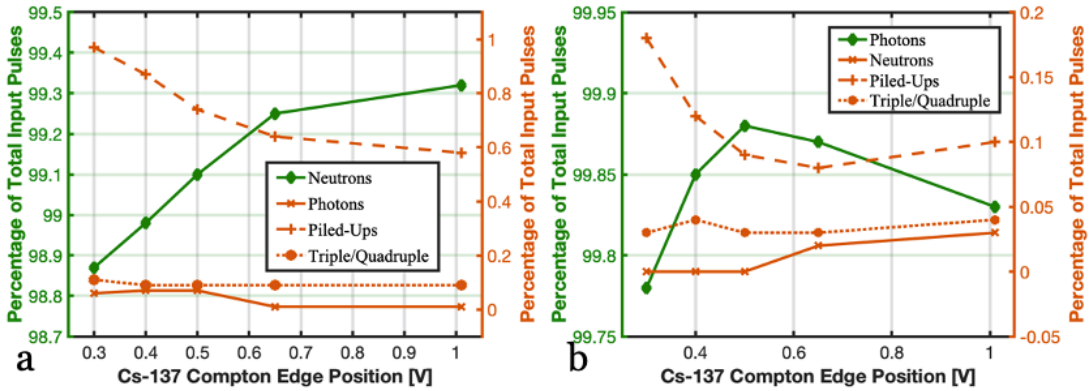

Figure 5.6. ANN classifications when: a) TOF+CI extracted neutrons are provided as inputs and b) TOF+CI extracted photons are provided as inputs.

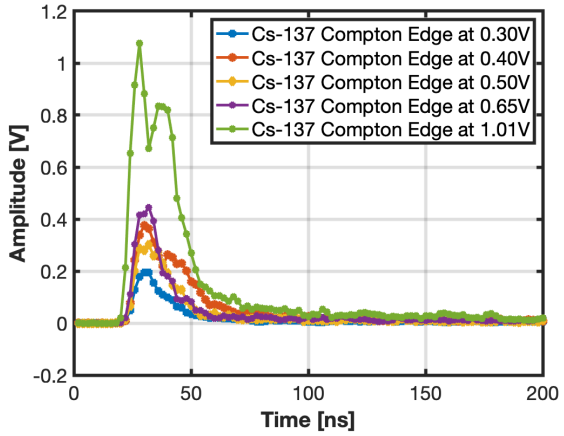

Figure 5.7. Examples of poor SNR pulses identified by the developed ANN system.

In this test, the ANN system demonstrated its robustness against a wide range of energy deposited by the incoming particle (different energy regions of the spectrum). With an ANN

system that is invariant to the gain of the measuring circuit and sensitive to a wide range of deposited energy, the application space of the network is broadened.

5.4 Demonstration of the ANN System

5.4.1 Experimental Setup

A ^{252}Cf neutron source was measured in the presence of the intense bremsstrahlung flux from the linac. The source was placed 4 m off-axis from the beam center line; 4 m prevents any radioactivity being induced in the source because of bremsstrahlung bombardment. This measurement of the ^{252}Cf in the presence of the bremsstrahlung flux is referred to as the active ^{252}Cf measurement. Ground truth neutron count rates were established through a passive ^{252}Cf measurement i.e., measuring the neutron source without the bremsstrahlung flux from the linac.

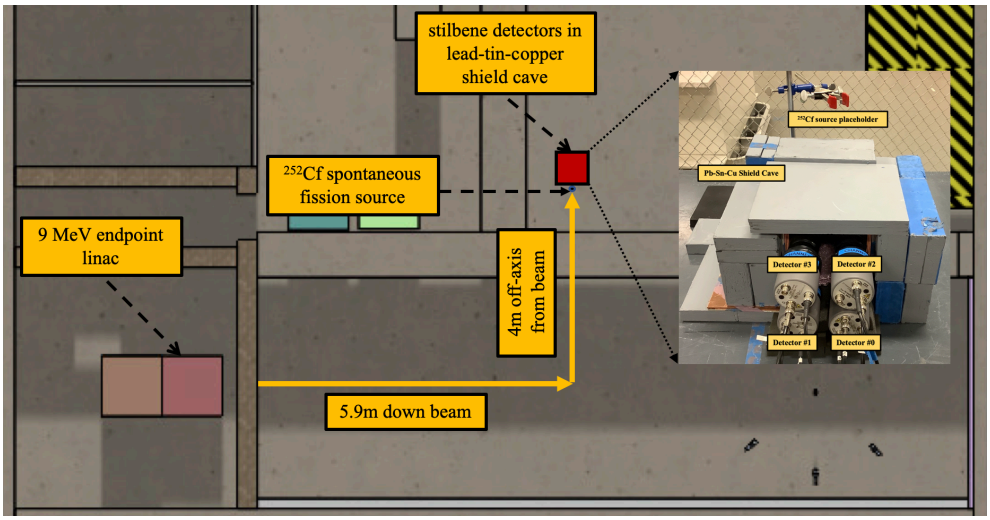

Figure 5.8. Experimental setup for the active ^{252}Cf measurement [48].

Fission neutrons were detected using four *trans*-stilbene scintillators coupled to PMTs. The detectors were placed in a layered lead-tin-copper shield cave, which helps reduce the effect of pulse pile-up (pile-up is a function of the radiation flux and voltage pulse width). The tin and copper in the shield cave helped shield low energy characteristic Kα and Kβ X-rays that are

emitted from lead because of high energy photon absorption [52]. Data was acquired with a CAEN V1730 digitizer. Figure 5.8 shows the detector setup during the active ^{252}Cf measurement.

An active background measurement was also performed to account for photoneutrons produced in the surrounding high-Z materials. All active measurements i.e., background and ^{252}Cf were performed for 4 hours, and the passive ^{252}Cf measurement was performed for 30 minutes.

5.4.2 Data Analysis

The linac at the University of Michigan is currently operating in pulsed mode with a pulse length of 4 μs and a repetition rate of approximately 44 Hz. Time gating was performed to separate during and in-between linac pulses stilbene detections. The scintillation pulses detected during linac pulses were processed with the traditional CI method and the developed ANN system. All data were processed with a lower light output threshold of 0.28 MeVee and an upper light output threshold of 2.67 MeVee.

For the traditional CI analysis, particles were discriminated by a line that was obtained using an auto-slice PSD algorithm [47] on the passive ^{252}Cf data. A fractional pile-up cleaning approach was used to eliminate piled-up events from active measurements. Piled-up events were identified as those having a second voltage pulse with a leading edge that increased by at least 12% of the height of the first voltage pulse in one digitizer step. The CI analysis provides a basis for which the performance of the developed ANN system can be compared to that of traditional methods.

5.4.3 Results and Discussion

Figure 5.9 shows the active background subtracted neutron count rates in all four *trans*-stilbene detectors determined using the traditional CI method. Without any pile-up cleaning, net

neutron count rates for active ^{252}Cf measurements exceeded ground truth by an average of 38% in detectors 0, 1, and 2 (Figure 5.9a). The overestimation is because of misclassification of piled-up events as neutrons.

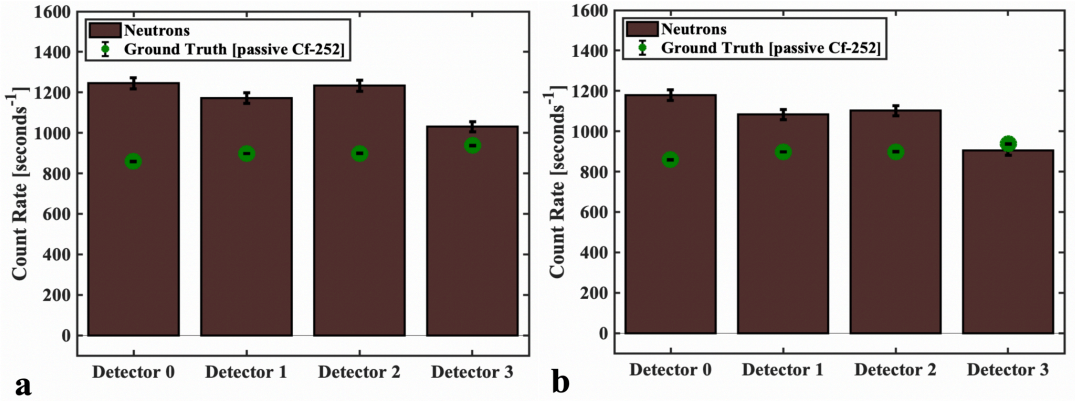

Figure 5.9. Active background subtracted neutron count rates in all four detectors determined using the traditional CI method: a) without pile-up cleaning, and b) with pile-up cleaning. (*Error bars are from Poisson counting statistics and are represented within one standard deviation.*) [48]

The PSD plots represented in Figure 5.10a and Figure 5.10c show that particle discrimination capabilities of the scintillator are greatly deteriorated due to the presence of piled-up events. After pile-up cleaning, there still existed many piled-up events that were misclassified as neutrons (Figure 5.10 b and c) resulting in a 27% overestimation of net neutron rates in detectors 0, 1 and 2 (Figure 5.9b). A lower fractional cleaning percentage can be used to eliminate remaining piled-up events; however, that will result in over-cleaning of the active dataset. Figure 5.11 shows the PSD contour plot for the ANN attributed single neutron pulses in channel 0. For reference, a passive ^{252}Cf PSD and a particle discrimination line are also included. The ANN attributed neutrons from active measurements constitute a neutron region in the exact same location as one would expect from a passive measurement. The PSD contour verifies the ANN system classification of single neutrons.

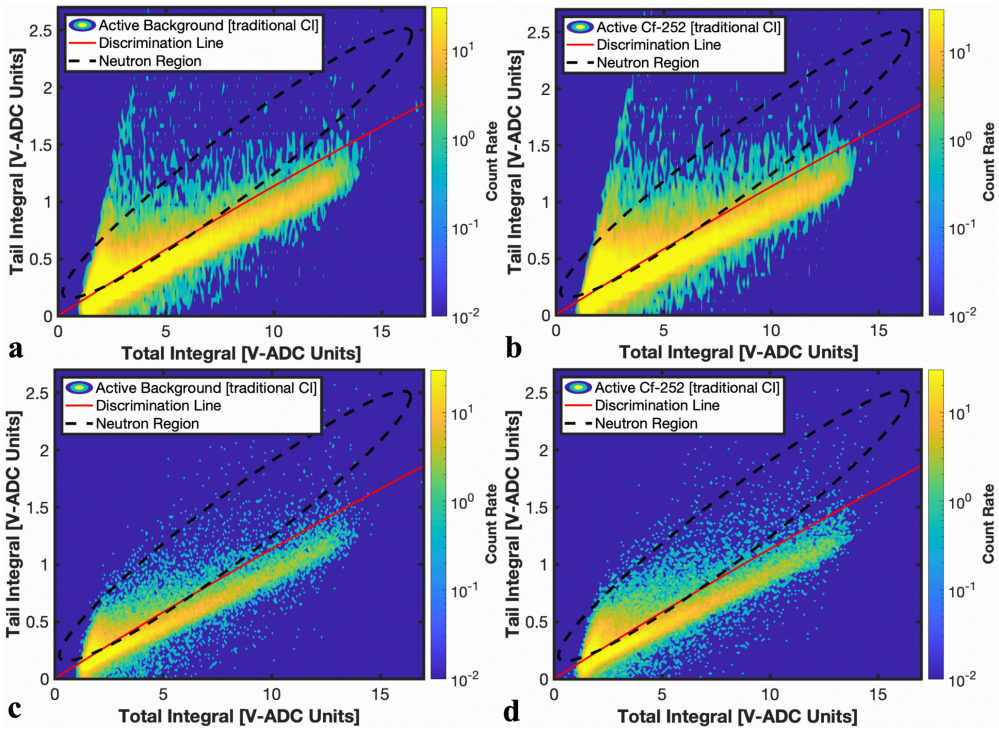

Figure 5.10. Traditional CI PSD plots: a) active background (before pile-up cleaning), b) gross active ^{252}Cf (before pile-up cleaning), c) active background (after pile-up cleaning), and d) gross active ^{252}Cf (after pile-up cleaning). *Note that the neutron region represented in these plots is for illustration purposes only*. [48]

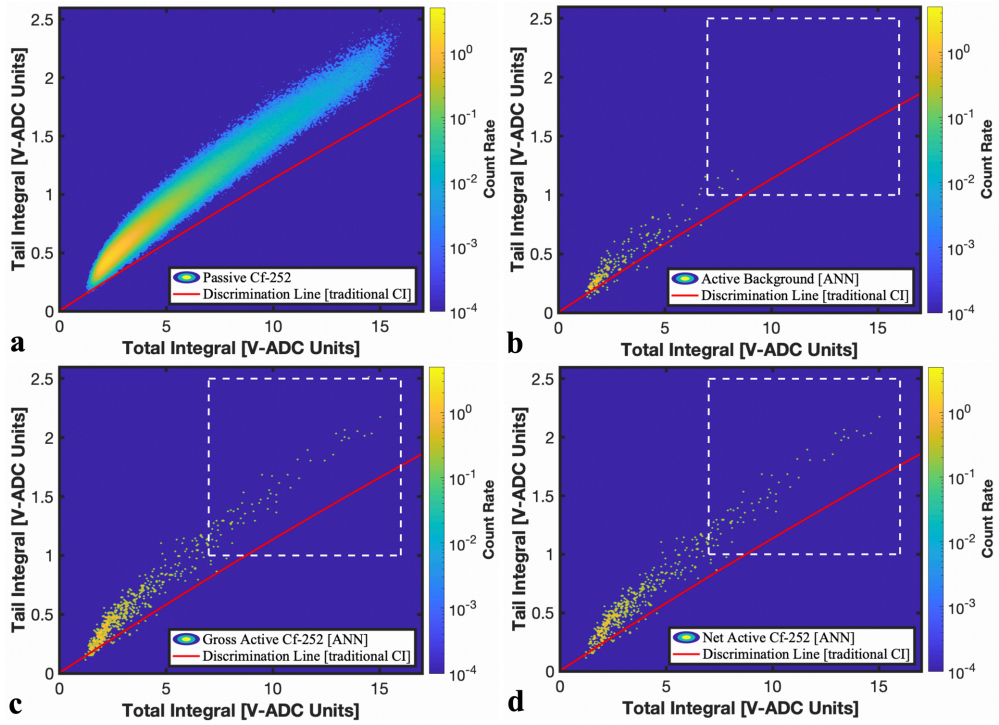

Figure 5.11. PSD plots for ANN attributed single neutrons: a) passive ^{252}Cf, b) active background, c) gross active ^{252}Cf, and d) net active ^{252}Cf [48].

Figure 5.12 shows the breakdown of pulses during active background and active ^{252}Cf measurements in detector 0. A significant portion (29%) of the total detected pulses belong to the unclassifiable category. This unclassifiable category of pulses includes the too-close type of piled-up events, triple/quadruple type, and poor SNR pulses. Nearly 29% of the total piled-up events (total piled-up events include both classifiable and unclassifiable pulses) were recovered by the ANN system. The other three detectors used during active measurements exhibited similar breakdown of pulses.

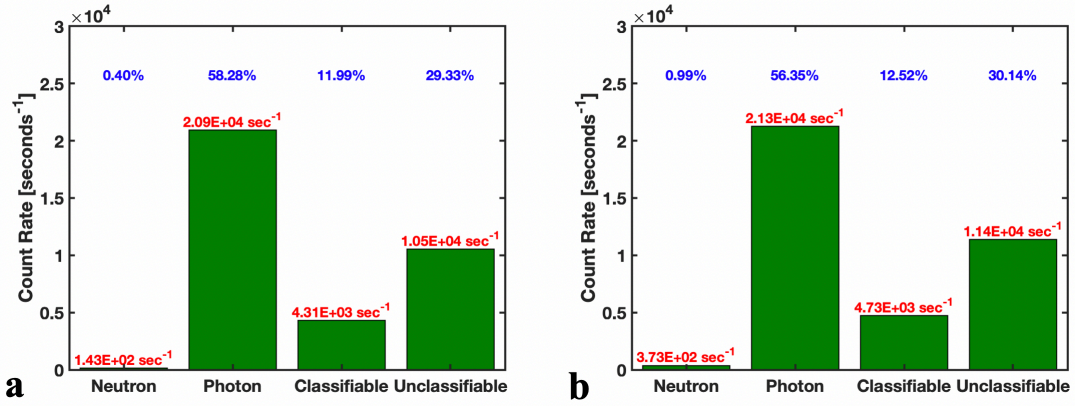

Figure 5.12. Breakdown of scintillation pulses in channel 0 by the ANN system: a) active background and b) active ^{252}Cf [48].

Figure 5.13 summarizes overall net neutron count rates as determined by the developed ANN system. Using only single neutron pulses, the net active ^{252}Cf count rates account for an average of 32.55% of the ground truth in all four detectors. After information was recovered from piled-up events, the overall net count rate increased to 62.32% of the ground truth. There still exist gaps between the ground truth and the measured net active neutrons, which is due to information lost to the unclassifiable piled-up events.

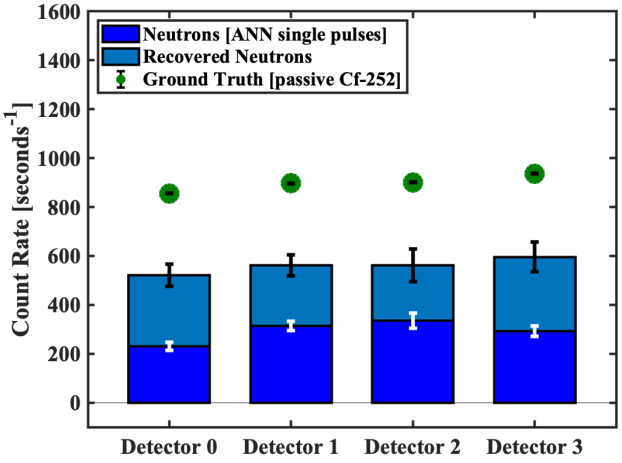

Figure 5.13. Active background subtracted neutron count rate in all four detectors determined using the ANN system (*Error bars are from Poisson counting statistics and are represented within one standard deviation.*) [48]

5.5 Summary and Remarks

The pulse pile-up is inevitable in intense radiation environments. The particle discrimination capabilities of the *trans*-stilbene scintillator are greatly deteriorated due to the presence of piled-up events. These piled-up events are often misclassified as neutrons. To mitigate the effect of pulse pile-up, I developed an ANN system to classify scintillation pulses as neutrons and photons and recover particle information from piled-up events. The architecture of the ANN system is robust and can be trained to classify scintillation pulses from any scintillator detector coupled to either PMT or silicon photomultiplier tube (SiPM), thereby expanding the use of the ANN system.

An overall classification accuracy of 99.5% was achieved during the training of the ANN system. The different normalization methods applied to voltage pulses make the ANN system invariant to the gain setting of the measuring circuit. This gain invariance helps classify scintillation pulses in different regions of the energy spectrum.

The overall performance of the ANN system was demonstrated through the active ^{252}Cf measurement in which the neutron source was measured in the presence of the bremsstrahlung

radiation from the linac. The ANN system was found to outperform traditional methods in the intense photon environment. The traditional CI method over-predicted the ground truth neutron rate by 27%. This over-prediction was due to misclassification of piled-up events as neutrons. The ANN system correctly identified single and piled-up events. Nearly 29% of piled-up events were recovered, and the neutron count rate after pile-up recovery was 62% of the ground truth. This pile-up recovery provides an efficiency boost for neutron detection.

Chapter 6 Interrogation of Bare Depleted Uranium

For the measurement of photoneutrons, a 5.23 cm thick depleted uranium (DU) target was interrogated with bremsstrahlung photons from a 9-MV linac, and fast neutrons were detected with four *trans*-stilbene organic scintillators. This chapter provides details on the experimental setup, data analysis, and measured results for the photoneutron count rate from uranium. For simulations with Monte Carlo codes, a framework was developed using the MCNPX-PoliMi transport code. The developed framework is described, and the simulated results are compared with the measured results. The chapter concludes with a discussion on the discrepancy observed between simulation and measurement. The results presented in this chapter were accepted for publication in the Physical Review Applied journal [53].

6.1 Photoneutron Detection with *Trans*-Stilbene Scintillators

6.1.1 Experimental Setup

The University of Michigan has a 9-MV electron linac that is currently operating in pulsed mode with a pulse length of approximately 4 μs and a repetition rate of approximately 44 Hz. The bremsstrahlung radiation is collimated using a primary and secondary collimator. The primary collimator consists of lead backed with tungsten and has a beam spot size of 25 cm. The lead is 83 cm in diameter and 28 cm thick, whereas tungsten is 48 cm in diameter and 11 cm thick. The secondary collimator consists of lead, which is 74 cm square and 41 cm thick. The beam spot size is reduced from 25 cm to 5.08 cm at the exit of the secondary collimator.

A depleted uranium (DU), which is 99.7 wt% ^{238}U and 0.3 wt% ^{235}U, and lead targets were interrogated for an hour with the bremsstrahlung photons. The DU target was a 5.23 cm cube, and the lead target had a dimension of 5.08 cm x 5.08 cm x 6.35 cm. Targets were placed in the beam 27 cm from the secondary collimator. At this location, the beam spot size is large enough to cover the entire surface area of the target, which is desired to maximize photoneutron production. The lead target produces neutrons through (γ, n) reactions whereas the DU target produces neutrons through (γ, n) and (γ, f) reactions [7]. Lead interrogation provides a basis for which photoneutrons from an actinide, such as DU, can be compared to photoneutrons from a non-SNM target, such as lead. An active background measurement was also performed for an hour to account for photoneutrons produced in the collimator.

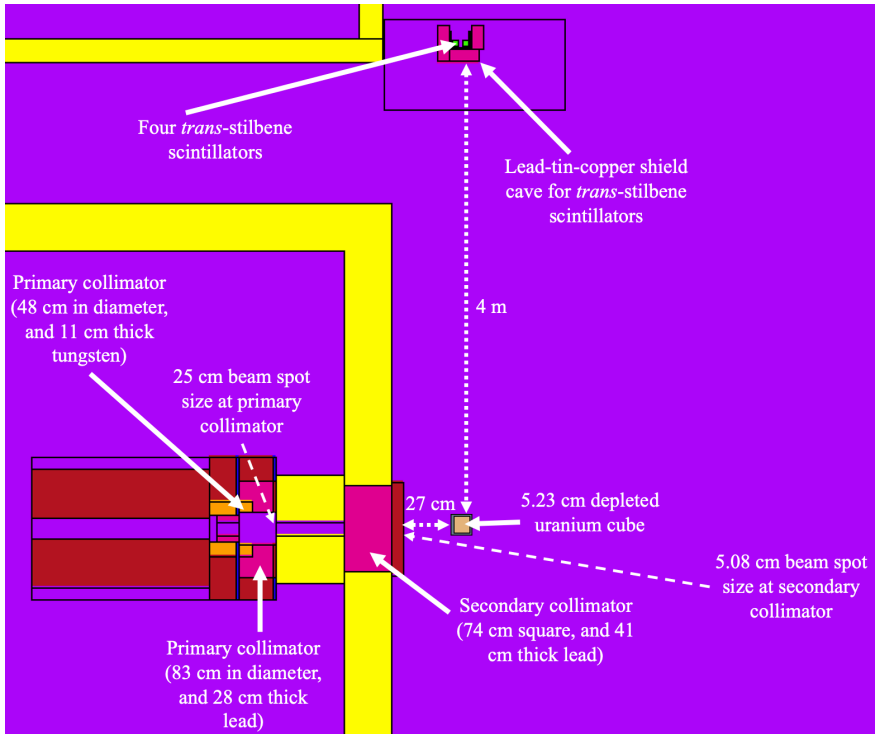

Figure 6.1. Detailed geometry of the experimental setup for the interrogation of depleted uranium and lead targets. (Geometry is defined in MCNPX-PoliMi) [53].

The same four *trans*-stilbene detectors setup described in section 5.4.1 was used for the detection of photoneutrons. The front and the sides of the cave consisted of 10.16 cm thick lead.

There was 5.08 cm thick lead at the top and bottom of the cave. The tin and copper were 0.64 cm thick and provided shielding to Kα and Kβ X-rays, which are produced in lead because of high-energy bremsstrahlung absorption [52]. Additionally, the detectors were placed perpendicular to the beam axis at 4 m from the front of the shield cave to the edge of the DU cube. This 4 m source-to-detector distance helped reduce the probability of piled-up events, which is dependent on the radiation flux and voltage pulse width. The schematic of the experimental setup is shown in Figure 6.1.

6.1.2 Data Analysis

Time gating was performed to analyze detection events that arrived during the linac pulses. This time gating facilitated discrimination of prompt photoneutrons from delayed fission neutron, which are emitted through β-decay of photofission fragments. Additionally, all data were processed with a lower light output threshold of 0.28 MeVee and an upper threshold of 2.67 MeVee. This light output window corresponds to a proton recoil energy of 1.66 – 2.67 MeV.

Scintillation events that arrived during the linac pulses were processed with the developed artificial neural network (ANN) system described in section 5.1. The ANN system identifies neutron, photon, and piled-up pulses and recovers neutron and photon information from piled-up events.

6.2 Monte Carlo Simulations with MCNPX-PoliMi

The measurement was simulated with the MCNPX-PoliMi transport code [29,30] using the ENDF/B-VII photonuclear cross-section library [7]. The MCNPX-PoliMi is a well-established particle transport code that has been validated with experiments [54,55]. The ENDF/B-VII library was selected because it contains updated photonuclear cross-sections for 163 isotopes up to 140

MeV photon energies [7]. The evaluations of these cross-sections were performed using methodology and modelling tools developed at Los Alamos National Laboratory in collaboration with the International Atomic Energy Agency [56].

The simulation was performed in three steps: 1) electron simulation, 2) photoneutron simulation, and 3) detector response simulation. For the electron simulation, 10 MeV monoenergetic electrons were modeled in MCNPX-PoliMi. The 10 MeV energy of the electron is based on a previous beam quality measurement performed at the University of Michigan [57]. The electron source was defined as a point source at a radial distance of 0.05 cm from the x-ray converter target. The source electrons were directed in the forward direction i.e., 0° with respect to the radial distance. A photon current tally (MCNPX type 1 tally) was used to obtain a bremsstrahlung spectrum at the secondary collimator opening. This photon current tally was cosine-binned between 0°-90° and 90°-180°; the angle of cosine in MCNPX-PoliMi is defined with respect to a vector normal to the surface in the outward direction. The tally result in the 0°-90° bin provided the energy spectrum of bremsstrahlung photons exiting the secondary collimator.

The obtained bremsstrahlung spectrum was then used as a source to model photoneutron production in the depleted uranium target. For the photoneutron simulation, photon source was defined as a spherical source of radius 2.54 cm at the exit of the secondary collimator. The photoneutrons exiting the face of depleted uranium towards the detector array was tallied using the cosine- and an energy-binned neutron current tally (MCNPX type 1 tally). The cosine bin widths were set to 5°, and the energy bin widths were set to 0.1 MeV. The energy-binned tally result in the 0°, 5°, 10°,….., 90° cosine bins were used to define photoneutron source term for the detector response simulation. The photoneutron source was defined as a planar source at the face of depleted uranium towards the detector array. During the detector response simulation, a particle

collision file was generated, which included photoneutron collision information in all four *trans*-stilbene detectors.

All three steps of the simulation were performed in a detailed geometry that included structural components of the linac, primary and secondary collimation of bremsstrahlung photons, beam dump, and details of the laboratory space, such as ceiling, floor, and support columns. The screenshot of the geometry is shown in Figure 6.1.

The MCNPX-PoliMi writes to a dedicated output file the main parameters of each collision event that occurs in user-defined cells. The information included in the output file is listed in Table 6.1 and a screenshot of an example collision file is shown in Figure 6.2. The collision file from MCNPX-PoliMi was processed with a post-processing algorithm i.e., MPPost [58]. MPPost is a FORTRAN program that simulates detector responses using the information provided in the particle collision file. A block diagram illustrating the process of converting energy deposited by particles in user-defined cells to detector response is shown in Figure 6.3.

1	974	10	1	-99	1001	550	0.789176	27.40	535.09	691.79	75.09	1.000E+00	0	10	0	1.507E+00
2	974	10	1	-99	6000	550	0.102534	27.48	534.53	691.27	74.54	1.000E+00	0	11	0	7.176E-01
3	974	10	1	-99	6000	550	0.075727	27.72	532.96	693.26	73.87	1.000E+00	0	12	0	6.151E-01
4	974	10	1	-99	6000	550	0.143366	27.85	533.75	694.07	73.32	1.000E+00	0	13	0	5.393E-01
5	974	10	1	-99	1001	550	0.039837	27.97	532.93	693.42	73.19	1.000E+00	0	14	0	3.958E-01
6	974	10	1	-99	1001	510	0.018741	32.64	524.26	690.90	71.18	1.000E+00	0	22	10	1.687E-01
7	974	10	1	-99	6000	510	0.030381	32.87	525.47	690.57	71.11	1.000E+00	0	23	10	1.500E-01

Figure 6.2. Screenshot of the particle collision file from detector response simulation to a ^{252}Cf spontaneous fission source using MCNPX-PoliMi.

The Birks function [59] defined in eq. 2-3 was used to convert energy deposited to light output. The MPPost processed data was scaled to photoneutron count rate i.e., CPS using,

$$CPS = \frac{N_{MPPost}}{n_{emitted}} * \frac{n_{emitted}}{B_{incident}} * \frac{B_{incident}}{E_{electron}} * \frac{I_{e,peak}}{q_e} * DF. \quad 6\text{-}1$$

In eq. 6-1, $I_{e,peak}$ is the peak linac current (97.2 mA), q_e is elementary charge, and DF is the duty factor of the linac (0.02%). The term $B_{incident}/E_{electron}$ represents total bremsstrahlung photons produced per incident electron, which is the sum of energy-binned photon current tally from the

electron simulation. The sum of cosine- and energy-binned neutron tally from step 2 of simulation (photoneutron simulation) provided total photoneutrons emitted from depleted uranium per incident bremsstrahlung photon i.e., $n_{emitted}/B_{incident}$. The term $N_{MPPost}/n_{emitted}$ represents total neutrons detected in *trans*-stilbene detectors per emitted photoneutron, which was calculated by MPPost.

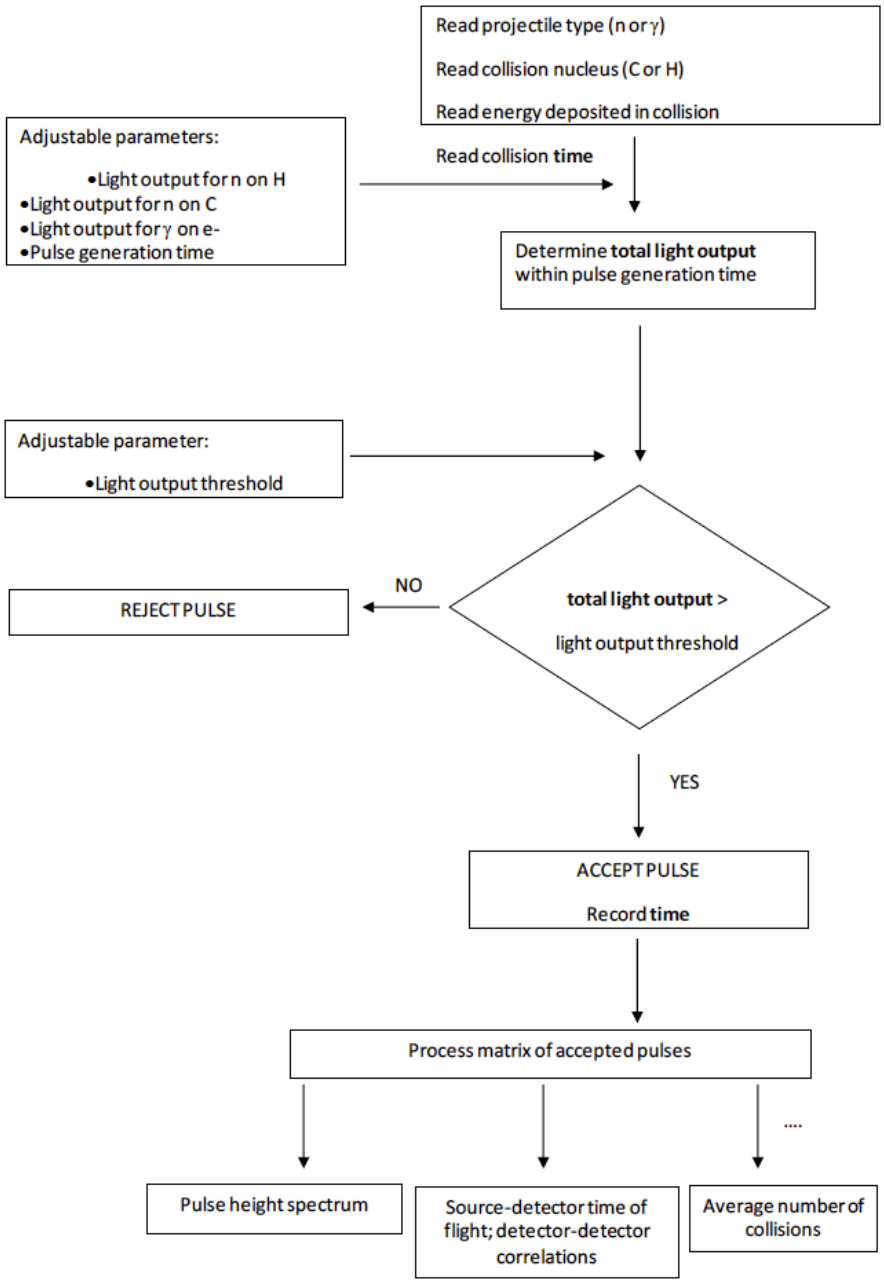

Figure 6.3. Block diagram for detector response simulation using MPPost [60].

In eq. 6-1, $I_{e,peak}$ and DF are the sources of systematic errors. The average repetition rate of the linac was measured to be 44.15 Hz with a standard deviation of 0.09 Hz. This deviation in the linac repetition rate was accounted for in the duty factor and the scaled photoneutron count rate. The M9 linatron is a robust accelerator, and therefore an uncertainty of 1% was assumed with the peak linac current i.e., $I_{e,peak}$. This 1% uncertainty was propagated in the scaled photoneutron count rate. The remaining terms in eq. 6-1 are the sources of statistical errors. A large number of source particles were sampled during each step of the photonuclear simulation such that the statistical uncertainty was less than 0.001%.

Table 6.1. Particle collision information provided by MCNPX-PoliMi in the output file [60].

nps	Starting event ID
$npar$	Particle identification number
ipt	Particle type (1 = neutron, 2 = photon, and 3 = electron)
$ntyn$	Collision type
$nxs(2, iex)$	Target nucleus ZAID identification
$ncl(icl)$	Cell number where the collision took place
$EnReCo$	Energy deposited in the collision (MeV)
tme	Time in shakes
xxx	x – coordinate of the position at which collision took place
yyy	y - coordinate of the position at which collision took place
zzz	z - coordinate of the position at which collision took place
wgt	Weight of the incident particle
$ngen$	Generation number of incident particle (it increases after a fission event)
$nsca$	Number of scatterings (elastic for neutrons and Compton for photons) from birth
$ncode$	Code of the reaction which produced the incident particle
erg	Doppler broadened energy of incident particle

6.3 Results and Discussion

6.3.1 Measurement

Figure 6.4 shows the detected pulse integrals for lead and depleted uranium interrogations before and after the elimination of piled-up events. Figure 6.4 a and c show that there are significant piled-up events that greatly deteriorate the neutron and photon detection capabilities of the *trans*-stilbene scintillators. Figure 6.4 b and d show the results after applying the developed ANN system. A good separation between neutrons and photons is observed; the ANN system successfully identified the piled-up events.

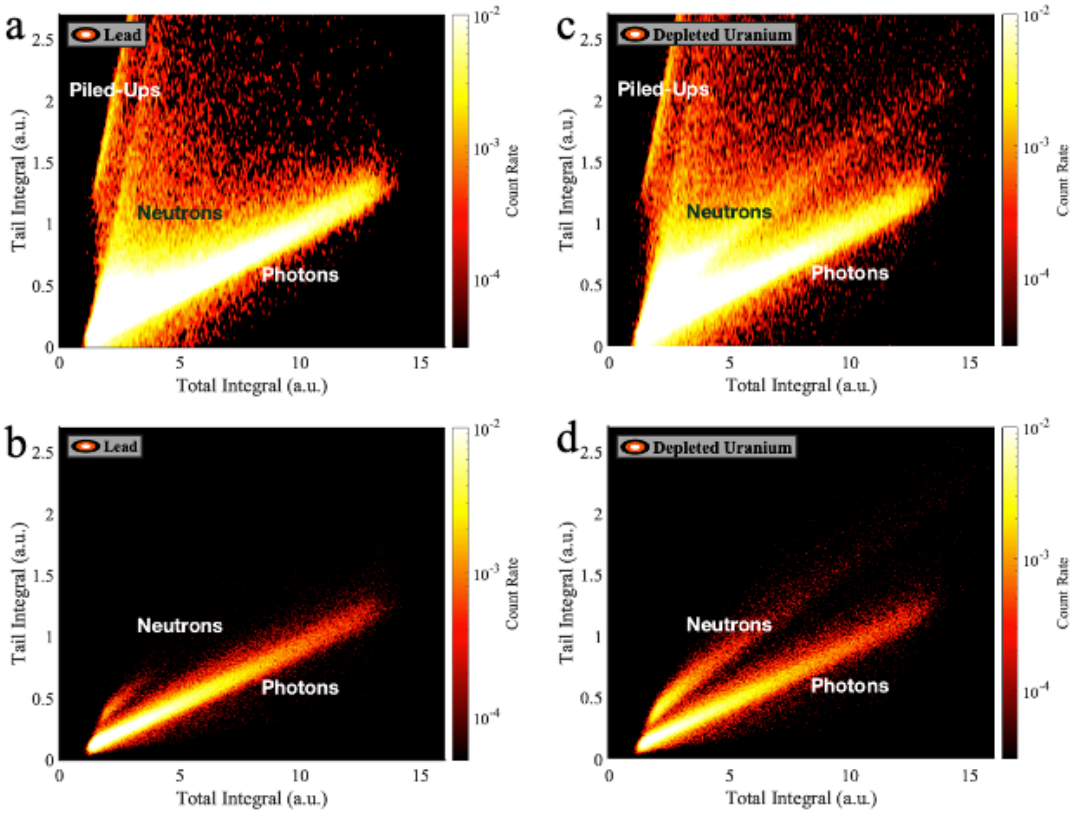

Figure 6.4. Neutron and photon integrals for - a) lead before elimination of piled-up events, b) lead after ANN elimination of piled-up events, c) depleted uranium before elimination of piled-up events, and d) depleted uranium after ANN elimination of piled-up events [53].

Figure 6.5a shows the measured light output distributions for DU and lead. We observed a 5x increase in the photoneutron count rate when the lead target was replaced with the DU target

Additionally, the measured light output distribution for lead photoneutrons is much softer than the DU photoneutron light output distribution. This difference in the light output distributions is due to the known difference in the photoneutron energy spectra. The DU photoneutrons are emitted with two energy spectra i.e., (γ, n) and Watt spectra whereas lead photoneutrons are emitted with only (γ, n) spectrum (Figure 2.4).

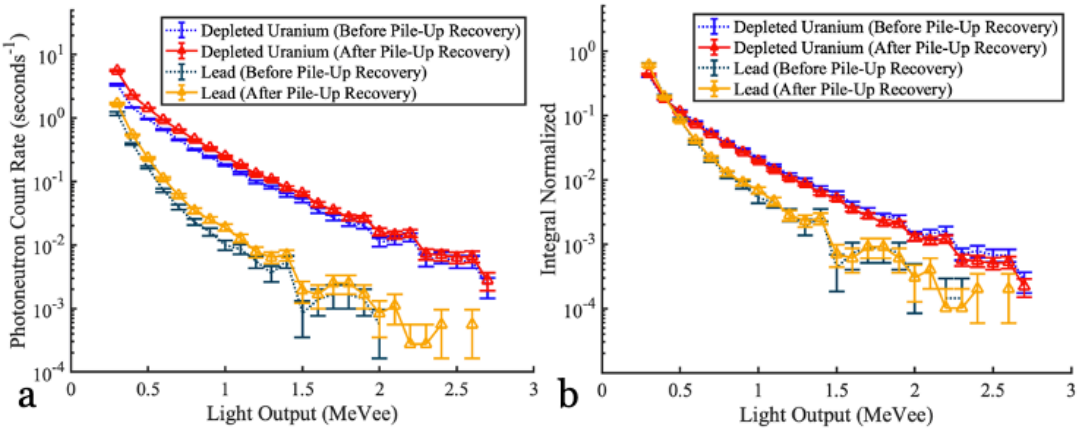

Figure 6.5. Measured photoneutron light output distributions for lead and depleted uranium- a) absolute comparison and b) integral normalized comparison. (*Active background is subtracted from each distribution. Error bars are from Poisson counting statistics and are represented within one standard deviation.*) [53]

Without any pile-up recovery, the photoneutron count rate is 1.92 ± 0.07 counts per second for lead and 8.22 ± 0.11 counts per second for DU. After information is recovered from piled-up events, the count rate increases to 2.76 ± 0.08 counts per second for lead and 12.68 ± 0.14 counts per second for DU. We observed that the shape of the photoneutron light output distributions remains unaffected after recovery of piled-up events (Figure 6.5b). This constant shape implies that pile-up recovery provides an efficiency boost of approximately 31% for neutron detection.

6.3.2 MCNPX-PoliMi

A passive ^{252}Cf measurement was performed to validate the MCNPX-PoliMi input geometry and the *trans*-stilbene detector response from MPPost. The ^{252}Cf spontaneous fission

source was placed 4 m from the front of the lead-tin-copper shield cave, which is the same as the DU to shielding distance. The measured data was analyzed with the ANN system.

Figure 6.6 shows the measured and simulated neutron light output distributions. The simulated and measured neutron count rates agree within (8.5 $\pm$ 0.9) %. The measured count rates before and after recovery of piled-up events are statistically identical, which is expected due to the low activity of the ^{252}Cf source i.e., 872 $\pm$ 15 μCi on June 19th, 2022, and a large source-to-detectors distance (> 4 m). The passive ^{252}Cf result demonstrates the accuracy of the MCNPX-PoliMi transport code and the ability to accurately simulate *trans*-stilbene detectors response to a fission source.

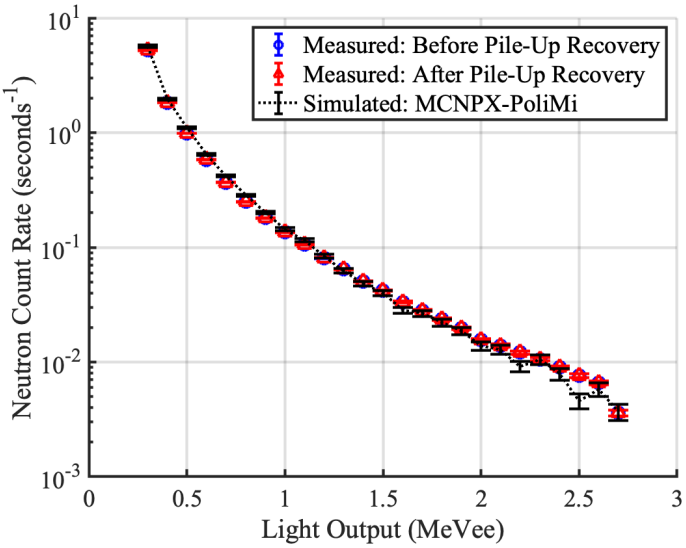

Figure 6.6. Measured and simulated neutron light output distributions from a ^{252}Cf spontaneous fission source. (*Errors bars are from Poisson counting statistics and are represented within one standard deviation.*)

Figure 6.7 shows the measured and simulated photoneutron light output distributions for DU. For a light output window of 0.28 – 0.60 MeVee, the simulation is found to overestimate the measured result. This overestimation is due to the information that is lost to unrecoverable piled-up events (29.5% of the collected data was eliminated). Nearly 75% of these unrecoverable piled-up events were voltage signals that have a small amplitude (less than 0.60 MeVee) and a poor

voltage signal-to-noise ratio. The developed MCNPX-PoliMi framework does not simulate pulse pile-up effect in *trans*-stilbene scintillators.

For a light output window of 0.60 – 2.67 MeVee, the simulation was found to under-predict the measured result by an average of 33.3 ± 1.2%. The underprediction of simulation versus experiment in our result confirms the previously reported underprediction when using ENDF/B-VII photonuclear cross-section data for uranium [8,9].

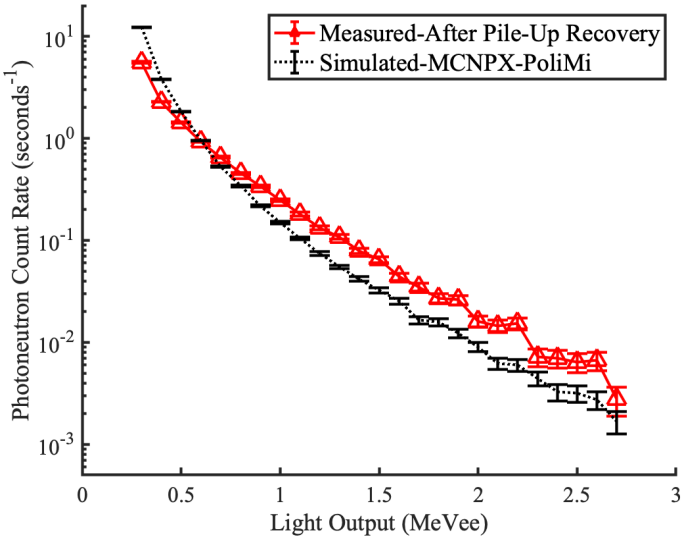

Figure 6.7. Measured and simulated photoneutron light output distributions for depleted uranium. (*Represented error bars are within one standard deviation.*) [53]

Frankl and Macian-Juan [61] performed a photonuclear benchmark study of natural uranium with MCNPX using ENDF/B-VII cross-section libraries. In the benchmark study, the MCNPX results were compared to measured results that were obtained by Barber and George in 1959 [62]. The simulation was found to under-predict the measured count rate by 8.7 ± 15.1% for a 0.98 cm thick natural uranium target interrogated with bremsstrahlung photons produced by 11.5 MeV electrons. In the present work, the DU cube was 5.23 cm and was interrogated with bremsstrahlung photons produced by 9 MeV electrons. An underestimation of 33.3 ± 1.2% in the simulated photoneutron count rate was observed. The underprediction of simulation versus

experiment is consistent with the Frankl and Macian-Juan result, and therefore, the result gives confidence that the developed ANN system is correctly recovering information from piled-up events.

6.3.3 Time to Detection

It has been demonstrated in the literature that time-of-flight techniques can be used to discriminate fissionable materials from other photoneutron producing targets, such as lead [63]. Another technique exploits the difference in the prompt neutron yield parallel and perpendicular to the plane of high-energy photon beam polarization. This difference in prompt neutron yield is referred to as polarization asymmetry [20,21]. Both time-of-flight and polarization asymmetry techniques described in the literature are non-trivial to be implemented in the field for applications, such as cargo scanning applications wherein high-energy photon interrogation systems are used for SNM detection.

The observed difference (Figure 6.5) in the photoneutron light output distributions of lead and DU can be exploited to discriminate actinides from other non-fissionable neutron producing targets. A light output window of 1.00 – 2.67 MeVee is selected. This light output window corresponds to a proton recoil energy of 3.68 – 6.85 MeV, which is sufficiently high to eliminate (γ, n) photoneutrons. Only prompt photofission neutrons are energetic enough to deposit such high energy in the scintillator, and therefore, false positive alarms can be reduced in the field by counting neutrons that deposit energies between 3.68 – 6.85 MeV. False positives are of great concern in cargo scanning.

Figure 6.8 shows the photoneutron count rate in the 1.00 – 2.67 MeVee light output window as a function of interrogation time. The photoneutron count rate with the presence of DU was greater than the active background count rate by three standard deviations during the first 30

seconds of interrogation. This result demonstrates that an actinide may be flagged in the field as quickly as 30 seconds, which is well within the American National Standard Institute (ANSI) standard inspection times for clearing cargo packages [64].

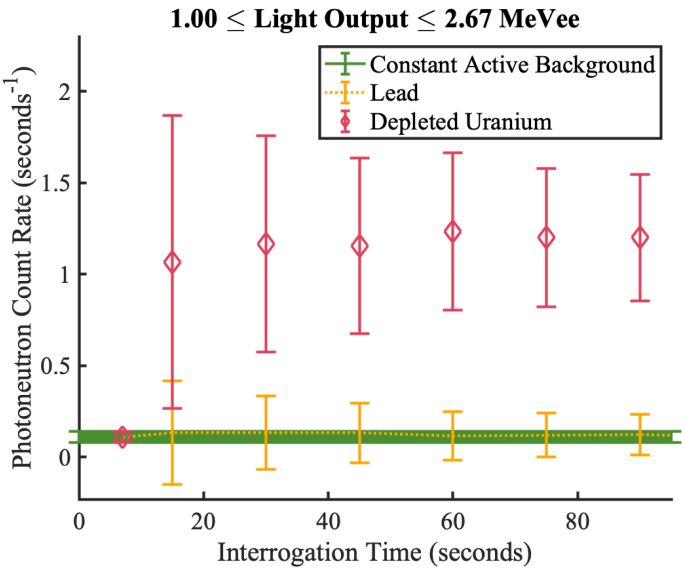

Figure 6.8. Photoneutron count rates in depleted uranium and lead as a function of interrogation time. (*Error bars are from Poisson counting statistics and are represented within three standard deviations*.) [53]

6.3.4 Different Masses of Depleted Uranium

Three different masses of DU i.e., 2.4 kg, 4.8 kg, and 7.2 kg were interrogated with the 9-MV linac. The goal of this measurement was to study photoneutron count rates with increasing mass of SNM surrogate. Each mass of DU was 10.16 cm in height and 10.16 cm in width. The thicknesses were 1.27 cm, 2.54 cm, and 3.81 cm. Figure 6.9 shows the photoneutron count rates in all three masses of DU. The count rate increased with an increase in the mass of DU, which is due to the increased photonuclear reaction rates. The 4.8 kg DU has a photoneutron count rate that is approximately 1.4x greater than the 2.4 kg DU. The photoneutron count rate in 7.2 kg DU is only 1.1x greater than the count rate in 4.8 kg DU. It appears that the photoneutron count rate increases and reaches an asymptote with increasing mass of the DU target. This asymptote trend is because of the mean free path of high-energy photons in DU. The mean free path of a 10 MeV

photon in DU is approximately 0.96 cm [65], and therefore increasing the thickness any further does not increase photoneutron production significantly.

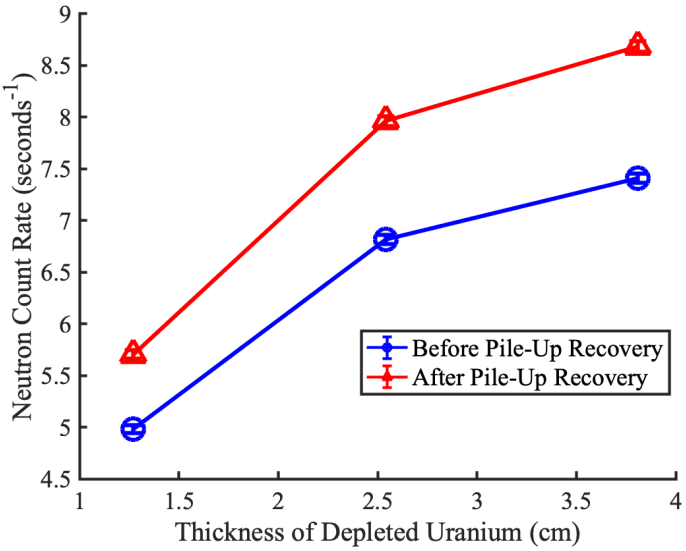

Figure 6.9. Photoneutron count rates with increasing mass (thickness) of DU.

6.4 Summary and Remarks

I presented measured results that demonstrate the detection of prompt photofission neutrons from a depleted uranium cube. These neutrons were detected with *trans*-stilbene organic scintillators, state-of-the-art detectors that are spectroscopy capable. The pulse pile-up caused by the intense bremsstrahlung photons deteriorated the particle discrimination capabilities of the *trans*-stilbene scintillator. To address the pulse pile-up issue, I applied a neural-network-based digital processing of scintillation pulses. The information recovered from neutron piled-up events provided an efficiency boost of approximately 31% to the interrogation system.

I also exploited the difference in the measured photoneutron light output distributions of lead and DU to discriminate between (γ, n) and photofission neutrons. By selecting a light output window of 1.00 – 2.67 MeVee, I demonstrated that an actinide, such as uranium, can be detected as quickly as 30 seconds, and differentiated from a non-fissionable material, such as lead.

Additionally, different masses of DU were interrogated, and prompt photofission neutrons were successfully detected from the smallest mass i.e., 2.4 kg.

I further presented a framework that can be used to simulate active interrogation experiments with the MCNPX-PoliMi transport code. The MCNPX-PoliMi is a modified version of the MCNPX transport code that can accurately model photonuclear and particle detection physics (detector responses). The developed framework was validated with measured results using a ^{252}Cf source. In the photonuclear experiments, for a light output window of 0.70 – 2.67 MeVee, the simulated result was found to under-predict the measured result by $33.27 \pm 3.61\%$. This result is expected due to the known under-prediction in the photonuclear cross-section data for uranium. Additional work is needed to estimate discrepancies between measurement and simulation for light output values below 0.70 MeVee.

Chapter 7 Interrogation of Shielded Depleted Uranium

During the interrogation of bare depleted uranium (DU), nearly 30% of the collected data was eliminated because it was unclassifiable by the developed ANN system. Most of the eliminated data (approximately 75%) were voltage pulses that had a small amplitude and a poor signal-to-noise ratio. Due to the elimination of the data, the simulated results were found to over-predict the measured results in the 0.28 to 0.60 MeVee light output. To reduce the amount of data that is eliminated during interrogation measurements, iron and polyethylene shielding was introduced around the DU cube. This chapter provides the details of the measurement setup and the measured results from DU when shielded in various iron and polyethylene configurations. The measurements were simulated in the MCNPX-PoliMi transport code using the framework developed in section 6.3.2. The comparison of the simulated and measured results is presented in this chapter, which provides quantitative assessment of the under-prediction in the photonuclear cross-section data for uranium. The results presented in this chapter are currently under review in the Nuclear Science and Engineering journal [66].

7.1 Setup and Data Analysis

The same measurement setup described in section 6.1.1 was used for the interrogation of DU in various iron and polyethylene shielded configurations. Four *trans*-stilbene organic scintillators coupled to PMTs, and shielded in a lead-tin-copper shield cave were used for fast neutron detection.

The interrogation of DU was performed in various iron and polyethylene shielded configurations. Both iron and polyethylene shielding were hollow boxes of varying wall thicknesses. The iron wall thickness extended up to 6.35 cm and the polyethylene wall thickness extended up to 15.24 cm. The distance between DU and collimator opening was constant i.e., 27 cm, across all configurations. Both iron and polyethylene shielding around DU were studied because iron primarily attenuates bremsstrahlung photons, which reduces photoneutron production in the target whereas polyethylene primarily attenuates the produced photoneutrons. All measurements with DU were performed for one hour. Additionally, a one-hour measurement was performed with no target present to quantify photoneutrons produced in the photon collimator. This measurement with no target is referred to as the active background. The photograph from the interrogation of DU shielded in 5.08 cm thick polyethylene configuration is shown in Figure 7.1.

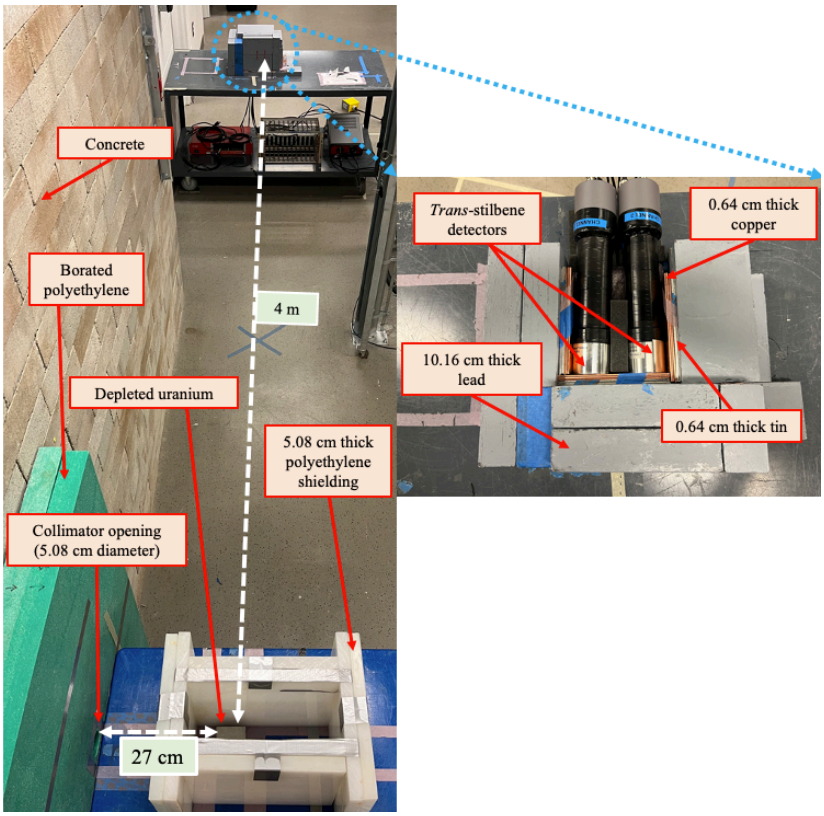

Figure 7.1. Photographs of the measurement setup for the interrogation of depleted uranium in shielded configurations [66].

The analysis of the measured data was performed similarly to the analysis described in section 6.1.2. Time gating was performed to separate during and in-between linac pulses *trans*-stilbene detections. The scintillation events that were detected during linac pulses were processed with the developed ANN system (section 5.1).

The validated MCNPX-PoliMi framework described in section 6.2 was used to simulate various iron and polyethylene shielded configurations of DU. The Briks function was used to convert energy deposited to light output (eq. 2-3). The collision file obtained from MCNPX-PoliMi was processed with MPPost [58], and the output from MPPost was scaled to photoneutron count rate using eq. 6-1.

7.2 Results and Discussion

7.2.1 Breakdown of Scintillation Pulses

Figure 7.2 shows the breakdown of scintillation pulses from the *trans*-stilbene organic scintillators during interrogation of depleted uranium in various shielded configurations. The developed ANN system broadly categorized voltage pulses into three broad categories: singles, recoverable piled-up events, and unclassifiable piled-up events. The singles and recoverable piled-up events were further classified as neutrons and photons whereas unclassifiable events were eliminated. These unclassifiable piled-up events included triple/quadruple pile-ups and voltage pulses that were extremely noisy. The noisy pulses constituted most unclassifiable piled-up events, and the ANN system was unable to classify them as neutrons and photons with confidence.

For both iron and polyethylene shielded configurations, the total scintillation pulses decreased with an increase in the shield wall thickness. This decreasing trend is due to the attenuation of bremsstrahlung photons by iron and the moderation of neutrons by polyethylene. The percentage of voltage pulses categorized as singles increased with an increase in iron wall

thickness i.e., from 62% to 83%, This increase in the number of clean signals is due to the attenuation of photons, which causes pulse pile-up. For the polyethylene shielded configurations, the singles constituted an average of 60% of the total scintillation pulses across all thicknesses. This nearly constant percentage of singles is because a low-Z material like polyethylene has a small effect on the bremsstrahlung radiation.

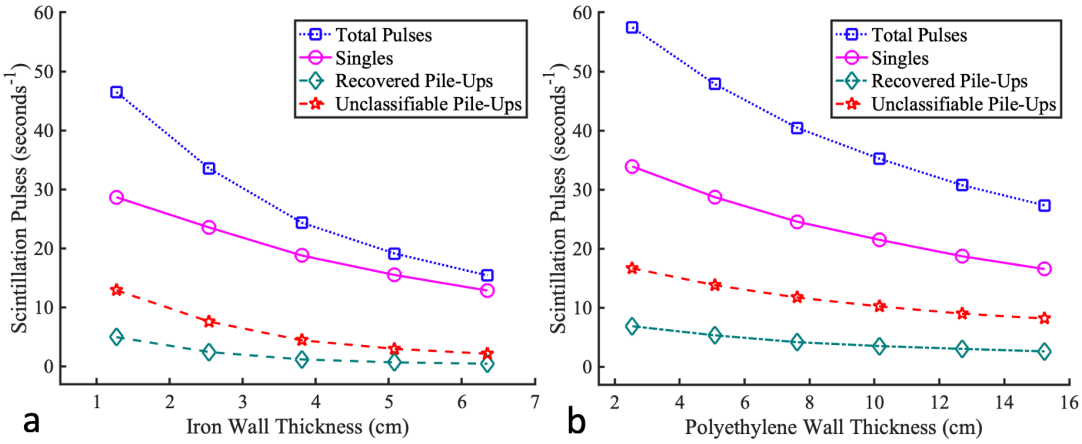

Figure 7.2. Breakdown of scintillation pulses from the *trans*-stilbene detectors during interrogation of depleted uranium: a) iron shielded configurations and b) polyethylene shielded configurations.

Figure 7.3 and Figure 7.4 shows the tail and total integrals of neutrons and photons detected during linac active interrogation of depleted uranium shielded in the least and greatest thicknesses of iron and polyethylene with and without the piled-up events. The results shown in Figure 7.3 and Figure 7.4 demonstrates the ANN ability to accurately identify singles, and a good separation was is observed between neutrons and photons without any piled-up events in the PSD plots.

7.2.2 Photoneutron Count Rate

Figure 7.5 shows the bremsstrahlung photon spectrum at the exit of the secondary collimator obtained from the electron simulation. The ENDF/B-VII photonuclear cross-section data for (γ, n), $(\gamma, 2n)$, and $(\gamma, fission)$ reactions are also represented in Figure 7.5. The Q-value

for (γ, n) photonuclear reactions in ^{238}U is 6.2 MeV and the threshold for (γ, f) reactions is 5.5 MeV.

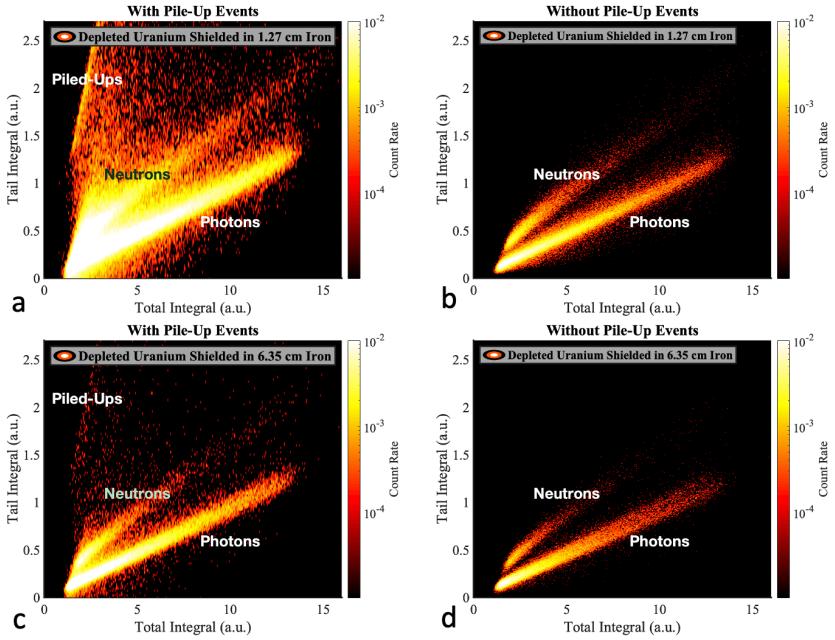

Figure 7.3. Neutron and photon tail and total pulse integrals for depleted uranium shielded in a) 1.27 cm iron (before pile-up recovery), b) 1.27 cm iron (after pile-up recovery), c) 6.35 cm iron (before piled-up recovery), and d) 6.35 cm iron (after pile-up recovery) [66].

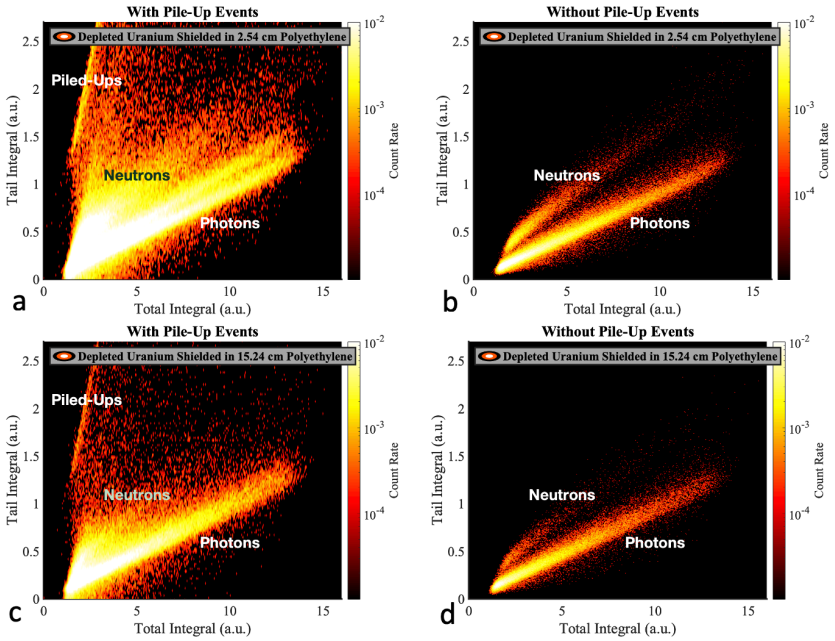

Figure 7.4. Neutron and photon tail and total pulse integrals for depleted uranium shielded in a) 2.54 cm polyethylene (before pile-up recovery), b) 2.54 cm polyethylene (after pile-up recovery), c) 15.24 cm polyethylene (before piled-up recovery), and d) 15.24 cm polyethylene (after pile-up recovery) [66].

There are no photoneutrons from the $(\gamma, 2n)$ reactions as the endpoint energy of the bremsstrahlung radiation is less than the reaction threshold energy in ^{238}U (Q-value for $(\gamma, 2n)$ in ^{238}U is 11.3 MeV). Approximately 9% of the total bremsstrahlung spectrum is emitted with energies greater than 5.5 MeV, and therefore only a fraction of emitted photons induces photonuclear reactions in the depleted uranium target. The rest of the bremsstrahlung photons does not contribute to photoneutrons production; however, they constitute an intense photon background and cause pulse pile-up issues in *trans*-stilbene detectors.

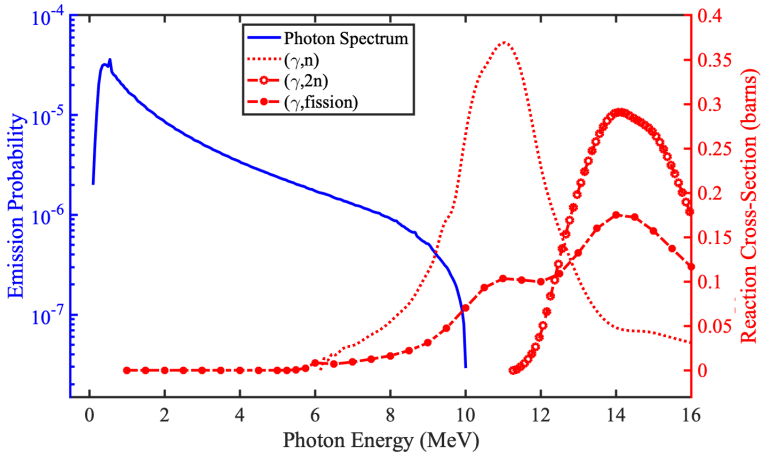

Figure 7.5. ENDF/B-VII photonuclear cross-section data [7] for ^{238}U superimposed with the bremsstrahlung photon spectrum.

Figure 7.6a shows the measured and simulated photoneutron count rate for depleted uranium shielded in various thicknesses of iron. Both measured and simulated count rates decreased with an increase in iron wall thickness. This decreasing trend is expected because the attenuation of bremsstrahlung radiation caused by iron reduces (γ, n) and $(\gamma, fission)$ photonuclear reaction rates in depleted uranium, which reduces the production of photoneutrons. Figure 7.6b shows the measured and simulated photoneutron count rates for depleted uranium shielded in various polyethylene configurations. We again observed a decreasing trend in the measured and simulated count rates, which is expected because polyethylene is a neutron moderator, and therefore, it can reduce the neutron energy below detection thresholds.

The pile-up events were processed with the ANN pile-up recovery to restore neutron information. For the 1.27 cm thick iron configuration, pile-up recovery constituted nearly 27% of the total photoneutron count rate. The percentage of recovered neutrons was reduced to 5% for the 6.35 cm thick iron configuration. This reduced recovery in neutron information is due to reduced pulse pile-up. The simulated photoneutron count rate for this minimally piled-up affected iron configuration was found to under-predict the measured count rate by 25.9 $\pm$ 3.3%. This thickest iron configuration, which has the highest percentage of collected data classified as singles, establishes a reference value to quantify the discrepancy between measurement simulation and simulation. For the 1.27 cm and 2.54 cm thick iron configurations, the discrepancy between the measured and simulated photoneutron count rates improved after pile-up recovery; however, the simulated rate is over predicting the measured rate, which is due to the information that is lost to unclassifiable piled-up events.

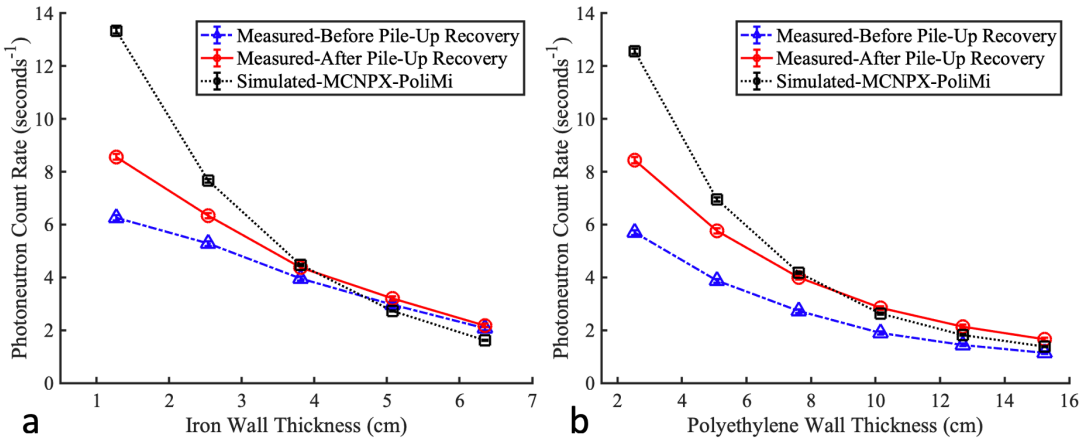

Figure 7.6. Simulated and active background subtracted photoneutron count rates: a) depleted uranium shielded in varying thickness of iron and b) depleted uranium shielded in varying thickness of polyethylene. (*Error bars are from Poisson counting statistics and are represented within one standard deviation.*)

For all six polyethylene configurations, pile-up recovery constituted an average of 32% of the total photoneutron count rate. For the 2.54 cm, 5.08 cm, and 7.62 cm thick polyethylene configurations, the simulated rate is found to over-predict the measured rate (after pile-up

recovery). The discrepancy between simulation and measurement was observed to reach an asymptote with increasing polyethylene wall thickness. For the 12.70 cm and 15.24 cm thick configurations, the simulated count rate under-predicted the measured rate by 14.7 ± 3.3% and 16.9 ± 3.9% respectively. This under-prediction is consistent with the reference value obtained from the iron shielded configurations.

In 2015, Frankl and Macian-Juan performed a photonuclear benchmark study using MCNPX with ENDF/B-VII cross-section library [61]. The authors used measurement data that were obtained by Barber and George in 1959 [62]. For a 0.98 cm thick natural uranium target interrogated with a 11.5-MV electron linac, Frankl and Macian-Juan found that the simulated count rate under-predicts the measured rate by 8.7 ± 15.1%. In the present work, the depleted uranium target is 5.23 cm thick and interrogated with a 9-MV linac. The reference under-prediction value obtained from the maximum iron configuration is 25.9 ± 3.3%. This under-prediction is consistent with the Frankl and Macian-Juan results. However, due to huge uncertainty in the measured result by Barber and George, it cannot be concluded that the under-prediction obtained in the present study agrees with the 8.7 ± 15.1%. The ENDF/B-VII provided an integral validation of the photonuclear cross-section for ^{235}U [7]. This validation found that the discrepancy between measurement and simulation can vary between 20 – 30%. The reference under-prediction in the present work lies between 20 – 30% range, which provides confidence in the obtained result.

7.2.3 Photoneutron Light Output Distributions

Figure 7.7 shows the normalized photoneutron light output distribution for depleted uranium shielded in 2.54 cm thick iron and 2.54 cm thick polyethylene configurations. For both shielded configurations, the measured distributions have the same shape before and after recovery of piled-up events. This same shape implies that pile-up recovery provided an efficiency boost for

neutron detection i.e., pile-up recovery increased photoneutron counts, thereby providing a higher neutron detection efficiency. Additionally, this result helps build confidence in the recovery of piled-up events through the ANN system.

Figure 7.8 shows the measured and simulated photoneutron light output distributions for the least and greatest thicknesses of iron and polyethylene tested in this work. For the least thicknesses of shielding i.e., 1.27 cm for iron and 2.54 cm for polyethylene, the simulated count rate over-predicted the measured count rate in the 0.28 to 0.60 MeVee light output window. This over-prediction is due to the information that is lost to unclassifiable piled-up events. Nearly 75% of these unclassifiable piled-up events were voltage signals that were noisy and had a small amplitude i.e., less than 0.6 MeVee. The simulation was found to under-predict the measurement in the 0.70 to 2.67 MeVee light output window by an average of 35.4 $\pm$ 2.1%.

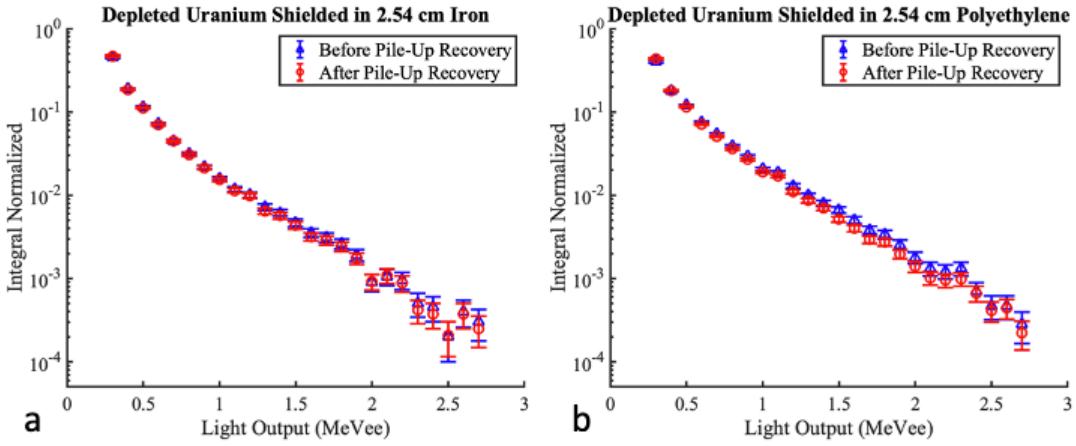

Figure 7.7. Normalized photoneutron light output distributions for depleted uranium shielded in a) 2.54 cm thick iron and b) 2.54 cm thick polyethylene. (*Error bars are represented within one standard deviation.*)

For the greatest thicknesses of shielding i.e., 6.35 cm for iron and 15.24 cm for polyethylene, the simulation was under predicting the measured result across the entire light output window of 0.28 to 2.67 MeVee. This under-prediction between simulation and measurement is

25.9 ± 3.3% for the 6.35 cm thick iron case and 16.9 ± 3.9% for the 15.24 cm thick polyethylene case.

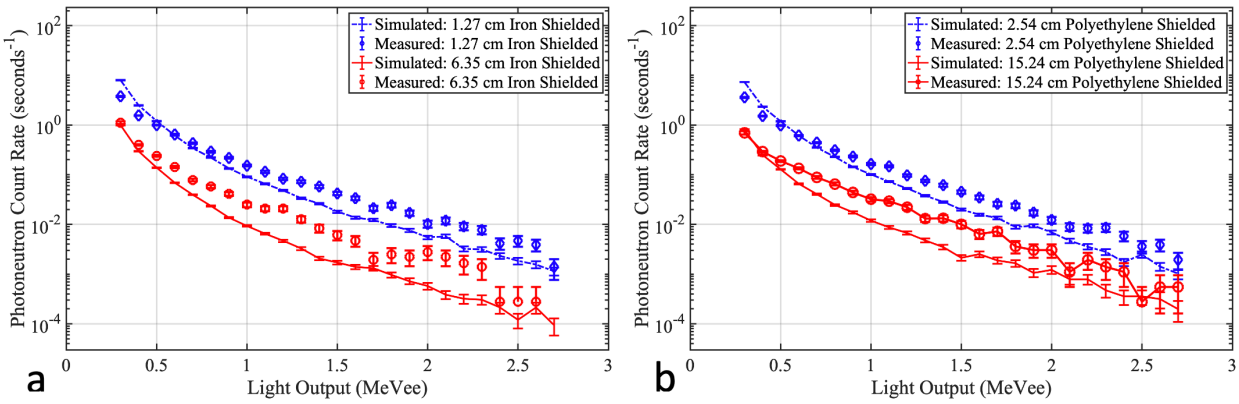

Figure 7.8. Simulated and active background subtracted photoneutron light output distributions for the least and greatest thickness of a) iron shielding and b) polyethylene shielding. (*Errors bars are from Poisson counting statistics and are represented within one standard deviation.*)

The discrepancy between results of the thickest iron and polyethylene shielded configurations is due to the information that is lost to unclassifiable piled-up events. Nearly 14% of the collected data was eliminated from the thickest iron case while 30% was eliminated from the thickest polyethylene case. Assuming the eliminated data have the same neutron-to-photon ratio as single pulses, the fractional neutrons present in the eliminated data can be estimated. For depleted uranium shielded in 6.35 cm thick iron and 15.24 cm thick polyethylene, the measured neutron-to-photon ratios are 0.35 and 0.09 respectively. Using these measured ratios, the neutron fraction is computed using,

$$F_n = \frac{R}{R+1}, \tag{7-1}$$

where F_n is the neutron fraction and R is the measured neutron-to-photon ratio. The neutron fractions estimated by eq. 7-1 were used to predict the missing photoneutron count rate in the thickest iron and polyethylene shielded configurations. These count rates were 0.22 photoneutrons per second for the 6.35 cm thick iron configuration and 0.43 photoneutrons per second for the

15.24 cm thick polyethylene configuration. These fractional neutrons from the eliminated data were added to the photoneutron count rate after pile-up recovery, and the simulation was found to under-predict the measured result by 32.8 ± 3.2% for the thickest iron case and 34.0 ± 3.3% for the thickest polyethylene case. These under-predictions obtained after accounting for unclassifiable piled-up events agree with the 35.4 ± 2.1% value that was obtained from the least thicknesses of iron and polyethylene shielding in the 0.70 –2.67 MeVee light output window.

7.3 Summary and Remarks

During the interrogation of the bare DU target, nearly 30% of the collected data was eliminated, which was due to the unclassifiable piled-up events. I further mitigated pulse pile-up issues by interrogating the DU target in various iron and polyethylene shielded configurations. The measured photoneutron count rate obtained from the developed ANN system indicated a decreasing trend in the count rates with an increase in shield wall thickness. This decreasing trend is due to the attenuation of bremsstrahlung radiation by iron, and moderation of photoneutrons by polyethylene. Additionally, the effect of pile-up recovery was reduced with increasing iron wall thickness and remained constant across all configurations of polyethylene.

For the thickest case of the iron shielding, i.e., 6.35 cm, the effect of pulse pile-up was minimal. This minimally piled-up affected configuration was used to establish a reference value to quantify the discrepancy between measurement and simulation. The MCNPX-PoliMi simulation was found to under-predict the measured photoneutron count rate by 25.9 ± 3.3%. A significant portion of the collected data, i.e., 14%, was still eliminated due to unclassifiable piled-up events. Additional analysis was performed to estimate the contribution of unclassifiable piled-up events to the photoneutron count rate using the measured neutron-to-photon ratio from single pulses. After correcting for unclassifiable events, the simulation was found to under-predict

measurements by at most 33.8 ± 3.2%. For the thickest polyethylene case, i.e., 15.24 cm, after correcting for unclassifiable events, the simulation was found to under-predict the measured result by 34.0 ± 3.3%. The results obtained from the thickest iron and polyethylene shielded configurations are in good agreement within one standard deviation.

For the least thicknesses of iron and polyethylene shielded configurations, the discrepancy between simulation and measurement improved after recovering neutron information from piled-up events. For a light output window of 0.70 – 2.67 MeVee, the MCNPX-PoliMi result was found to under-predict the measured photoneutron count rate by an average of 35.4 ± 2.1%. This result obtained from the most piled-up affected configurations is in good agreement with the result obtained from the least piled-up affected configuration.

Chapter 8 Summary, Conclusions, and Future Work

8.1 Summary

This Ph.D. research provides new measured results, which can help quantify under-predictions in the photoneutron count rates for uranium by Monte Carlo codes. This quantitative assessment was achieved through a comparative study between simulation and measurement. The Monte Carlo simulation was performed using the MCNPX-PoliMi transport code with the most updated photonuclear cross-section library. For measurement of photoneutrons, a 5.23 cm thick depleted uranium (DU) target was interrogated with bremsstrahlung photons from a 9-MV linac, and fast neutrons were detected with four *trans*-stilbene organic scintillators. The intense bremsstrahlung flux from the linac creates pulse pile-up in *trans*-stilbene scintillators, thereby posing a measurement challenge for photoneutron detection.

The pulse pile-up effect was mitigated by developing and demonstrating an artificial neural network (ANN) system. The developed ANN system consists of six feed-forward neural networks that work in conjunction to classify scintillation pulses as neutrons and photons and recover particle information from piled-up events. I demonstrated the performance of the ANN system through the active ^{252}Cf measurement in which the neutron source was measured in the presence of the bremsstrahlung radiation from the linac. The ANN system outperformed traditional pulse shape discrimination methods in the intense photon environment.

Active interrogation experiments were performed on a DU cube and a lead block. The results obtained from the developed ANN system showed a 5x increase in the photoneutron count

rate when the lead target was replaced with the DU cube. Additionally, the measured light output distribution for lead photoneutrons was softer than the DU photoneutron light output distribution. This difference in the light output distributions is due to the differences in the photoneutron energy spectra. By selecting a light output window of 1.00 – 2.67 MeVee, the difference in the measured distributions was further exploited to demonstrate that an actinide, such as uranium, can be detected as quickly as 30 seconds, and differentiated from a non-SNM material, such as lead. Performing interrogation measurements in a timely manner is of interest in cargo scanning application wherein high-energy photons are used to detect hidden special nuclear materials.

The interrogation of bare DU was modelled using a developed MCNPX-PoliMi framework. The MCNPX-PoliMi simulation was validated with measured results from a ^{252}Cf spontaneous fission source. In the photonuclear experiments, the simulation over-predicted measurement in the 0.28 – 0.60 MeVee light output window. Possible reason for this under-prediction in the measured result is the elimination of unclassifiable piled-up events that resulted in loss of information.

The pulse pile-up was further reduced by introducing various iron and polyethylene shielding around DU. The minimally piled-up affected iron configuration was used to establish a reference value to quantify the discrepancy between measurement and simulation. For the thickest case of the iron shielding, i.e., 6.35 cm, after correcting for unclassifiable events, the simulation was found to under-predict measurements by at most 33.8 $\pm$ 3.2%. For the thickest polyethylene case, i.e., 15.24 cm, after correcting for unclassifiable events, the simulation was found to under-predict the measured result by 34.0 $\pm$ 3.3%. The results obtained from the thickest iron and polyethylene shielded configurations are in good agreement within one standard deviation.

For the least thicknesses of iron and polyethylene shielded configurations, the MCNPX-PoliMi result was found to under-predict the measured photoneutron count rate by an average of $35.4 \pm 2.1\%$ in the 0.70 – 2.67 MeVee light output window. This result obtained from the most piled-up affected configurations is in good agreement with the result obtained from the least piled-up affected configuration.

The consistent results obtained from the interrogation of DU in bare and various shielded configurations help build confidence in the under-prediction by Monte Carlo codes. The findings from this work provide new measured results that can help improve photonuclear cross-section data for uranium, which in turn will enhance simulation capabilities with existing Monte Carlo codes.

8.2 Conclusions

The pulse pile-up is inevitable in intense radiation environments. Neural-network-based digital pulse processing algorithms help recover information from such piled-up events, which are otherwise eliminated when using traditional pulse processing techniques. The ANN algorithm can further process scintillation pulses in real-time by implementing the algorithm on a field programmable gate array (FPGA).

The present work provides a measurement setup that can be used to detect photoneutrons in intense radiation environments. This setup does not use any coincidence counting technique, which makes the measurement setup robust for cargo scanning and nuclear waste characterization applications. The differences in energy spectra of photoneutrons from different materials are reflected in the obtained light output distributions. These differences are exploited to flag materials of interest from other hoax materials.

The present work also provides a detailed framework to simulate photonuclear physics using the MCNPX-PoliMi transport code. The developed framework begins with the electron simulation, which is the starting point for high-energy bremsstrahlung photons. Modelling photonuclear physics from the very start, i.e., electrons help capture most physical quantities of interest with fewer approximations, thereby enhancing the overall accuracy of simulated results.

The discrepancy observed between measurement and simulation is primarily caused by under-predicted photonuclear cross-section data for uranium. This result can be concluded because the validation of the MCNPX-PoliMi simulation performed with the ^{252}Cf source yielded good agreement between measurement and simulation; we can be confident that the discrepancy is not due to other cross-section data utilized in the simulation process. Precise photonuclear cross-sections are needed to accurately study responses of high-energy photon interrogation systems. Additionally, correct answers from simulation are of great importance for the design and development of interrogation systems for nuclear security and safeguard applications.

8.3 Future Work

The ANN system developed in the present work is limited to classify scintillation pulses that have light output values between 0.28 – 2.67 MeVee (1.66 – 6.85 MeV proton recoil energy). This limitation is due to the voltage thresholds applied to the time-of-flight (TOF) data, which was used to train the ANN system. The classification range can be expanded by training the ANN system with neutron and gamma-ray pulses that have light output values of less than 0.28 MeVee and greater than 2.67 MeVee. The high-confidence training data can be collected using the TOF approach discussed in section 4.1. During the TOF experiment, the gain of the measuring circuit must be selected appropriately such that neutron and gamma-ray voltage pulses have a good signal-to-noise ratio for light output values below 0.28 MeVee and above 2.67 MeVee. By expanding the

light output window, the ANN system will be able to classify neutrons that deposit energies less than 1.66 MeV.

The ANN architecture developed in the present work is a robust architecture that can be used to classify scintillation pulses from any organic scintillators coupled to either photomultiplier tubes (PMT) or silicon photomultiplier tubes (SiPM). The current work investigated the ANN system for *trans*-stilbene organic scintillator coupled to a PMT. The *trans*-stilbene scintillator is a crystal, which has limited availability and is further limited in size. Emerging new organic scintillators, such as the organic glass can be investigated for use in high-radiation environments. The current ANN system can be trained to classify scintillation pulses from organic glass coupled to either PMT or SiPM, thereby expanding the use of the ANN system.

The present Ph.D. research provides an experimental setup for measurement of photoneutrons with *trans*-stilbene detectors and a 9-MV linac. I measured SNM surrogate i.e., DU and a non-SNM target i.e., lead. Low-Z elements, such as beryllium and heavy water are of interest because of their low threshold energies for photonuclear reactions. Theoretically, these low-Z targets can produce photoneutrons up to 7 MeV energies when interrogated with 9 MeV photons. For cargo scanning applications, the 3.68 – 6.85 MeV energy window (section 6.3.3) that was used to discriminate lead from DU may not be able to discriminate SNMs from low-Z elements. Thus, supporting measurements must be performed to identify differences in the photoneutrons light output distributions for uranium and low-Z elements.

The current work further provides a framework to simulate active interrogation measurements using Monte Carlo codes, such as the MCNPX-PoliMi. The developed framework can be used to predict photoneutron count rates from other common elements such as plutonium,

iron, heavy water etc. The comparison of the predicted count rates with measured rates can help improve photonuclear cross-section data for other elements of interest in nuclear community.

Bibliography

[1] A. Danagoulian, W. Bertozzi, C. L. Hicks, A. v. Klimenko, S. E. Korbly, R. J. Ledoux, and C. M. Wilson, *Prompt Neutrons from Photofission and Its Use in Homeland Security Applications*, 2010 IEEE International Conference on Technologies for Homeland Security, HST 2010 379 (2010).

[2] B. W. Blackburn, J. L. Jones, C. E. Moss, J. T. Mihalczo, A. W. Hunt, F. Harmon, S. M. Watson, and J. T. Johnson, *Utilization of Actively-Induced, Prompt Radiation Emission for Nonproliferation Applications*, Nucl Instrum Methods Phys Res B **261**, 341 (2007).

[3] A. Sari, F. Carrel, F. Lainé, and A. Lyoussi, *Neutron Interrogation of Actinides with a 17 MeV Electron Accelerator and First Results from Photon and Neutron Interrogation Non-Simultaneous Measurements Combination*, Nucl Instrum Methods Phys Res B **312**, 30 (2013).

[4] A. Lyoussi, J. Romeyer-Dherbey, F. Jallu, E. Payan, A. Buisson, G. Nurdin, and J. Allano, *Transuranic Waste Detection by Photon Interrogation and On-Line Delayed Neutron Counting*, Nuclear Instruments and Methods in Physics Research B **160**, 280 (2000).

[5] P. M. Dighe, E. Berthoumieux, D. Doré, J. M. Laborie, X. Ledoux, V. Macary, S. Panebianco, and D. Ridikas, *Delayed Gamma Studies from Photo-Fission of 237Np for Nuclear Waste Characterization*, Ann Nucl Energy **36**, 399 (2009).

[6] C. Romano et al., *Proceedings of the Workshop for Applied Nuclear Data: WANDA2020* (2020).

[7] M. B. Chadwick et al., *ENDF/B-VII.0: Next Generation Evaluated Nuclear Data Library for Nuclear Science and Technology*, Nuclear Data Sheets **107**, 2931 (2006).

[8] A. Sari, *Characterization of Photoneutron Fluxes Emitted by Electron Accelerators in the 4–20 MeV Range Using Monte Carlo Codes: A Critical Review*, Applied Radiation and Isotopes **191**, 110506 (2023).

[9] V. V. Varlamov, *Reliability of Photonuclear Data: Various Experiments and Evaluations*, Physics of Particles and Nuclei **50**, 637 (2019).

[10] Y. Bengio, *Learning Deep Architectures for AI*, Foundations and Trends in Machine Learning **2**, 1 (2009).

[11] R. J. Olesen, J. B. Cole, D. E. Holland, E. M. Brubaker, and J. E. Bevins, *Regenerative Neural Network for Rotating Scatter Mask Radiation Imaging*, Radiat Meas **143**, (2021).

[12] R. Zhang, P. Gong, X. Tang, P. Wang, C. Zhou, X. Zhu, L. Gao, D. Liang, and Z. Wang, *Reconstruction Method for Gamma-Ray Coded-Aperture Imaging Based on Convolutional Neural Network*, Nuclear Instruments and Methods in Physics Research, Section A: Accelerators, Spectrometers, Detectors and Associated Equipment.

[13] J. J. Valiente-Dobón et al., *NEDA—NEutron Detector Array*, Nucl Instrum Methods Phys Res A **927**, 81 (2019).

[14] X. Fabian et al., *Artificial Neural Networks for Neutron/γ Discrimination in the Neutron Detectors of NEDA*, Nucl Instrum Methods Phys Res A **986**, 164750 (2021).

[15] T. Tambouratzis, D. Chernikova, and I. Pazsit, *A Comparison of Artificial Neural Network Performance: The Case of Neutron/Gamma Pulse Shape Discrimination*, in *2013 IEEE Symposium on Computational Intelligence for Security and Defense Applications (CISDA)* (2013), pp. 88–95.

[16] F. Belli, B. Esposito, D. Marocco, M. Riva, Y. Kaschuck, and G. Bonheure, *A Method for Digital Processing of Pile-up Events in Organic Scintillators*, Nucl Instrum Methods Phys Res A **595**, 512 (2008).

[17] M. Kafaee and S. Saramad, *Pile-up Correction by Genetic Algorithm and Artificial Neural Network*, Nucl Instrum Methods Phys Res A **607**, 652 (2009).

[18] C. Fu, A. di Fulvio, S. D. Clarke, D. Wentzloff, S. A. Pozzi, and H. S. Kim, *Artificial Neural Network Algorithms for Pulse Shape Discrimination and Recovery of Piled-up Pulses in Organic Scintillators*, Ann Nucl Energy **120**, 410 (2018).

[19] J. Han et al., *Pulse Characteristics of CLYC and Piled-up Neutron–Gamma Discrimination Using a Convolutional Neural Network*, Nucl Instrum Methods Phys Res A **1028**, (2022).

[20] J. M. Mueller, M. W. Ahmed, and H. R. Weller, *A Novel Method to Assay Special Nuclear Materials by Measuring Prompt Neutrons from Polarized Photofission*, Nucl Instrum Methods Phys Res A **754**, 57 (2014).

[21] J. M. Mueller, M. W. Ahmed, A. Kafkarkou, D. P. Kendellen, M. H. Sikora, M. C. Spraker, H. R. Weller, and W. R. Zimmerman, *Tests of a Novel Method to Assay SNM Using Polarized Photofission and Its Sensitivity in the Presence of Shielding*, Nucl Instrum Methods Phys Res A **776**, 107 (2015).

[22] K. W. Chin, H. Sagara, and C. Y. Han, *Application of Photofission Reaction to Identify High-Enriched Uranium by Bremsstrahlung Photons*, Ann Nucl Energy **158**, 108295 (2021).

[23] R. Kimura, H. Sagara, and S. Chiba, *Principle Validation of Nuclear Fuel Material Isotopic Composition Measurement Method Based on Photofission Reactions*, J Nucl Sci Technol **53**, 1978 (2016).

[24] S. Van Liew, W. Bertozzi, N. D'Olympia, W. A. Franklin, S. E. Korbly, R. J. Ledoux, and C. M. Wilson, *Identification and Imaging of Special Nuclear Materials and Contraband Using Active X-Ray Interrogation*, Phys Procedia **90**, 313 (2017).

[25] M. Delarue, E. Simon, B. Pérot, P. G. Allinei, N. Estre, D. Eck, E. Payan, I. Espagnon, and J. Collot, *New Measurements of Cumulative Photofission Yields of 239Pu, 235U and 238U with a 17.5 MeV*

Bremsstrahlung Photon Beam and Progress toward Actinide Differentiation, Nucl Instrum Methods Phys Res A **1040**, (2022).

[26] C. A. Meert, A. P. Panter, A. J. Jinia, A. T. MacDonald, S. D. Clarke, B. D. Pierson, and S. A. Pozzi, *High-Fidelity Photoneutron Detection via Neutron Activation Analysis*, Nucl Instrum Methods Phys Res A **1040**, (2022).

[27] R. Kimura, H. Sagara, and S. Chiba, *Precision Requirement of the Photofission Cross Section for the Nondestructive Assay*, EPJ Web Conf **146**, 4 (2017).

[28] D. B. Pelowitz, *MCNPX User'S Manual Version 2.6.0*, Los Alamos National Laboratory (2008).

[29] S. A. Pozzi, E. Padovani, and M. Marseguerra, *MCNP-PoliMi: A Monte-Carlo Code for Correlation Measurements*, Nucl Instrum Methods Phys Res A **513**, 550 (2003).

[30] S. A. Pozzi et al., *MCNPX-PoliMi for Nuclear Nonproliferation Applications*, Nucl Instrum Methods Phys Res A **694**, 119 (2012).

[31] A. J. Koning, D. Rochman, J. C. Sublet, N. Dzysiuk, M. Fleming, and S. van der Marck, *TENDL: Complete Nuclear Data Library for Innovative Nuclear Science and Technology*, Nuclear Data Sheets **155**, 1 (2019).

[32] T. Gozani, *Active Nondestructive Assay of Nuclear Materials*, U.S. Nuclear Regulatory Commission, Washington, D.C. **NUREG/CR-0602**, (1981).

[33] T. Gozani, *Threshold Photofission with Electron Accelerators - Why, How and Applications*, Atomkernenergie **19**, 63 (1972).

[34] N. V. , Kornilov, Verification of the 252Cf Standard in the Energy Range 2-20 MeV, 2015.

[35] M. Vretenar, *Linear Accelerators*, in *Proceedings of the CAS-CERN Accelerator School: Advanced Accelerator Physics* (CERN-European Organization for Nuclear Research, 2013), pp. 295–329.

[36] T. H. Shin, P. L. Feng, J. S. Carlson, S. D. Clarke, and S. A. Pozzi, *Measured Neutron Light-Output Response for Trans-Stilbene and Small-Molecule Organic Glass Scintillators*, Nucl Instrum Methods Phys Res A **939**, 36 (2019).

[37] G. F. Knoll, *Radiation Detection and Measurement*, Fourth (John Wiley & Sons, Inc., n.d.).

[38] J. B. Birks, *The Theory and Practice of Scintillation Counting* (Pergamon Press, 1964).

[39] ET Enterprises, *ET Enterprises 51 Mm (2") Photomultiplier 9214B Series Data Sheet*, https://et-enterprises.com/products/photomultipliers/product/p9214b-series.

[40] Inrad Optics, *Scintinel Stilbene Single Crystals*, https://inradoptics.com/pdfs/datasheets/InradOptics_Datasheet_Stilbene_Final.pdf.

[41] CAEN, *CAEN V1730/V1730S 16/8 Channel 14 Bit 500 MS/s Digitizer*, https://www.caen.it/products/v1730/.

[42] S. Walczak and N. Cerpa, *A Biological Basis of Artificial Neural Networks*, in *Encyclopedia of Physical Science and Technology*, 3rd Editio (Academic Press, 2001), pp. 631–645.

[43] L. P. Fávero, P. Belfiore, and R. de Freitas Souza, *Artificial Neural Networks*, in *Data Science, Analytics and Machine Learning with R* (Elsevier, 2023), pp. 441–467.

[44] A. Malekian and N. Chitsaz, *Concepts, Procedures, and Applications of Artificial Neural Network Models in Streamflow Forecasting*, in *Advances in Streamflow Forecasting* (Elsevier, 2021), pp. 115–147.

[45] T. Kohonen, Biological Cybernetics Analysis of a Simple Self-Organizing Process, 1982.

[46] R. Rojas, *Neural Networks: A Systematic Introduction* (Springer-Verlag Berlin Heidelberg New York, n.d.).

[47] J. K. Polack, M. Flaska, A. Enqvist, C. S. Sosa, C. C. Lawrence, and S. A. Pozzi, *An Algorithm for Charge-Integration, Pulse-Shape Discrimination and Estimation of Neutron/Photon Misclassification in Organic Scintillators*, Nucl Instrum Methods Phys Res A **795**, 253 (2015).

[48] A. J. Jinia, T. E. Maurer, C. A. Meert, M. Y. Hua, S. D. Clarke, H. S. Kim, D. D. Wentzloff, and S. A. Pozzi, *An Artificial Neural Network System for Photon-Based Active Interrogation Applications*, IEEE Access **9**, 119871 (2021).

[49] D. Wolpert, *Stacked Generalization (Stacking)*, Neural Networks **5**, 241 (1992).

[50] MathWorks Inc, MATLAB and Deep Learning Toolbox Release R2020a, n.d.

[51] M. F. Møller, *A Scaled Conjugate Gradient Algorithm for Fast Supervised Learning*, Neural Networks **6**, 525 (1993).

[52] R. D. Deslattes, E. G. Kessler, Jr., P. Indelicato, L. de Billy, E. Lindroth, and J. Anton, *X-Ray Transition Energies: New Approach to a Comprehensive Evaluation*, Rev Mod Phys **75**, 35 (2003).

[53] A. J. Jinia, T. E. Maurer, C. A. Meert, O. V. Pakari, S. D. Clarke, H.-S. Kim, D. D. Wentzloff, and S. A. Pozzi, *Prompt Photofission Neutron Detection in Depleted Uranium*, Accepted for Publication in Physical Review Applied (n.d.).

[54] S. A. Pozzi et al., *Validation of MCNPX-PoliMi Fission Models*, IEEE Nuclear Science Symposium Conference Record 997 (2012).

[55] S. D. Clarke, E. C. Miller, M. Flaska, S. A. Pozzi, R. B. Oberer, and L. G. Chiang, *Verification and Validation of the MCNPX-PoliMi Code for Simulations of Neutron Multiplicity Counting Systems*, Nucl Instrum Methods Phys Res A **700**, 135 (2013).

[56] M. Chadwick et al., *Handbook on Photonuclear Data for Applications: Cross-Sections and Spectra*, International Atomic Energy Agency, Austria **IAEA-TECDOC-1178**, (2000).

[57] N. H. Ba Sunbul, Validation of Ionizing Radiation Acoustic Imaging (IRAI) for 3D Dosimetry, Dissertation at the University of Michigan, 2022.

[58] E. C. Miller, S. D. Clarke, S. A. Pozzi, and E. Padovani, *MCNPX-PoliMi Post-Processing Algorithm for Detector Response Simulation*, Journal of Nuclear Materials Management **40**, 34 (2012).

[59] J. B. BIRKS, *Organic Crystal Scintillators*, The Theory and Practice of Scintillation Counting 235 (1964).

[60] E. Padovani, S. A. Pozzi, S. D. Clarke, and E. C. Miller, MCNPX-POLIMI USERS MANUAL, n.d.

[61] M. Frankl and R. Macián-Juan, *Photonuclear Benchmarks of C, Al, Cu, Ta, Pb, and U from the ENDF/B-VII Cross-Section Library ENDF7U Using MCNPX*, Nuclear Science and Engineering **183**, 135 (2016).

[62] W. C. Barber and W. D. George, *Neutron Yields from Targets Bombarded by Electrons*, Physical Review **116**, 1551 (1959).

[63] S. D. Clarke, S. A. Pozzi, S. J. Thompson, and A. W. Hunt, *Monte Carlo Assessment of Active Photon Interrogation Systems for Detection of Fissionable Material*, in *2008 Symposium on Radiation Measurements and Applications* (Berkely, California, U.S.A., 2008).

[64] *American National Standard Minimum Performance Criteria for Active Interrogation Systems Used for Homeland Security*, ANSI N42.41-2007 1 (2008).

[65] M. J. Berger, J. H. Hubbell, S. M. Seltzer, J. Chang, J. S. Coursey, R. Sukumar, D. S. Zucker, and Olsen K., *NIST Standard Reference Database 8 (XGAM)*, NIST, Physical Measurement Laboratory, Radiation Physics Division (2010).

[66] A. J. Jinia, T. E. Maurer, C. A. Meert, S. D. Clarke, H.-S. Kim, D. D. Wentzloff, and S. A. Pozzi, *Measurement of Photoneutrons from Depleted Uranium and Comparison Study Using MCNPX-PoliMi* , Under Review in Nuclear Science and Engineering (n.d.).